PERFORMANCE ANALYSIS OF ULTRAVIOLET COMMUNICATION IN THE PRESENCE OF TURBULENCE

Ph.D. Thesis

by

KAMAL KISHORE GARG

DEPARTMENT OF ELECTRICAL ENGINEERING
INDIAN INSTITUTE OF TECHNOLOGY INDORE

April, 2022

PERFORMANCE ANALYSIS OF ULTRAVIOLET COMMUNICATION IN THE PRESENCE OF TURBULENCE

A THESIS

Submitted in partial fulfillment of the

requirements for the award of the degree

of

DOCTOR OF PHILOSOPHY

by

KAMAL KISHORE GARG

DEPARTMENT OF ELECTRICAL ENGINEERING

INDIAN INSTITUTE OF TECHNOLOGY INDORE

April, 2022

INDIAN INSTITUTE OF TECHNOLOGY INDORE

CANDIDATE'S DECLARATION

I hereby certify that the work which is being presented in the thesis entitled "**PERFORMANCE ANALYSIS OF ULTRAVIOLET COMMUNICATION IN THE PRESENCE OF TURBULENCE**" in the partial fulfillment of the requirements for the award of the degree of DOCTOR OF PHILOSOPHY and submitted in the DEPARTMENT OF ELECTRICAL ENGINEERING, Indian Institute of Technology Indore, is an authentic record of my own work carried out during the time period from August 2017 to April 2022 under the supervision of Prof. Vimal Bhatia, Professor, Indian Institute of Technology Indore, India.

The matter presented in this thesis has not been submitted for the award of any other degree of this or any other institute.

26.04.2022

Signature of the student with date
(KAMAL KISHORE GARG)

This is to certify that the above statement made by the candidate is correct to the best of my knowledge.

26/04/22

Signature of Thesis Supervisor with date
(Prof. VIMAL BHATIA)

Kamal Kishore Garg has successfully given his Ph.D. Oral Examination held on **12/09/2022**.

12/09/22

Signature of Thesis Supervisor with date
(Prof. VIMAL BHATIA)

ACKNOWLEDGEMENTS

There is always a feeling of thankfulness that one conveys as an offer for the useful and necessary services that someone provides throughout one's life. First and foremost, I want to express my gratitude to the Almighty God for choosing this prestigious institute for me, without whose blessings I would not have been able to reach this milestone.

I would like to give special thanks and heartfelt gratitude to my Ph.D. supervisor, Prof. Vimal Bhatia, for giving me the opportunity to join the Signal and Software Group (SaSg) and for his endless help and continuous support in achieving one of the major milestones in my life. It is an honour and a joy for me to work under the direction of such a kind and dedicated supervisor like Prof. Vimal Bhatia. I'd also like to express my gratitude to Prof. Mukesh Kumar and Dr. Neminath Hubballi, members of my PSPC committee, who continuously evaluated my research progress and provided insightful and valuable suggestions on improving the quality of my research work.

I am really grateful to all of the academic members and staff members of the Indian Institute of Technology Indore for their essential assistance throughout my thesis study. I'd also like to express my gratitude to all of the members of the Signal and Software Group (SaSg) for their encouragement and support, which helped me get through a difficult period in my life while never making me feel alone on this arduous trip. I would like to express my gratitude to my seniors, Dr. Abhijeet Bishnu and Dr. Sanjeev Sharma. In particular, I'd also like to thank Dr. Parvez Shaik, Dr. Praveen Kumar Singya, Dr. Sandesh Jain, and all my colleagues for assisting me with my thesis work in various ways.

I would like to thank my boss, Mr. John Bourke, my colleague, Mr. Purandhar Krishnamurthy, and all the staff members of Mobile Internet India Pvt. Ltd., who provided me with the flexibility and all the possible support I needed from time to time during my Ph.D. tenure.

Finally, and most importantly, none of this would have happened without the love of my family. I would like to express my gratitude to my brother, Neeraj Aggarwal, and my parents. Their support, constant encouragement, and love always helped me through every phase of my life. I'd want to express my gratitude to my wife, Rachna Sharma, and my amazing children, Aashi and Vihaan, for their unwavering support and care. Without their consistent encouragement and motivation during difficult times, I would never have accomplished this. My dissertation is dedicated to them.

KAMAL KISHORE GARG

Dedicated
to
Parents, Family & Teachers

If I have seen further than others, it is by standing upon the shoulders of giants

— Issac Newton

ABSTRACT

Optical wireless communication (OWC) is gaining considerable research attention due to the scarcity of RF spectrum, and increasing demand for multi-rate multimedia services. The conventional OWC systems, including free-space optics (FSO) and visible light communication (VLC), requires line-of-sight (LOS) along with strict pointing, acquisition, and tracking (PAT) requirements. These constraints limit FSO and VLC system's applicability in scenarios where it is not feasible to obtain LOS. Ultraviolet communication (UVC), on the other hand, overcomes such limitations and finds a prominent role in establishing the reliable communication link. UVC has the unique ability to operate in non-LOS (NLOS) mode. This ability is due to the extremely small operating wavelength of ultraviolet (UV) waves ranging from 200 nm to 280 nm (commonly referred to as UV-C band), which results in the strong interaction of UV waves with atmospheric particles, thereby giving rise to scattering phenomenon. Additionally, the deep UV band is solar blind due to the absorption of UV-C waves by the ozone layer, which results in almost negligible background noise near to the earth surface. Due to the exceptionally low background noise, a wide field of view (FOV) can be used at the receivers, enhancing the communication system's performance.

NLOS UVC suffers from high path-loss due to atmospheric absorption and turbulence-induced fading caused by inhomogeneous atmospheric conditions. These impairments severely degrade NLOS UVC system's performance and limit its communication range to a short distance. Further, in-spite of the availability of huge license free band, the data rate of NLOS UVC is rather limited due to low modulation speed of UV LEDs. The goal of this thesis is to address these challenges of NLOS UVC through the use of spatial diversity, cooperative relaying, and higher-order modulation schemes, and making it suitable for data-intensive applications, and long distance outdoor communication.

In this thesis, initially the problem of turbulence induced fading is addressed through the use of a single-input-multiple-output (SIMO) NLOS UVC system employing selection combining (SC) at the receiver. The multiple receiver branches are assumed to be correlated, and the system's performance is analyzed in terms of outage probability, ergodic capacity, and average symbol error rate (ASER) for higher order modulation formats including square quadrature amplitude modulation (SQAM), rectangular QAM (RQAM), cross QAM (XQAM), and hexagonal QAM (HQAM). Numerical study is conducted and it is demonstrated that the proposed system model effectively mitigates the effect of fading, and use of higher order modulation schemes significantly improves the data rate.

Further, a parallel multi-relay cooperative NLOS UVC system is presented to address the problems of both the high path-loss and fading. Amplify-and-forward (AF) based relays are employed and SC is used at the receiver. Comparative performance of the considered system is studied for fixed-gain and variable-gain AF relaying. Higher order modulation schemes are used with the objective of improving the data rate of the system. Detailed performance study is performed in terms of outage probability, diversity analysis, and ASER for different system configurations, and useful insights are drawn.

Furthermore, a decode-and-forward (DF) based multi-relay NLOS UVC system employing best-relay selection is studied. The performance of the considered system is assessed in terms of outage probability, diversity order, ASER for RQAM,

SQAM, XQAM, and HQAM schemes. In practical systems, it is not possible to have complete CSI knowledge at all communication nodes thereby resulting in channel estimation errors (CEEs). The negative impact of CEE on system performance can not be ignored in realistic system designs. A detailed comparative study showing the impact of CEE on the system performance for different number of relays is evaluated and useful inferences are drawn.

Additionally, a hybrid RF/NLOS UVC system is proposed to extend the communication range of an RF system to RF prohibited areas with no LOS connectivity. Hybrid of RF and OWC technologies such as VLC and FSO have been extensively studied in the literature. However, the need of LOS by FSO and VLC hinders their applicability to scenarios where LOS in the optical link is not available. UVC is an attractive choice in such situations due to its ability to operate in NLOS mode. A detailed performance study of the proposed hybrid RF/NLOS UVC system is conducted considering the practical case of imperfect CSI at the receiver. Impact of CEE on the RF and UVC link is studied and it is demonstrated that the RF link is more vulnerable to CEE as compared to UVC link. The ASER analysis is performed and comparative performance of RQAM, XQAM, and HQAM schemes is presented.

Lastly, numerical results are compared with Monte-Carlo simulations to verify the correctness of derived expressions.

Contents

List of Figures

List of Tables

List of Abbreviations/Acronyms

2D two-dimentional

3G/4G/5G/6G 3rd/4th/5th/6th generation

AF amplify-and-forward

AM amplitude modulation

ARDO asymptotic relative diversity order

ASER average symbol error rate

ASK amplitude shift keying

AWGN additive white Gaussian noise

BER bit error rate

BPSK binary phase-shift keying

CDF cumulative distribution function

CEE channel estimation error

CSI channel state information

CV common volume

DC direct current

DCO-OFDM DC-biased optical OFDM

DF decode-and-forward

e2e end-to-end

EGC equal-gain combining

EUV extreme UV

FOV field-of-view

FSO free space optics

HDTV high-definition television

HQAM hexagonal QAM

IP Internet protocol

IR infrared

ISI intersymbol interference

LB lower-bound

LED light emitting diode

LMMSE linear minimum mean square error

LN lognormal

LOS line-of-sight

MIMO multiple-input multiple-output

MISO multiple-input and single-output

MMSE minimum mean square error

MRC maximal ratio combining

NLOS non-line-of-sight

OFDM orthogonal frequency division multiplexing

OOK on-off keying

OWC optical wireless communication

PAM pulse amplitude modulation

PAPR peak-to-average-power ratio

PD photodetector

PDF probability density function

PPM pulse position modulation

PSK phase shift keying

QAM quadrature amplitude modulation

QPSK quadrature phase-shift keying

RDO relative diversity order

RF radio frequency

RQAM rectangular QAM

RV random variable

Rx receiver

SC selection combining

SER symbol error rate

SIM subcarrier intensity modulation

SIMO single-input and multiple-output

SISO single-input and single-output

SNR signal-to-noise ratio

SQAM square QAM

SR selection-relaying

SSC switched-and-stay combining

TAS transmit antenna selection

TLV threshold limit value

Tx transmitter

UB upper-bound

UV ultraviolet

UVC ultraviolet communication

VL visible light

VLC visible light communication

XQAM cross QAM

List of Symbols

- Basic arithmetic and calculus notations with their definitions.

Elementary & Special Functions

Notation	Definition
$Q(x)$	$= \frac{1}{\sqrt{2\pi}} \int_x^{\infty} e^{-\frac{t^2}{2}} dt$ is the Gaussian Q-function.

Probability & Statistics

Let X be a random variable (RV).

Notation	**Definition**
$\mathbb{E}[\cdot]$	statistical expectation operator
$\Pr[\cdot]$	statistical probability operator
$f_X(\cdot)$	probability density function (PDF) of a RV X
$F_X(\cdot)$	cumulative distribution function (CDF) of a RV X
$\mathcal{N}(\mu, \sigma^2)$	normal distribution with mean μ and variance σ^2
$\mathcal{CN}(\mu, \sigma^2)$	complex normal distribution with mean μ and variance σ^2

Vectors & Matrices

Notation	**Definition/interpretation**
$\mathbf{a}_i$	i^{th} element of a $1 \times n$ vector $\mathbf{a}$
$\mathbf{A}_{i,j}$	i^{th} element of j^{th} column of an $m \times n$ matrix $\mathbf{A}$

Chapter 1

Introduction

1.1 Overview

Wireless communication system designers have been confronted with an ever-increasing need for high-capacity and high-data-rate wireless applications such as gaming, streamed multimedia, high-definition television (HDTV), as well as Internet protocol (IP) telephony. The current system is experiencing severe congestion of the radio-frequency (RF) spectrum and wireless traffic bottleneck in order to cater an exponentially increasing amount of data to end users within an acceptable delay. The scarcity of RF spectrum and the need for an affordable and attractive high-data rate technology which can complement the existing RF systems has encouraged researchers to shift their focus to the optical band of the electromagnetic spectrum with wavelength range $350 - 1550$ nm. This led to the ascend of optical wireless communication (OWC) systems [1].

Over the last few decades, OWC has received growing attention and effort. In comparison to a RF system, it exhibits various potential advantages, including a huge unlicensed bandwidth, low-power and compact transceiver, high resilience to jamming, and the possibility for data rate enhancement. Due to these advantages, OWC is an realistic and intriguing addition to next-generation wireless connectivity (5G and beyond). An OWC system transmits data using an optical wave with a wavelength ranging from infrared (IR), visible-light (VL) to ultraviolet (UV) [2].

The IR optical band has three regions (a) IR-A ($780-1400$ nm), (b) IR-B ($1400-3000$ nm), and (c) IR-C ($3000-10^6$ nm). Outdoor and indoor communications have benefited from infrared technology by utilizing lasers or light-emitting diodes (LEDs) in line-of-sight (LOS) conditions. IR-A is intended for wireless communications over short distances. IR-B is mostly utilized for long-distance communications, whether guided (through optical fibre) or free space optical (FSO). IR-C, on the other hand, has been extensively used in military applications.

Visible light communication (VLC) refers to OWC systems that operate in the visible band ($380-780$ nm) [2]. LEDs are used in VLC systems because they may be pulsed at very high speeds without affecting the lighting output or the human eye. The use of LEDs for both illumination and communication is a sustainable and energy-efficient strategy that has the potential to transform how we utilize light. VLC can be employed in a variety of applications, including wireless local area networks, wireless personal area networks, and vehicle networks.

UV spectrum comprises of wavelength range $10-380$ nm which is subdivided into 4 bands (a) UV-A ($315-380$ nm) (b) UV-B ($280-315$ nm) (c) UV-C ($200-280$ nm) (d) extreme UV (EUV) ($10-200$ nm). UV-A and UV-B bands are effective in a wide variety of applications, including commercial, military, medical, and dental. UV-C band, also known as deep UV band, is employed in wireless ultraviolet communications (UVCs). EUV comprises of extremely small wavelength and requires high vacuum for transmission.

1.2 Ultraviolet Communication

UVC, although still in its infancy stage, is attracting considerable research interest in academia and business as a result of recent breakthroughs in UV sources and detectors [3]. Deep UV band has been widely adopted for UVC due to its unique atmospheric propagation characteristics. The conventional IR and VL based OWC systems, including FSO and VLC, requires LOS along with strict pointing, acquisition, and tracking (PAT) requirements. These constraints limit FSO and VLC system's applicability in scenarios where it is not feasible to obtain LOS. UVC, on the other hand, overcomes these constraints and plays a critical role in establishing a reliable communication link [4]. First and foremost, UVC has the unique ability to operate in non-line-of-sight (NLOS) mode due to the strong interaction of UV waves with molecules and aerosols present in the atmosphere [5, 6]. There is a lot of UV in this band that is scattered by the atmosphere. This allows the radiation to be directed toward a receiver even when there is no direct LOS between the sender and receiver. Additionally, the deep UV band is solar blind at ground level due to ozone absorption in the upper atmospheric layers. Thus, background noise has a negligible effect, permitting the use of wide field-of-view receivers (FOV) [3]. From a safety perspective, the harmful effect of UV-C radiation on humans can be avoided by conforming to the threshold limit value (TLV) of exposure established by the International Commission on Non-Ionizing Radiation Protection (ICNIRP) and the American Conference of Governmental Industrial Hygienists (ACGIH) [7, 8].

When UV light travels through an atmospheric channel, it encounters a variety of negative factors as a result of the UV wave's interaction with atmospheric constituents. Path loss and atmospheric turbulence are two of the most critical factors that affect the quality of communication. Path loss quantifies the amount of power a signal loses as it travels through a communication channel. Atmospheric turbulence occurs as a result of change in the refractive index of the atmosphere thereby causing random fluctuations in the received signal strength. This phenomenon is referred to as turbulence-induced fading.

Fig. 1.1 shows a typical single-input-single-output (SISO) NLOS UVC channel between transmitter (Tx) and receiver (Rx) which are d distance apart. ϕ^{Tx} and θ^{Tx} are the beam divergence and elevation angle of the Tx, respectively; and, ϕ^{Rx} and θ^{Rx} are the FOV and elevation angle of the Rx, respectively. An NLOS UVC experiences path loss due to both scattering [6] and turbulence [9]. Closed-form expression for

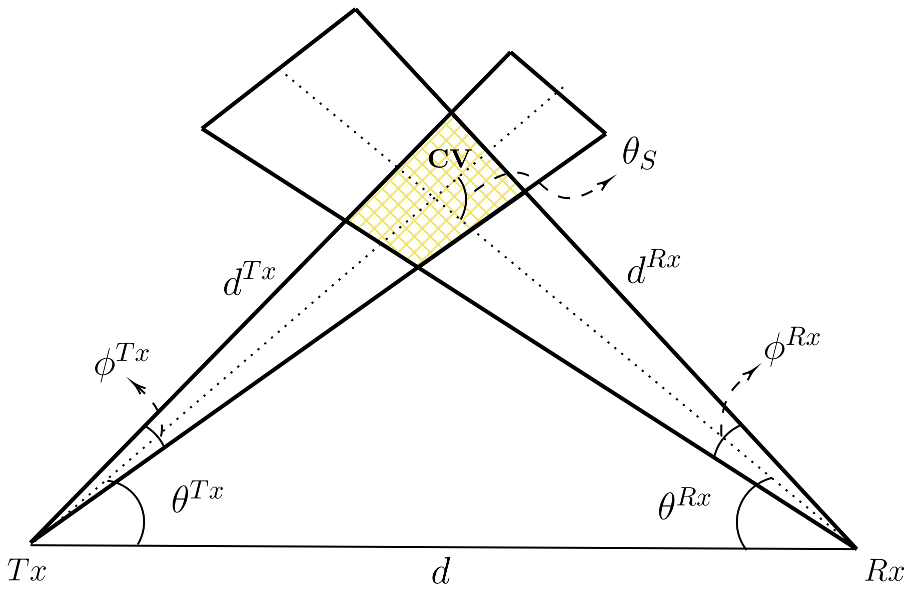

Figure 1.1: NLOS UVC channel.

the scattering path loss under single scattering assumption is presented in [10]. This scattering path loss model is shown to have close resemblance with the experimental data for smaller values of ϕ^{Tx}. We have adopted this scattering path loss model in this work. The path loss due to turbulence in NLOS UVC system was introduced in [9], and is shown to have significant impact on the system performance. We have considered turbulence path loss in our analysis and the same is incorporated in (1.5).

The closed-form expression for the path loss due to scattering is given as [10]

$$\ell^S = \frac{k_s A_r {\phi^{Tx}}^2 \phi^{Rx} P(\theta_S)\sin(\theta_S)\big[12\sin^2(\theta^{Rx}) + {\phi^{Rx}}^2\sin^2(\theta^{Tx})\big]}{96d\sin(\theta^{Tx})\sin^2(\theta^{Rx})(1-\cos(\phi^{Tx}/2))\exp\big(k_e d\big[\sin(\theta^{Tx})+\sin(\theta^{Rx})\big]/\sin(\theta_S)\big)}, \tag{1.1}$$

where A_r is the effective area of Rx, and $\theta_S = \theta^{Tx} + \theta^{Rx}$. k_e is the extinction coefficient given as $k_e = k_s + k_a$, with k_a as the absorption coefficient and k_s is the scattering coefficient. $P(\psi)$ is the single scattering phase function given by

$$P(\psi) = \frac{k_s^{\mathrm{Ray}}}{k_s}P^{\mathrm{Ray}}(\psi) + \frac{k_s^{\mathrm{Mie}}}{k_s}P^{\mathrm{Mie}}(\psi). \tag{1.2}$$

The scattering coefficient is computed as $k_s = k_s^{\mathrm{Ray}} + k_s^{\mathrm{Mie}}$, where k_s^{Ray} and k_s^{Mie} are the Rayleigh and Mie scattering coefficients, respectively. $P^{\mathrm{Ray}}(\psi)$ and $P^{\mathrm{Mie}}(\psi)$ are the Rayleigh and Mie scattering phase functions, respectively, and are defined as [10]

$$P^{\text{Ray}}(\psi) = \frac{3[1+3\gamma+(1-\gamma)\psi^2]}{16\pi(1+2\gamma)} \tag{1.3}$$

and,

$$P^{\text{Mie}}(\psi) = \Big(\frac{1-g^2}{4\pi}\Big)\Bigg[\frac{1}{(1+g^2-2g\psi)^{3/2}} + f\frac{0.5(3\psi^2-1)}{(1+g^2)^{3/2}}\Bigg], \tag{1.4}$$

where γ, f and g are the model parameters.

The NLOS UVC channel is modeled as a combination of two individual LOS communication links, one from Tx to common volume (CV) and another from CV to Rx [11]. The distance between Tx and Rx is considered to be of few hundred meters such that the irradiance variance of the received signal is less than 1.2 [12]. In such case, the UV signal experiences weak turbulence and the channel coefficient is modeled using lognormal (LN) distribution [9, 11, 12]. The closed-form expression for the probability density function (PDF) of NLOS UV channel coefficient (h) under weak turbulence condition is derived in [12] and is given as

$$f_h(h) = \frac{1}{\sigma_h h\sqrt{2\pi}} \exp\Bigg[-\frac{(\ln h - \mu_h)^2}{2\sigma_h^2}\Bigg], \tag{1.5}$$

where μ_h and σ_h^2 are the mean and variance, respectively, of the associated Gaussian random variable (RV) $\ln(h) \sim \mathcal{N}(\mu_h, \sigma_h^2)$, and are computed as [12]

$$\mu_h = \mu_{\text{Tx-CV}} + \mu_{\text{CV-Rx}}, \tag{1.6}$$

$$\sigma_h^2 = \sigma_{\text{Tx-CV}}^2 + \sigma_{\text{CV-Rx}}^2. \tag{1.7}$$

$\sigma_{\text{Tx-CV}}^2$ and $\sigma_{\text{CV-Rx}}^2$ are the log-irradiance variance of the LOS links from Tx to CV and from CV to Rx, respectively. Assuming the plane wave propagation and horizontal link between Tx and Rx, these parameters are given by [9, 12]

$$\sigma_{\text{Tx-CV}}^2 = \frac{1.23C_n^2(2\pi/\lambda)^{7/6}d^{11/6}\sin\big(\theta^{Rx}\big)^{11/6}}{\sin(\theta_S)^{11/6}}, \tag{1.8}$$

and,

$$\sigma^2_{\text{CV-Rx}} = \frac{1.23 C_n^2 (2\pi/\lambda)^{7/6} d^{11/6} \sin\left(\theta^{Tx}\right)^{11/6}}{\sin(\theta_S)^{11/6}}, \tag{1.9}$$

where C_n^2 is the refractive index structure parameter, and λ is the wavelength. $\mu_{\text{Tx-CV}} = -0.5\sigma^2_{\text{Tx-CV}} - \ell^T_{\text{Tx-CV}}$ and $\mu_{\text{CV-Rx}} = -0.5\sigma^2_{\text{CV-Rx}} - \ell^T_{\text{CV-Rx}}$ are the log-irradiance mean for the LOS links from Tx-CV and CV-Rx, respectively [12]. Terms $\ell^T_{\text{Tx-CV}}$ and $\ell^T_{\text{CV-Rx}}$ are attributed to the turbulence path loss of Tx-CV and CV-Rx links, respectively, and can be computed as [9]

$$\ell^t_{\text{Tx-CV}} = a_0 \sqrt{\frac{\sin(\theta^{Rx})^{11/6}}{\sin(\theta_S)^{11/6}}},\ \ell^t_{\text{CV-Rx}} = a_0 \sqrt{\frac{\sin(\theta^{Tx})^{11/6}}{\sin(\theta_S)^{11/6}}}, \tag{1.10}$$

where $a_0 = \frac{\ln(10)}{5}\sqrt{\frac{23.17 C_n^2 (2\pi)^{7/6} d^{11/6}}{\lambda^{7/6}}}$.

1.3 Cooperative Communication

Turbulence induced fading is a significant issue in OWC [13]. Spatial diversity has proven to be an effective and widely used technique to alleviate the effects of fading and to improve the performance of communication systems [14]. In spatial diversity, several parallel communication links are formed between Tx and Rx by employing multiple transmit and/or receive branches. Such systems are usually termed as multiple-input multiple-output (MIMO). Use of MIMO system results in reception of the multiple copies of the transmitted data stream at the receiver. A combining technique is used at the receiver to properly combine the received copies of the signal with an objective to improve end-to-end (e2e) signal-to-ratio (SNR) of the communication link, and thereby improving the communication quality. Some of the popularly used diversity combining schemes are maximal ratio combining (MRC), selection combining (SC), and equal-gain combining (EGC) [14].

In this work, the selection combining scheme is used at the Rx primarily based on two considerations: (1) lower receiver complexity, and (2) analytical tractability. The MRC and EGC combining techniques necessitate a new receiver chain for each diversity branch, which increases the total complexity of the receiver. In contrast, only one of the diversity branches processes the received signal during selection combining. In particular, the typical SC combiner selects the branch with the highest SNR. In addition, the coherent sum of the separate branch signals is not necessary because the output of the SC combiner is identical to the signal on only one of the branches. Consequently, the SC scheme is compatible with both differentially coherent and noncoherent modulation schemes, as it does not require knowledge of the signal phases on each branch, as would be required to execute MRC or EGC in a coherent system. In addition, the EGC and MRC schemes compute the weighted sum of the signal received over multiple branches, which involves calculating the distribution of the received signal at the combiner's output. To analyse such UVC systems, the distribution of the sum of lognormal random variables must be determined, which remains an open problem. Although there are several curve fitting approximations available in the literature for determining the distribution of the sum of lognormal random variables, these techniques can result in large approximation errors [15–19]. This is another reason to choose SC over EGC and MRC.

It is not always feasible to employ multiple transmit/receive branches at each node owing to device size and hardware constraints (for example, in mobile handsets and sensor networks). Cooperative communication is a viable choice in such situations [20]. The fundamental concept of cooperative communication is to process data between source and destination via an alternate indirect multipath with the help of intermediary relay nodes (each equipped with a single transmit/receive branch), thereby producing a virtual MIMO system. Cooperative communications is used in a variety of standards, including IEEE 802.16j, IEEE 802.22, and 3GPP-LTE-Advanced (LTE-A), and plays an important role in 5G and beyond standards [21].

Fig. 1.2 depicts a dual-hop one-way cooperative communication system consisting of a source (S), relay (R), and destination (D) nodes. In this system, one complete communication takes place in two phases. In the first phase (Phase 1),

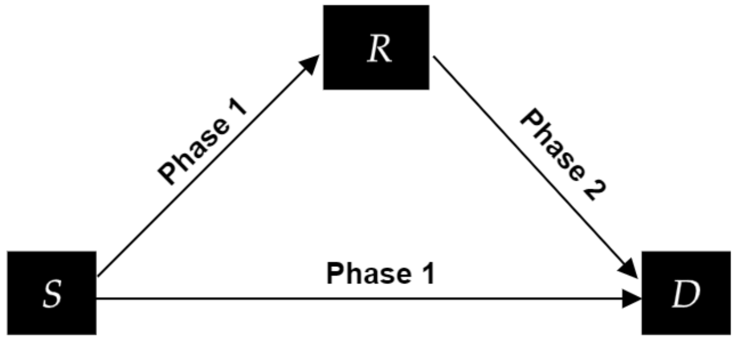

Figure 1.2: Dual-hop one-way cooperative communication system.

node S transmits signal which is received by both R and D nodes. In the second phase (Phase 2), S node remains silent, and R node forwards the received signal based on a relaying protocol to the D node. At the end of second phase, node D has two copies of the received signal from S and R. Finally, D combines the received signal copies using a combining scheme (such as SC, EGC or MRC) to improve the overall SNR of the system. There exists different types of relaying techniques which can be employed to realize such cooperative communication system. Selection of the appropriate relaying technique depends on various factors such as transceiver complexity, nodes location, and channel conditions.

Decode-and-forward (DF), amplify-and-forward (AF) and selection-relaying (SR) are widely used cooperative relaying techniques in the literature [20, 22]. In DF relaying, R explicitly decodes the message received from S and passes the newly generated signal to D. DF relaying scheme is alternatively referred to as regenerative relaying. In AF relaying technique, R does not decodes the received signal, instead it simply amplifies and forwards the received signal to the D node. AF relaying is also known as non-regenerative relaying schemes. SR, on the other hand, is a dynamic relaying scheme in which relays are chosen to retransmit the source message only when the relayed link is sufficiently reliable. This scheme can be used in conjunction with both the DF and AF schemes to increase the efficiency of cooperation.

1.4 Modulation Schemes

In spite of huge bandwidth availability in UV band, the data transmission rate of NLOS UVC is still limited. This is mainly due to the low modulation speed of the LEDs operating in the deep UV band [23]. In such case, high data rate can be achieved by using spectrally efficient higher order modulation schemes [24]. In the existing literature, the performance analysis for UVC is generally limited to on-off-keying (OOK) modulation scheme, due to its simplicity [25–30]. Minimizing average transmit power for a given bit error rate (BER) or symbol error rate (SER) can enable future wireless communication systems to communicate at high data rates while using less power. However, higher data rates for a given bandwidth typically require a higher transmit power to achieve the same performance. The use of spectrally efficient higher-order modulation schemes such as quadrature amplitude modulation (QAM) and its variants is an effective way to achieve both high data rates and optimal power utilisation. In this section, we provide a brief introduction to various QAM based versatile and bandwidth-efficient futuristic modulation schemes including rectangular QAM (RQAM), cross QAM (XQAM), and hexagonal QAM (HQAM).

1.4.1 Rectangular QAM (RQAM)

RQAM is a bandwidth efficient modulation scheme which has got wide acceptance due to its generic nature [31–34]. RQAM includes multilevel amplitude-shift-keying (ASK), OOK, quadrature phase shift keying (QPSK), square QAM (SQAM), orthogonal binary frequency-shift-keying (OBFSK) as its special cases [33]. RQAM constellation is obtained by arranging the constellation points in a rectangular shape. The obtained rectangular constellation can be parallel to in-phase axis or quadrature-phase axis with same average energy. The 32-points RQAM constellations are shown in Fig. 1.3.

The conditional expression for the SER of $M_I \times M_Q$ RQAM over additive white

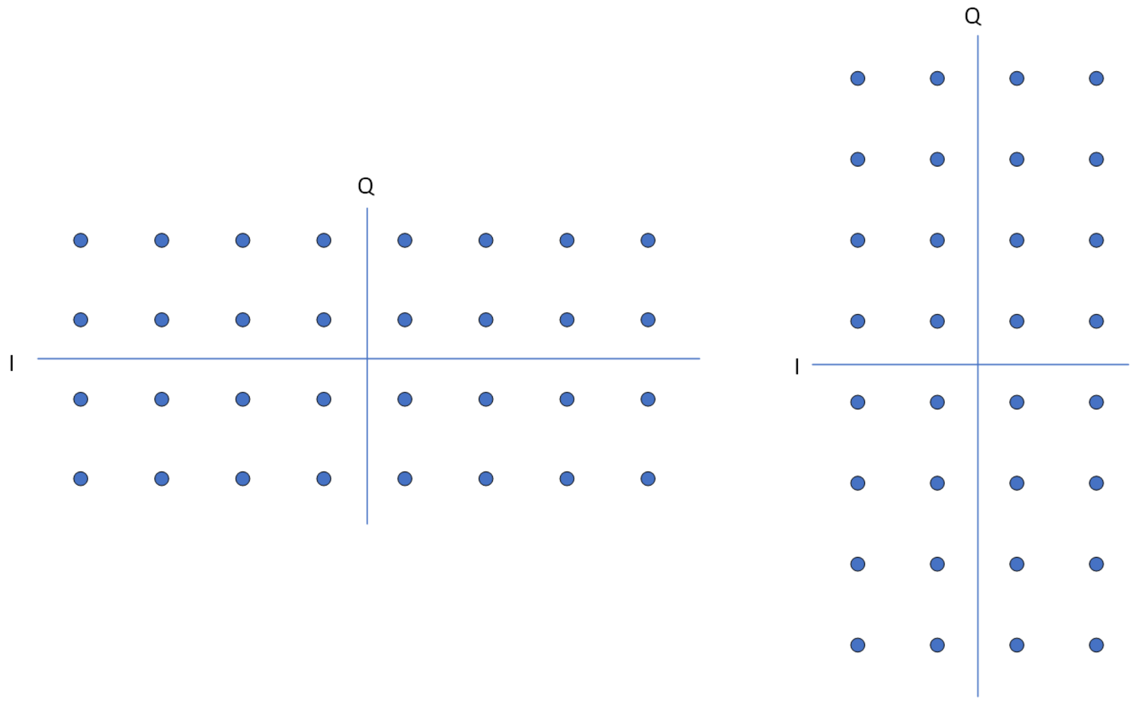

Figure 1.3: 32-points RQAM constellations.

Gaussian (AWGN) channel is given as [32]

$$P_s^{\mathrm{RQAM}}(e|\chi) = 2p_0Q(a_0\sqrt{\chi}) + 2q_0Q(b_0\sqrt{\chi}) - 4p_0q_0Q(a_0\sqrt{\chi})Q(b_0\sqrt{\chi}), \tag{1.11}$$

where $a_0 = \sqrt{6/((M_I^2-1)(M_Q^2-1)\beta_0^2)}, b_0 = \beta_0 a_0$, $p_0 = 1 - 1/M_I$, $q_0 = 1 - 1/M_Q$, and $\beta_0 = d_Q/d_I$, in which d_Q and d_I denote quadrature and in-phase decision distances, respectively. The expression for M-ary SQAM scheme can directly be obtained from (4.19) by substituting $M = \sqrt{M_I} = \sqrt{M_Q}$ [35].

1.4.2 Cross QAM (XQAM)

RQAM is a suitable modulation scheme for transmission when the number of bits per symbol is even. However, RQAM is not a power efficient modulation scheme for the transmissions involving odd number of bits per symbol. In such cases, XQAM offers higher power spectral efficiency, with a minimum SNR gain of around 1 dB, as compared to RQAM [33]. A 32-points XQAM constellation is shown in Fig. 1.4.

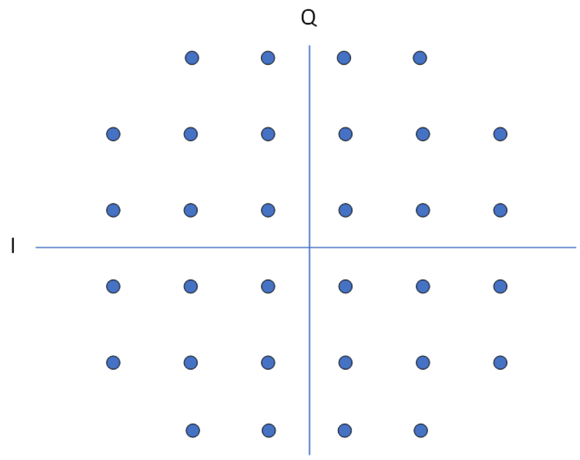

Figure 1.4: 32-points XQAM constellation.

The conditional expression for XQAM-32 is given in [36] as

$$P_s^{\text{XQAM-32}}(e|\chi) = \frac{1}{8}\Big[26Q(\sqrt{2A\chi}) + Q(2\sqrt{A\chi}) - 23Q^2(\sqrt{2A\chi})\Big], \tag{1.12}$$

where $A = \frac{48}{31M-32}$ with M representing the constellation size which is 32 for XQAM-32 scheme.

1.4.3 Hexagonal QAM (HQAM)

HQAM is a futuristic two-dimensional (2D) constellation scheme which is based on hexagonal lattice [37]. HQAM has optimum Euclidean distance between constellation points due to its densest 2D packing, which enables improved power efficiency with low peak-to-average-power ratio (PAPR). As a result, HQAM offers considerable SNR gain over RQAM and XQAM schemes for higher constellation sizes. Fig.1.5 shows the HQAM constellations for different constellation sizes.

The conditional expression for the SER of HQAM over AWGN channel is given as [34]

$$P_s^{\text{HQAM}}(e|\chi) = DQ(\sqrt{q_1\chi}) + \frac{2}{3}D_C Q^2(\sqrt{2q_1\chi/3}\,) - 2D_C Q(\sqrt{q_1\chi})Q(\sqrt{q_1\chi/3}\,), \tag{1.13}$$

where q_1, D and D_C are the constants which has different values for different HQAM

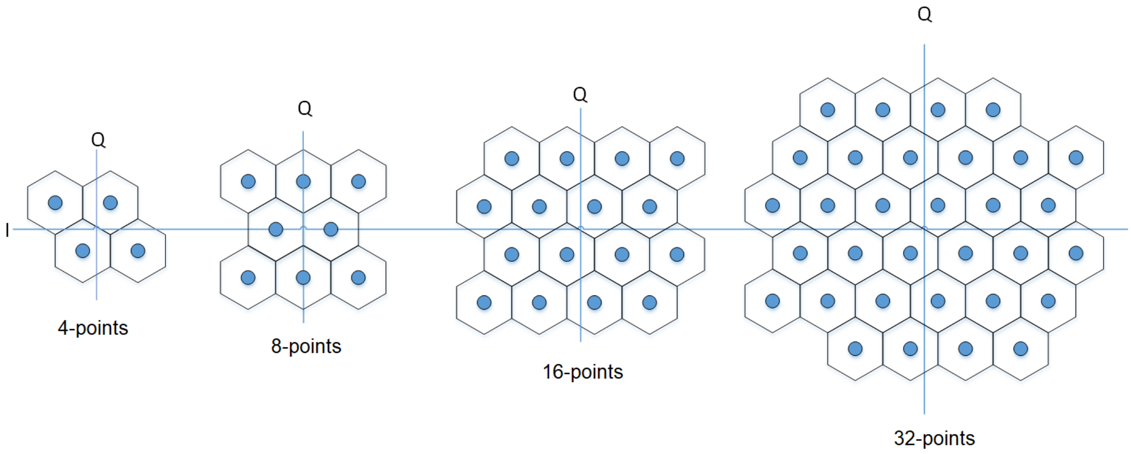

Figure 1.5: HQAM constellations.

constellation sizes. For M-ary HQAM constellation

$$q_1 = \frac{N_0}{E_s}\left(\frac{\Delta_1}{2\sigma}\right)^2, \; D = \frac{1}{M}\sum_{k=0}^{M-1} D(k), \; D_C = \frac{1}{M}\sum_{k=0}^{M-1} D_C(k), \tag{1.14}$$

where Δ_1 is the half of the minimum distance between constellation points, σ is the standard deviation of the AWGN. $D(k)$ is the number of nearest neighborhoods (NNs) of the constellation point k, and $D_C(k)$ represents the number of couples of adjacent NNs of point k [37]. The values of these parameters for various constellation sizes considered in this study are given in Table 1.1.

Table 1.1: Parameter values for HQAM

Constellation Size	q_1	D	D_C
$M = 4$	1	5/2	3/2
$M = 8$	32/69	7/2	21/8
$M = 16$	8/35	33/8	27/8
$M = 32$	512/4503	75/16	33/8
$M = 64$	8/141	163/32	75/16

1.5 Subcarrier Intensity Modulation (SIM)

Subcarrier intensity modulation (SIM) with direct detection for OWC is an attractive alternative to conventional modulation/detection schemes such as OOK and pulse position modulation (PPM) based intensity modulations [38]. Recently, SIM has gained wide adoption in OWC systems due to its several unique benefits including support for higher-order-modulation schemes, low-complexity implementation, and improved error performance [39]. In this work, SIM based techniques are adopted for the NLOS UVC system to overcome the rotational ambiguity associated with the complex modulation schemes for optical channel [39–42]. In SIM technique, the information symbols are pre-modulated using the RF subcarrier(s). A direct current (DC) bias is added to the pre-modulated RF signal to ensure that the signal amplitude is greater than a pre-defined positive threshold. The DC-biased RF signal is then used to modulate the intensity of a UV laser diode/LED.

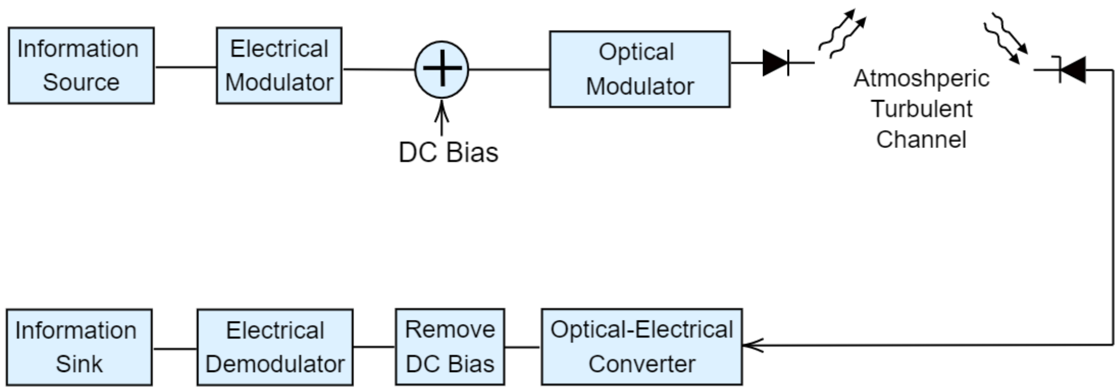

Figure 1.6: Block diagram of SIM.

The generic block diagram of SIM based optical system is shown in Fig. 1.6. It consists of an information source/sink, electrical modulator/demodulator, optical modulator, and photo detector. The information bit stream, obtained from the information source block, is first modulated on a RF subcarrier using a conventional electric modulator block. Both the phase and/or amplitude modulators are used as the electrical modulator block. The pre-modulated RF subcarrier is then used to drive the intensity of an optical source. Usually for the outdoor OWC system, semiconductor laser diode or LED is used as an optical source. Since the input of the semiconductor laser diode/LED must be non-negative, the pre-modulated RF subcarrier is added with a DC bias before driving the laser diode. The output of the laser diode is finally transmitted to the atmosphere. At the receiver, a photodetector is used to convert the received optical signal into an electrical signal. After removing the DC bias from the electrical signal (through a bandpass filter), the electrical signal is passed to the electrical demodulator and detector. Finally, the output of electrical demodulator/detector is collected at the information sink. For an intensity modulation system the received optical power is given as [38]

$$y(t) = P_r(t)x(t) + \nu(t), \tag{1.15}$$

where $P_r(t)$ is the received optical power, $x(t)$ is the scintillation characterized by the stationary probability process, and $\nu(t)$ is the AWGN. As an example, for subcarrier phase shift keying (PSK) modulation the received optical power is given as

$$P_r(t) = x(t)\frac{P_{max}}{2}(1 + m\ \cos(2\pi f_c t + \Phi_j)) + \nu(t), \tag{1.16}$$

where f_c is frequency of RF subcarrier, $\Phi_j = \frac{2(j-1)\pi}{M}$, $j = 1, 2, ...M$, and $M = 2^k$, so that the demodulator has zero threshold and this zero threshold is independent of irradiance fluctuation caused by atmospheric turbulence [43]. Further, P_{max} is the received peak power, and m is the modulation index. Due to the slow scintillation changes, the DC term $x(t)\frac{P_{max}}{2}$ can be eliminated. The electrical current signal $i(t)$ at the output of the photodiode can be expressed as

$$i(t) = x(t)\frac{P_{max}(eDG)}{2}m\ \cos(2\pi f_c t + \Phi_j) + \nu(t), \tag{1.17}$$

where (eDG) is the constant of photoelectric transfer [38]. Finally, $i(t)$ is demodulated using the reference electrical carrier signal to obtain the information symbols.

1.6 Noise Modelling and Photodetection

In optical communication, the receiver utilises photodetection. Photodetection is the process of converting optical radiation carrying information into its equivalent electrical signal in order to recover the transmitted data. The receiver's front-end components (telescope and optical filter) concentrate the filtered radiation onto the photodetection surface in the focal plane. PIN and APD are the two most widely used and popular optical receivers [44].

The PIN photodetector is composed of p-type and n-type semiconducting materials that are separated by an intrinsic region that is very lightly n-doped. In a PIN photodetector, the incident photon employs its energy to excite an electron from the valence band to the conduction band, thereby producing a free electron-hole pair. This results in the flow of current in an external circuit. Typically, the PIN detector's responsivity is either unity or less than unity. In contrast to the PIN photodetector, the APD provides an inherent current gain through a process known as repeated electron ionisation. This increases the sensitivity because the photocurrent is now multiplied prior to encountering the thermal noise of the receiver circuit. Typically, APD responsivity is greater than unity [45].

PIN photodetectors are thermally limited PD receivers that are compatible with OWC systems that operate over a few kilometres. Thermal and background noise comprise the PIN photodetector's noise. Due to the ozone layer's absorption of the UV wave, it is possible to disregard background noise in the case of UV. Consequently, terminal-noise is the only factor that must be addressed in the case of UVC receivers employing PIN photodetector. APD receivers, on the other hand, are photon-counting-receivers that are ideally suited for very long distances due to their enhanced output current gain. This additional gain is however accompanied by multiplicative noise, an increase in circuit complexity, and a rise in power consumption [45].

In this thesis, thermal noise limited PIN photodetectors over photon-counting APD receivers is used due to our considered maximum UV link distance of 1 km, negligible background noise, and less complex and energy-efficient receivers.

1.7 Performance Measures

Performance measures are used to examine the performance of a wireless communication system over different channel characteristics, fading conditions, and system configurations. These measures play an important role in identifying any design issues in the underlying system, and also assist in identifying the best operating conditions for its optimal performance. Commonly used performance measures in wireless communication are instantaneous SNR, outage probability, average symbol error rate (ASER), diversity order, and ergodic capacity.

1. **Instantaneous SNR:** Instantaneous SNR is the most fundamental measure used to quantify the signal distortion due to noise. It is measured at the output of receiver and determines the overall fidelity of the communication system. Instantaneous SNR is calculated as

$$\chi = \frac{\text{Received signal power}}{\text{Noise power at the receiver}} = \chi_{\circ}|h|^2, \tag{1.18}$$

where $\chi_{\circ}$ represents the average received SNR in the absence of fading, and h is the fading channel coefficient.

2. **Outage Probability:** Outage probability is defined as the probability of instantaneous SNR of the system falling below a predefined threshold (χ_{th}).

$$\begin{aligned} P_{out}(\chi_{th}) &= \Pr[\chi \leq \chi_{th}] = \int_0^{\chi_{th}} f_{\chi}(\chi) d\chi \\ &= F_{\chi}(\chi_{th}) \end{aligned} \tag{1.19}$$

where $f_{\chi}(\chi)$ is the PDF of χ. $F_{\chi}(\chi_{th})$ is the cumulative density function (CDF) of χ evaluated at χ_{th}.

3. **Average symbol error rate (ASER):** ASER is an important performance measure for wireless communication system. Using PDF based approach,

ASER of the underlying system is computed as

$$P_s(e) = \int_0^\infty P_s(e|\chi) f_\chi(\chi) d\chi, \tag{1.20}$$

where $P_s(e|\chi)$ is the conditional SER of the selected modulation scheme for a given χ.

4. **Diversity order:** Diversity order is an important metric to evaluate comparative performance of multi-relay wireless communication systems for different number of relays [12, 34, 46]. The conventional diversity order of a lognormally distributed fading channel does not converge to a finite value. In such case, relative diversity order (RDO) is computed as a useful measure to quantify the diversity advantage of a system as compared to some benchmark scheme. RDO was first introduced in [47] and thereafter widely adopted in the cooperative communication literature involving LN fading channels [12, 48, 49]. For systems incorporating multiple relays, non-relayed (SD link) is typically considered as the benchmark scheme [12]. With this consideration, the RDO of the system is defined as,

$$\text{RDO} = \frac{\partial \ln P_{out} / \partial \ln \chi_\circ}{\partial \ln P_{out}^{sd} / \partial \ln \chi_\circ}, \tag{1.21}$$

where P_{out}^{sd} is the outage probability of non-relayed SD link.

5. **Ergodic capacity:** Ergodic capacity is the maximum rate that can be communicated through a fading channel given a transmission strategy based solely on the fading distribution, averaged over all channel realizations [14]. Ergodic capacity is computed by averaging the instantaneous capacity over PDF Of instantaneous SNR of the system.

$$\begin{aligned} \mathcal{C}_e &= \mathbb{E}[\log_2(1+\chi)] \\ &= \int_0^\infty \log_2(1+\chi) f_\chi(\chi) d\chi \quad \text{bits/sec/Hz}. \end{aligned} \tag{1.22}$$

1.8 Motivation and Objectives

In this section, we present the motivation and objectives behind research work in this thesis.

1.8.1 Motivation

As discussed earlier in this chapter, UVC offers alternative system advantages and overcomes several limitation of conventional OWC technologies including FSO and VLC. It is worthwhile to re-iterate that the UVC has the ability to operate in NLOS mode which makes it a unique choice for scenarios where RF is prohibited and, FSO and VLC can not be used due to non-availability of LOS. Additionally, extremely low background noise due to absorption of UV wave by ozone layer allows the use of large FOV thereby improving SNR at the receiver [1, 3]. In spite of several advantages offered by NLOS UVC, it suffers from a very high path loss, turbulence induced fading, and limited data rate due to low-modulation speed of UV LEDs [23]. These shortcomings of of NLOS UVC restricts its usage to low-data rate applications over smaller distances. This research work is an attempt to address these challenges of NLOS UVC by making it suitable for long distance outdoor communication, and high-data rate applications.

Spatial diversity and cooperative relaying are the well established and proven techniques to mitigate the adverse effect of fading and to increase the communication range of wireless systems. The effectiveness of the spatial diversity to improve system capacity, coverage area and also to combats fading has been demonstrated in the seminal works from RF domain [50–52]. The cooperative relaying has gained enormous attention in current and future wireless systems due to its improved spectral efficiency, enhanced coverage and link capacity. Cooperative relaying has been considered in IEEE 802.16j/m, 3GPP LTE-Advanced and can be viewed as a promising solution for 5G and beyond systems [21, 22, 53]. Over the past few years, these techniques are widely being adopted in OWC systems operating in IR and VL band.

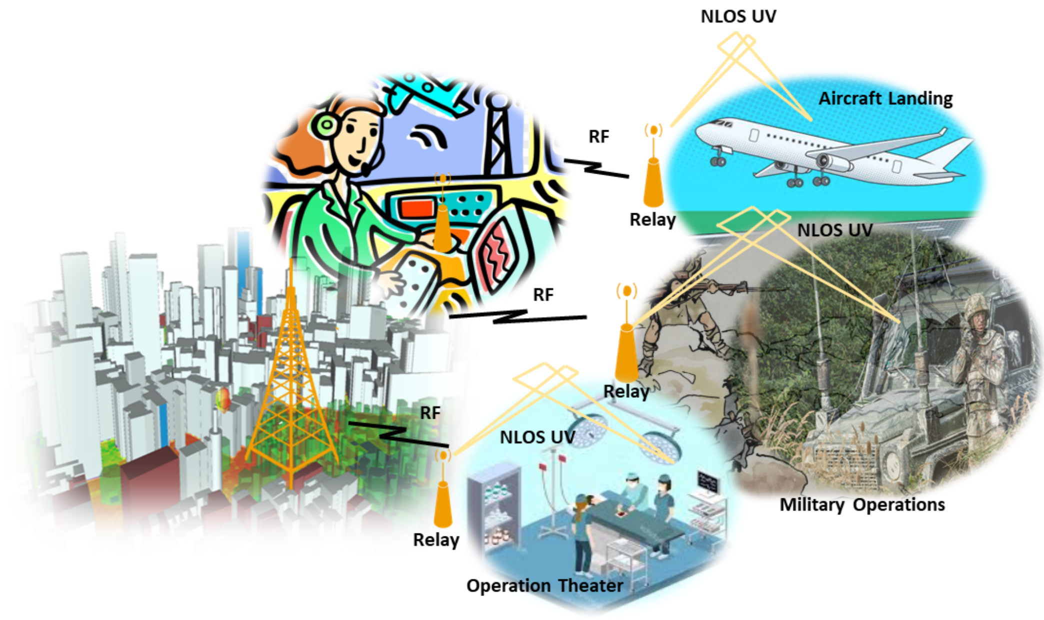

Figure 1.7: Applications of hybrid RF/NLOS UVC system.

However, the literature exploiting these techniques in the context of UVC is rather limited. Incorporating these techniques in NLOS UVC system and showing their effectiveness towards addressing the challenges of UVC is highly motivated.

Additionally, there are numerous applications where RF communication must be extended into areas where RF is restricted due to high-security requirements or to avoid interference with RF equipment. A hybrid RF/OWC system can meet these requirements by utilizing optical wireless links for RF prohibited areas. There is an extensive research literature exists on the hybrid RF/FSO and RF/VLC systems [40, 54–57]. However, due to the stringent LOS requirement posed by the FSO and VLC, these hybrid systems are rendered ineffective when the RF prohibited area lacks LOS connectivity. As a result, long-distance wireless connectivity to RF prohibited areas with no LOS presents a significant challenge that requires attention. A highly motivated solution to this problem is to use hybrid RF/NLOS UVC system, thereby leveraging the benefits of NLOS UVC for the optical link as shown in Fig. 1.7.

On the other front, the low modulation speed of UV LEDs limits the data-rate of UVC systems [23]. The higher-order modulation schemes, such as QAM and its variants including SQAM, RQAM, XQAM, and HQAM has gained increased research attention due to their high power, and bandwidth efficiency in RF communication systems. These complex modulation techniques can be incorporated in OWC through the use of SIM technique [38, 43, 58]. Using these futuristic modulation techniques is an effective way to address the low-data rate challenge of UVC. Therefore, it is worthwhile to explore the performance of these modulation schemes in NLOS UVC systems. Further, channel state information (CSI) plays a vital role in the equalization process at the receiver. However, perfect knowledge of CSI at the receiving node is rarely available in practice. This leads to channel estimation error (CEE), which has significant detrimental impact on the system's performance [56, 59]. Hence, from the real system design perspective, it is highly motivated to analyze the effect of CEE on the system performance.

1.8.2 Objectives

The challenges associated with NLOS UVC indicated in the previous subsection encouraged this thesis to pursue the following objectives:

- To employ spatial diversity to mitigate the fading caused by turbulence in an NLOS UVC system and to investigate the effect of channel correlation on system performance.
- To incorporate cooperative relaying in NLOS UVC system to enable long-distance outdoor UV communication.
- To evaluate the performance of a hybrid RF/NLOS UVC system in order to address the issue of providing long-distance RF connectivity to RF-prohibited areas with no LOS availability.
- To improve the data rate of the NLOS UVC system by utilizing SIM-based higher order modulation schemes and to conduct a thorough analysis of the ASER performance.

- To study the impact of CEE on the performance of proposed cooperative NLOS UVC systems, and hybrid RF/NLOS UVC system.

In view of the above stated objectives, this thesis is an attempt to pursue a unified study of the performance of NLOS UVC systems employing spatial diversity, cooperative relaying, and hybrid techniques. This research highlights some deeper practical insights to optimize physical-layer design features by assessing the trade-offs in system performance through system configurations, turbulence characteristics, and the complexity involved. The derived analytical expressions and the inferences drawn, obviate the necessity for computationally intensive and time-consuming Monte-Carlo simulations.

1.9 Thesis outline and contributions

The thesis is organized in 6 chapters, which are briefly described with their contributions as follows:

Chapter 1. Introduction: section 1 briefly describes different OWC technologies, ultraviolet communication, NLOS UVC channel model, cooperative communications, various higher order modulation schemes, important performance measures, and finally, the motivation and major contributions of the work presented in the thesis.

Chapter 2. Performance Analysis of NLOS Ultraviolet Communications in Turbulent Channel: In this section, an NLOS UVC system experiencing turbulence due to variation in the refractive index of the atmosphere is considered. A spatial diversity reception in the form of N_r-branches SC at the receiver is adopted. The channel coefficients are assumed to be exponentially correlated, and turbulence is modeled using LN distribution under weak turbulence conditions. Closed-form expressions for the outage probability and ASER for general order RQAM, XQAM, and HQAM schemes are derived. Furthermore, the ergodic capacity of the system is computed as a function of the channel correlation coefficient. The impact of varying number of receiver branches, and channel correlation on the system performance is evaluated and useful insights are drawn.

Chapter 3. Performance Analysis of AF Relayed Cooperative NLOS UVC System in the Presence of Turbulence: This section presents an effective AF based cooperative multi-relay system to combat the effect of both path loss and fading in NLOS UVC. Performance of the proposed system is analyzed in terms of outage probability by considering both variable-gain and fixed-gain AF relaying. Further, higher-order modulation schemes are employed to improve the data rate of the system. Innovative closed-form expressions of the ASER and diversity order are derived. The performance gains of the considered multi-relay system over non-relayed links for different system configurations are demonstrated.

Chapter 4. Impact of CSI Imperfections on Multiple Relay DF NLOS UVC Systems: In this section, a DF based best-relay selection cooperative relaying technique is proposed to improve the performance of NLOS UVC system and to extend its communication range. The practical case of imperfect CSI is considered at the receiver and the outage probability of the system is derived. The impact of elevation angles, receiver FOV, and turbulence strength on the system performance is studied. The RDO analysis of the system is conducted and the convergence of RDO through asymptotic analysis is presented. Further, the novel analytical expressions of ASER is derived for RQAM, XQAM, and futuristic HQAM schemes. A detailed performance study is carried out considering different system configurations and several interesting insights are highlighted, which reinforces UVC as a futuristic OWC technology.

Chapter 5. Relay Assisted Hybrid RF-NLOS UVC System with Imperfect Channel Estimation: In this section, the challenge of providing long distance wireless connectivity to RF prohibited areas is addressed by mixing NLOS UVC with RF communication using a DF relay. The RF link is modeled using Rayleigh distribution, and the NLOS UV link is modeled using LN distribution under weak turbulence conditions. Framework for analytical expressions of outage probability and PDF of the e2e SNR is presented by considering the practical scenario of imperfect CSI at the receiver. Subsequently, novel closed-form analytical expressions of ASER is deduced for spectrally-efficient higher-order modulation schemes including RQAM, SQAM, XQAM, and HQAM. Numerical investigations are conducted, and the impact of CSI imperfections on the system performance is evaluated.

Chapter 6. Conclusions and Future Works: This section summarizes all the contributions of the thesis along with the crucial insights and conclusions. Additionally, the scope of future works is outlined in this section.

Chapter 2

Performance Analysis of NLOS Ultraviolet Communications in Turbulent Channel

2.1 Introduction

UVC is becoming increasingly popular due to its inherent NLOS connectivity, high security, and abundant unlicensed spectrum availability. NLOS nature of the UV channel makes it a perfect solution for applications where LOS is not possible and RF communication is prohibited, for example, in aircrafts, hospitals, and covert operations. UVC suffers from high path loss due to underlying scattering and absorption, thus, restricting its usage to short communication range [29]. In addition, as the communication range increases, the turbulence induced fading further deteriorates the performance of the UV link [12].

Spatial diversity has been demonstrated to be an effective and commonly used strategy for mitigating the effect of fading and boosting communication system performance. There are various techniques proposed in the literature to introduce spatial diversity in NLOS UVC systems thereby making it suitable for long distance outdoor communication [12, 25, 29]. In [29] an experimental testbed is set up to study the effect of diversity reception in an NLOS UVC system with EGC used at the receiver. In [12], the authors conducted the performance analysis of an NLOS UVC system using cooperative communication techniques to achieve diversity; MRC is used at the receiver to combine the signal received via multi-hop relayed path and direct path. In [25], multiple photo-detectors are used to achieve diversity; channel coefficients are assumed to follow gamma-gamma distribution and switched-and-stay combining (SSC) technique is used at the receiver.

Due to the low modulation speed of LEDs operating in the deep UV region [23], UVC has a limited data transfer rate. It is highly desirable to adopt higher order modulation schemes to increase the data rate of NLOS UVC systems. In the existing literature, the performance analysis for UVC is generally limited to OOK modulation scheme, due to its simplicity [25–30]. QAM, on the other hand, is a general modulation technique that has gained widespread popularity due to its efficiency and generic nature. Different variations of QAM, such as RQAM, SQAM, XQAM, and HQAM are described in Section 1.4. These modulation schemes are extensively studied in RF based communication systems [33, 60]. However, detailed performance analysis of these modulation schemes in the context of NLOS UVC is least explored.

In this chapter, novel closed-form expressions for the outage probability, and ASER of a single-input-multiple-output (SIMO) NLOS UVC system are derived. The multiple receiver branches are assumed to be correlated, and SC is used at the receiver to achieve spatial diversity. The PDF of the instantaneous SNR at the output of selection combiner is computed. The computed PDF expression is used to derive the novel and generic ASER expression. This generic expression is then used to compute the ASER for RQAM, XQAM and HQAM schemes. The ergodic capacity of the considered system is derived and effect of channel correlation on the ergodic capacity is studied. Performance of the considered QAM schemes is investigated for different channel conditions, and useful inferences are drawn. It is shown that the system performance deteriorates with the increase in channel correlation due to the loss of diversity. The derived expressions are validated by Monte-Carlo simulations.

2.2 System Model

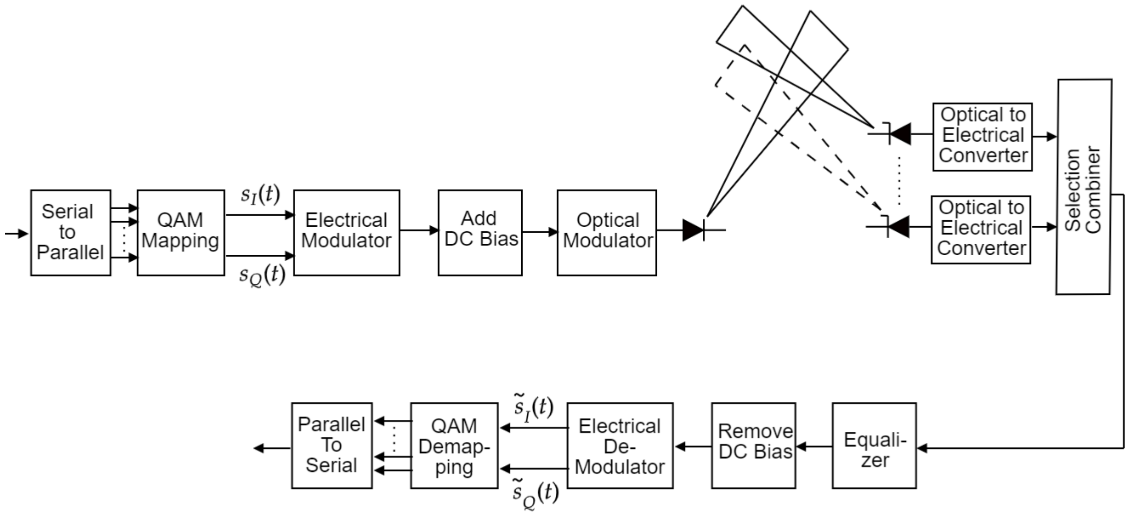

Figure 2.1: Selection combiner with N_r receiver branches

Fig. 2.1 dipicts an NLOS UVC system with N_r branches and SC at the receiver. At the transmitter, SIM is employed in which the information symbols are first modulated in the electrical domain. The DC bias is added to the electrically modulated signal. Finally, optical modulation is performed and the resultant optical signal is transmitted via NLOS UVC channel. The transmitted optical signal is received at the receiver after being distorted by the turbulence. N_r receiver branches are employed to achieve diversity. Each receiver branch is equipped with a photodetector that converts the optical power received into an electrical signal. The resultant electrical signal is passed to a selection combiner, which receives N_r copies of the detected electrical signal and selects the one with maximum SNR for further processing. The output of the selection combiner is fed to the equalizer, which employs the zero-forcing technique to eliminate the effect of channel. It is assumed that the CSI is completely known at the receiver. Next, DC-bias is removed and detection is performed to retrieve the QAM symbols. Finally, detected QAM symbols are demapped to parallel bit stream which is then converted into the serial information bits.

Let the received electrical signal corresponding to the i^{th} branch of the receiver is given by,

$$y_i = \eta P_r^{NLOS} h_i s + \nu_i, \quad i = 1, 2, \ldots, N_r \tag{2.1}$$

where s is the source symbol with average energy, $\mathbb{E}[|s|^2]$, normalized to 1. P_r^{NLOS} represents the received optical power at the receiver via i^{th} path under single scattering assumption in the absence of turbulence and w_i is the signal-independent noise modeled as zero mean AWGN [12, 25, 61] with variance σ_ν^2. h_i is the turbulence induced fading channel coefficient of the i^{th} path which follows LN distribution for weak turbulence. For mathematical tractability, the same elevation angle at all receiver branches is considered which means that the transmitter and all the receivers are looking at the same CV. As a result, the channel coefficients $\{h_i\}_{i=1}^{N_r}$ follows identical distribution, $\ln h_i \sim \mathcal{N}(\mu_h, \sigma_h^2)$. The channels experienced by different receiver branches are assumed to be exponentially correlated [25]. The covariance matrix of $\boldsymbol{h} = [h_1, h_2, \ldots h_{N_r}]^T$ is given by

$$\boldsymbol{\Upsilon_h} = \sigma_h^2 \begin{bmatrix} 1 & \upsilon & \ldots & \upsilon^{N_r-1} \\ \upsilon & 1 & \ldots & \upsilon^{N_r-2} \\ \vdots & \vdots & \ddots & \vdots \\ \upsilon^{N_r-1} & \upsilon^{N_r-2} & \ldots & 1 \end{bmatrix}. \tag{2.2}$$

The correlation coefficient between any two channel coefficients is given as

$$\upsilon^{|j-k|} = \mathbb{E}\Big[\frac{(h_j - m_h)(h_k - m_h))}{\sigma_h^2}\Big], \; j \neq k \tag{2.3}$$

with $m_h = \exp\Big(\mu_h + \frac{\sigma_h^2}{2}\Big)$.

Let χ_i is the instantaneous electrical SNR of the i^{th} receiver branch which is given by

$$\chi_i = \frac{\eta^2 P_r^{NLOS^2} h_i^2}{\sigma_\nu^2}. \tag{2.4}$$

The average received electrical SNR per symbol at any branch in the absence of turbulence is given as,

$$\chi_{\circ} = \frac{\eta^2 P_r^{NLOS^2}}{\sigma_\nu^2}. \tag{2.5}$$

Using the properties of LN distribution, it can be shown that the instantaneous SNR (χ_i) also follows LN distribution, $\ln(\chi_i) \sim \mathcal{N}(\mu_\chi, \sigma_\chi^2)$. The mean and variance of $\ln(\chi_i)$ can be computed as,

$$\mu_\chi = 2\mu_h + \ln(\chi_\circ), \quad \sigma_\chi^2 = 4\sigma_h^2. \tag{2.6}$$

Let $\boldsymbol{\chi} = [\chi_1, \chi_2, \ldots, \chi_{N_r}]^T$, then the joint pdf of $\boldsymbol{\chi}$ is given as

$$f_{\boldsymbol{\chi}}(\boldsymbol{\chi}) = \frac{\exp\left[-\frac{1}{2}(\ln \boldsymbol{\chi} - \boldsymbol{\mu}_\chi)^T \boldsymbol{\Upsilon}_\chi^{-1}(\ln \boldsymbol{\chi} - \boldsymbol{\mu}_\chi)\right]}{(2\pi)^{N_r/2}|\boldsymbol{\Upsilon}_\chi|^{1/2}\chi_1\chi_2\cdots\chi_{N_r}}. \tag{2.7}$$

Here $\boldsymbol{\mu}_{\boldsymbol{\chi}} = \mu_\chi[1, 1, \ldots, 1]^T$ is a $N_r \times 1$ vector and covariance matrix $\boldsymbol{\Upsilon}_{\boldsymbol{\chi}}$ is given as

$$\boldsymbol{\Upsilon}_{\boldsymbol{\chi}} = \sigma_\chi^2 \begin{bmatrix} 1 & \upsilon & \ldots & \upsilon^{N_r-1} \\ \upsilon & 1 & \ldots & \upsilon^{N_r-2} \\ \vdots & \vdots & \ddots & \vdots \\ \upsilon^{N_r-1} & \upsilon^{N_r-2} & \ldots & 1 \end{bmatrix}. \tag{2.8}$$

SC is employed to achieve receiver diversity. There are other combining schemes such as MRC and EGC, which has better performance as compared to SC. However, the improved performance is achieved at the cost of increased receiver complexity. In SC, only the branch with maximum SNR is selected for signal detection, thus, simplifying the receiver structure for practical deployments. The instantaneous SNR at the output of the selection combiner is given as

$$\chi_{sc} = \max(\chi_1, \chi_2, \ldots, \chi_{N_r}). \tag{2.9}$$

In the following section, the CDF and PDF expressions for χ_{sc} are derived.

2.3 Outage Analysis

In this section, the closed-form expression of the outage probability of the considered system is obtained. As stated in Section 1.7, the outage probability is defined as

$$P_{out}(\chi_{th}) = \Pr\left[\chi_{sc} < \chi_{th}\right] = F_{\chi_{sc}}(\chi_{th}), \tag{2.10}$$

where $F_{\chi_{sc}}(\cdot)$ is the CDF of χ_{sc}. Invoking (2.9) into (2.10), we get

$$P_{out}(\chi_{th}) = \underbrace{\int_0^{\chi_{th}} \cdots \int_0^{\chi_{th}}}_{N_r \text{ Integrals}} f_{\boldsymbol{\chi}}(\boldsymbol{\chi}) d\chi_1 d\chi_2 \dots d\chi_{N_r}. \tag{2.11}$$

Using $f_{\boldsymbol{\chi}}(\boldsymbol{\chi})$ from (2.7) into (2.11) results in

$$P_{out}(\chi_{th}) = \int_0^{\chi_{th}} \cdots \int_0^{\chi_{th}} \frac{\exp\left[-\frac{1}{2}(\ln \boldsymbol{\chi} - \boldsymbol{\mu}_{\boldsymbol{\chi}})^T \boldsymbol{\Upsilon}_{\boldsymbol{\chi}}^{-1} (\ln \boldsymbol{\chi} - \boldsymbol{\mu}_{\boldsymbol{\chi}})\right]}{(2\pi)^{N_r/2} |\boldsymbol{\Upsilon}_{\boldsymbol{\chi}}|^{1/2} \chi_1 \chi_2 \dots \chi_{N_r}} d\chi_1 d\chi_2 \dots d\chi_{N_r}. \tag{2.12}$$

Substituting $\boldsymbol{y} = \ln(\boldsymbol{\chi})$ into (2.12) results in

$$P_{out}(\chi_{th}) = \int_{-\infty}^{\ln(\chi_{th})} \cdots \int_{-\infty}^{\ln(\chi_{th})} \overbrace{\frac{\exp\left[-\frac{1}{2}(\boldsymbol{y} - \boldsymbol{\mu}_{\boldsymbol{\chi}})^T \boldsymbol{\Upsilon}_{\boldsymbol{\chi}}^{-1} (\boldsymbol{y} - \boldsymbol{\mu}_{\boldsymbol{\chi}})\right]}{(2\pi)^{N_r/2} |\boldsymbol{\Upsilon}_{\boldsymbol{\chi}}|^{1/2}}}^{f_{\boldsymbol{y}}(\boldsymbol{y})} dy_1 dy_2 \dots dy_{N_r}, \tag{2.13}$$

where $f_{\boldsymbol{y}}(\boldsymbol{y})$ is the PDF of the multivariate Gaussian random variable, $\boldsymbol{y} = [y_1, y_2, \dots, y_{N_r}]^T$, with mean vector $\boldsymbol{\mu}_{\boldsymbol{\chi}}$ and covariance matrix $\boldsymbol{\Upsilon}_{\boldsymbol{\chi}}$. The random variables $\{y_i\}_{i=1}^{N_r}$ can be obtained from $N_r + 1$ independent Gaussian random variables $Z_1, Z_2, \dots, Z_{N_r}; V$

using the following transformation [62]

$$y_k = \sigma_\chi[\sqrt{1-\upsilon'}Z_k + \sqrt{\upsilon'}V] + \mu_\chi, \quad k = 1, 2, \ldots, N_r \tag{2.14}$$

where $Z_k, V \sim \mathcal{N}(0, 1)$. υ' is obtained by approximating the covariance matrix given in (2.8) as

$$\boldsymbol{\Upsilon_\chi} \approx \boldsymbol{\Upsilon'_\chi} = \sigma_\chi^2 \begin{bmatrix} 1 & \upsilon' & \ldots & \upsilon' \\ \upsilon' & 1 & \ldots & \upsilon' \\ \vdots & \vdots & \ddots & \vdots \\ \upsilon' & \upsilon' & \ldots & 1 \end{bmatrix}, \tag{2.15}$$

where υ' is computed by minimizing the Frobenius norm of the vector $[\upsilon' - \upsilon, \upsilon' - \upsilon^2, \ldots, \upsilon' - \upsilon^{N_r-1}]^T$ resulting in $\sum_{i=1}^{N_r-1}(\upsilon^i - \upsilon') = 0$. On solving this equation, the following expression is obtained

$$\upsilon' = \frac{\upsilon(1-\upsilon^{N_r-1})}{(N_r-1)(1-\upsilon)} \quad \text{for } N_r > 1. \tag{2.16}$$

The transformation given in (2.14) is applied to (2.13) to obtain

$$\begin{aligned} P_{out}(\chi_{th}) = \int_{-\infty}^{\infty} & F_{Z_1}\left(\frac{\ln \chi_{th} - \mu_\chi - \sqrt{\upsilon'\sigma_\chi^2}\,v}{\sqrt{\sigma_\chi^2(1-\upsilon')}}\right) \\ & \times \ldots \times F_{Z_{N_r-1}}\left(\frac{\ln \chi_{th} - \mu_\chi - \sqrt{\upsilon'\sigma_\chi^2}\,v}{\sqrt{\sigma_\chi^2(1-\upsilon')}}\right) f_V(v)dv. \end{aligned} \tag{2.17}$$

Substituting the PDF and CDF expressions for standard normal distribution into (2.17) and using the transformation $v/\sqrt{2} = u$ results in

$$P_{out}(\chi_{th}) = \frac{1}{\sqrt{\pi}} \int_{-\infty}^{\infty} \left[1 - Q\left(\frac{\ln \chi_{th} - \mu_\chi - \sqrt{2\upsilon'\sigma_\chi^2}\,u}{\sqrt{\sigma_\chi^2(1-\upsilon')}}\right)\right]^{N_r} e^{-u^2} du. \tag{2.18}$$

Integral in (2.18) can be evaluated using Gauss Hermite quadrature integration technique [63, Table 25.10] as

$$P_{out}(\chi_{th}) = \frac{1}{\sqrt{\pi}} \sum_{j=1}^{n} w_j \left[1 - Q\left(\frac{\ln \chi_{th} - \mu_\chi - \sqrt{2\upsilon' \sigma_\chi^2}\, u_j}{\sqrt{\sigma_\chi^2 (1-\upsilon')}} \right) \right]^{N_r}, \tag{2.19}$$

where $Q(x) = \frac{1}{2\pi} \int_x^\infty e^{-t^2/2} dt$. w_j and u_j are the weight factors and zeros of n^{th} order Hermite polynomial, respectively. Differentiating (2.19) w.r.t. χ_{th} and replacing χ_{th} with χ for notational simplicity, results in the following PDF expression of χ_{sc}

$$\begin{aligned} f_{\chi_{sc}}(\chi) = & \frac{N_r}{\chi \pi \sqrt{2\sigma_\chi^2 (1-\upsilon')}} \sum_{j=1}^{n} w_j \left[1 - Q\left(\frac{\ln \chi - \mu_\chi - \sqrt{2\upsilon' \sigma_\chi^2}\, u_j}{\sqrt{\sigma_\chi^2 (1-\upsilon')}} \right) \right]^{N_r - 1} \\ & \times \exp\left[\frac{-(\ln \chi - \mu_\chi - \sqrt{2\upsilon' \sigma_\chi^2}\, u_j)^2}{2\sigma_\chi^2 (1-\upsilon')} \right]. \end{aligned} \tag{2.20}$$

2.4 ASER Analysis

In this section, PDF based approach is used to derive the generic expression for ASER. Let $P_s(e|\chi)$ represents the conditional probability of symbol error for AWGN channel. Thus, for a fading channel, ASER can be computed by averaging $P_s(e|\chi)$ over χ as

$$P_s(e) = \int_0^\infty P_s(e|\chi) f_{\chi_{sc}}(\chi) d\chi, \tag{2.21}$$

where $f_{\chi_{sc}}(\chi)$ represents the PDF of the e2e SNR. Using (2.20) into (2.21), we get

$$\begin{aligned} P_s(e) = & \frac{N_r}{\pi} \sum_{j=1}^{n} w_j \int_0^\infty \frac{1}{\chi \sqrt{2\sigma_\chi^2 (1-\upsilon')}} P_s(e|\chi) \\ & \times \left[1 - Q\left(\frac{\ln \chi - \mu_\chi - \sqrt{2\upsilon' \sigma_\chi^2}\, u_j}{\sqrt{\sigma_\chi^2 (1-\upsilon')}} \right) \right]^{N_r - 1} \exp\left(\frac{-(\ln \chi - \mu_\chi - \sqrt{2\upsilon' \sigma_\chi^2}\, u_j)^2}{2\sigma_\chi^2 (1-\upsilon')} \right) d\chi. \end{aligned} \tag{2.22}$$

Substituting $\upsilon = \frac{\ln\chi - \mu - \sqrt{2\upsilon'\sigma^2}u_j}{\sqrt{2\sigma^2(1-\upsilon')}}$ in (2.22) and simplifying, results in

$$P_s(e) = \frac{N_r}{\pi}\int_{-\infty}^{\infty}\sum_{j=1}^{n} w_j P_s\Big(e|\chi = \exp\big(\sqrt{2\sigma_\chi^2(1-\upsilon')}\ \upsilon + \mu_\chi + \sqrt{2\upsilon'\sigma_\chi^2}u_j\big)\Big) \times \Big[1 - Q(\sqrt{2}\ \upsilon)\Big]^{N_r-1}\exp\big(-\upsilon^2\big)d\upsilon. \tag{2.23}$$

On using Gauss Hermite quadrature integration in (2.23), we get

$$P_s(e) = \frac{N_r}{\pi}\sum_{k=1}^{n}\sum_{j=1}^{n} w_k w_j P_s\Big(e|\chi = \exp\big(\sqrt{2\sigma_\chi^2(1-\upsilon')}\ \upsilon_k + \mu_\chi + \sqrt{2\upsilon'\sigma_\chi^2}u_j\big)\Big) \times \Big[1 - Q(\sqrt{2}\ \upsilon_k)\Big]^{N_r-1}. \tag{2.24}$$

The expression in (2.24) is the generic ASER expression for the considered system, and is applicable to all modulation schemes.

2.4.1 Rectangular QAM Scheme

The conditional expression for the SER of $M_I \times M_Q$ RQAM over AWGN channel is described in (1.11) of Section 1.4.1. On substituting (1.11) into (2.24) results in the following final ASER expression for RQAM scheme.

$$\begin{aligned} P_s^{\mathrm{RQAM}}(e) = \frac{1}{\pi}\sum_{k=1}^{n}\sum_{j=1}^{n} w_k w_j \big[1 - Q(\sqrt{2}\ \upsilon_k)\big]^{N_r-1} \\ \times \Bigg\{2p_0 Q(a_0\sqrt{\exp\big(\sqrt{2\sigma_\chi^2(1-\upsilon')}\ \upsilon_k + \mu_\chi + \sqrt{2\upsilon'\sigma_\chi^2}u_j\big)} \\ + 2q_0 Q(b_0\sqrt{\exp\big(\sqrt{2\sigma_\chi^2(1-\upsilon')}\ \upsilon_k + \mu_\chi + \sqrt{2\upsilon'\sigma_\chi^2}u_j\big)} \\ - \Big[4p_0q_0 Q(a_0\sqrt{\exp\big(\sqrt{2\sigma_\chi^2(1-\upsilon')}\ \upsilon_k + \mu_\chi + \sqrt{2\upsilon'\sigma_\chi^2}u_j\big)} \\ \times Q(b_0\sqrt{\exp\big(\sqrt{2\sigma_\chi^2(1-\upsilon')}\ \upsilon_k + \mu_\chi + \sqrt{2\upsilon'\sigma_\chi^2}u_j\big)}\Big]\Bigg\} \end{aligned} \tag{2.25}$$

2.4.2 Hexagonal QAM Scheme

The conditional expression for the SER of HQAM over AWGN channel is given by (1.13) of Section 1.4.3. Substituting (1.13) into (2.24) and after mathematical simplifications, ASER expression of HQAM scheme for the considered system is computed as

$$\begin{aligned}
P_s^{\mathrm{HQAM}}(e) = {} & \frac{2}{\pi}\sum_{k=1}^{n}\sum_{j=1}^{n} w_k w_j \Big[1 - Q(\sqrt{2}\, v_k)\Big]^{N_r-1} \\
& \times \Bigg\{ D Q\left(\sqrt{q_1 \exp\left(\sqrt{2\sigma_\chi^2(1-\upsilon')}\, v_k + \mu_\chi + \sqrt{2\upsilon'\sigma_\chi^2} u_j\right)}\right) \\
& + \frac{2}{3} D_C Q^2\left(\sqrt{2q_1 \exp\left(\sqrt{2\sigma_\chi^2(1-\upsilon')}\, v_k + \mu_\chi + \sqrt{2\upsilon'\sigma_\chi^2} u_j\right)/3}\right) \\
& - 2D_C \Bigg[Q\left(\sqrt{q_1 \exp\left(\sqrt{2\sigma_\chi^2(1-\upsilon')}\, v_k + \mu_\chi + \sqrt{2\upsilon'\sigma_\chi^2} u_j\right)}\right) \\
& \times Q\left(\sqrt{q_1 \exp\left(\sqrt{2\sigma_\chi^2(1-\upsilon')}\, v_k + \mu_\chi + \sqrt{2\upsilon'\sigma_\chi^2} u_j\right)/3}\right) \Bigg] \Bigg\}.
\end{aligned} \tag{2.26}$$

2.4.3 Cross QAM Scheme

In this section, the ASER of XQAM scheme with 32 constellation points (XQAM-32) is derived. The conditional expression of the SER for XQAM-32 scheme is given by (1.12) of Section 1.4.2. Substituting (1.12) into (2.24) results in the ASER expression for XQAM-32 given by

$$\begin{aligned}
P_s^{\text{XQAM-32}}(e) = {} & \frac{1}{4\pi}\sum_{k=1}^{n}\sum_{j=1}^{n} w_k w_j \Big[1 - Q(\sqrt{2}\, v_k)\Big] \\
& \times \Bigg\{ 26 Q\left(\sqrt{2A \exp\left(\sqrt{2\sigma_\chi^2(1-\upsilon')}\, v_k + \mu_\chi + \sqrt{2\upsilon'\sigma_\chi^2} u_j\right.}\right) \\
& + Q\left(2\sqrt{A \exp\left(\sqrt{2\sigma_\chi^2(1-\upsilon')}\, v_k + \mu_\chi + \sqrt{2\upsilon'\sigma_\chi^2} u_j\right.}\right) \\
& - 23 Q^2\left(\sqrt{2A \exp\left(\sqrt{2\sigma_\chi^2(1-\upsilon')}\, v_k + \mu_\chi + \sqrt{2\upsilon'\sigma_\chi^2} u_j\right.}\right) \Bigg\}
\end{aligned} \tag{2.27}$$

2.5 Ergodic Capacity

In this section, the ergodic capacity of the system under consideration is derived. Ergodic capacity is an important performance metric, usually computed for the fast fading channels, to identify the data rate that can be achieved for a given system configuration. A UVC system operating in NLOS mode is very sensitive to atmospheric variations thus giving rise to fast fading [64]. From Shannon's capacity theorem [14], the ergodic capacity in bits/sec/Hz is computed as

$$\mathcal{C}_e = \int_0^{\infty} \log_2(1+\chi) f_{\chi_{sc}}(\chi) d\chi. \tag{2.28}$$

On substituting $f_{\chi_{sc}}(\chi)$ from (2.20) into (2.28) and following the steps similar to Section 2.4, the following expression for the ergodic capacity is obtained.

$$\begin{aligned}\mathcal{C}_e = \frac{N_r}{\pi} \sum_{k=1}^{n} \sum_{j=1}^{n} w_k w_j \Big[1 - Q(\sqrt{2}\, v_k)\Big]^{N_r - 1} \\ \log_2 \Big(1 + \exp\big(\sqrt{2\sigma_\chi^2 (1-\upsilon')}\, v_k + \mu_\chi + \sqrt{2\upsilon' \sigma_\chi^2} u_j\big)\Big).\end{aligned} \tag{2.29}$$

2.6 Numerical and Simulation Results

In this section, numerical analysis is conducted for the considered N_r-branches NLOS UVC system with selection combiner and validate the results through Monte-Carlo simulations. Unless otherwise stated, the system and channel configuration parameters given in Table 2.1 are considered for the numerical study [10, 12]. The number of terms (n) used to compute Gauss Hermite quadrature in (2.19), (2.25), (2.26), (2.27) and (2.29) is considered to be 20 for better numerical accuracy [64, 65].

Fig. 2.2(a) illustrates the theoretical and simulation results of outage probability for correlated channels ($\upsilon = 0.2, \upsilon = 0.8$). The SNR threshold χ_{th} is considered to be 4 dB [25]. It is observed that the theoretical results overlap with the simulation

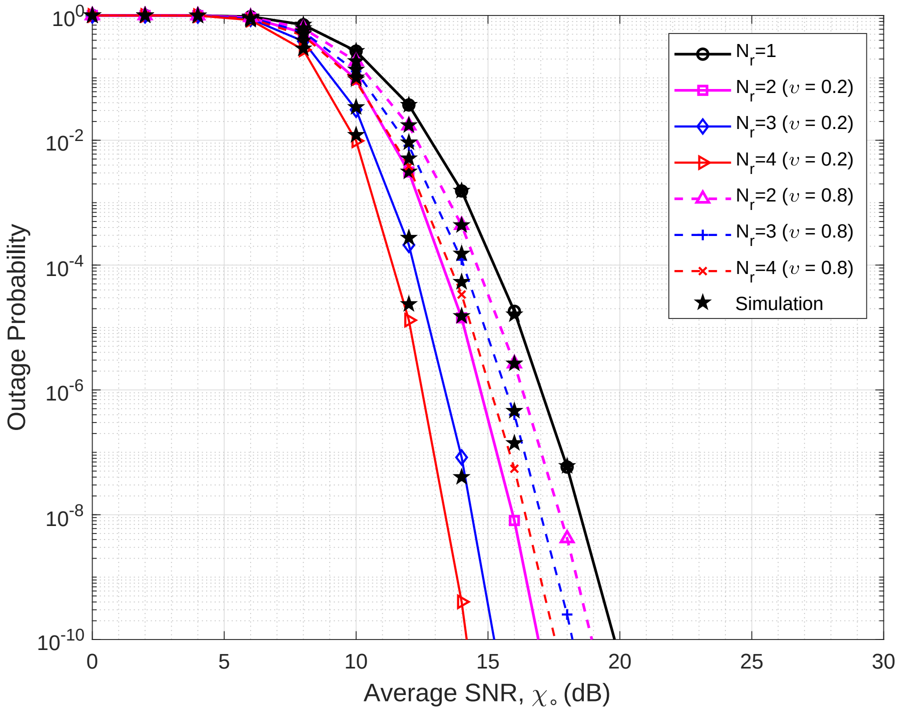

(a) Outage probability versus average SNR

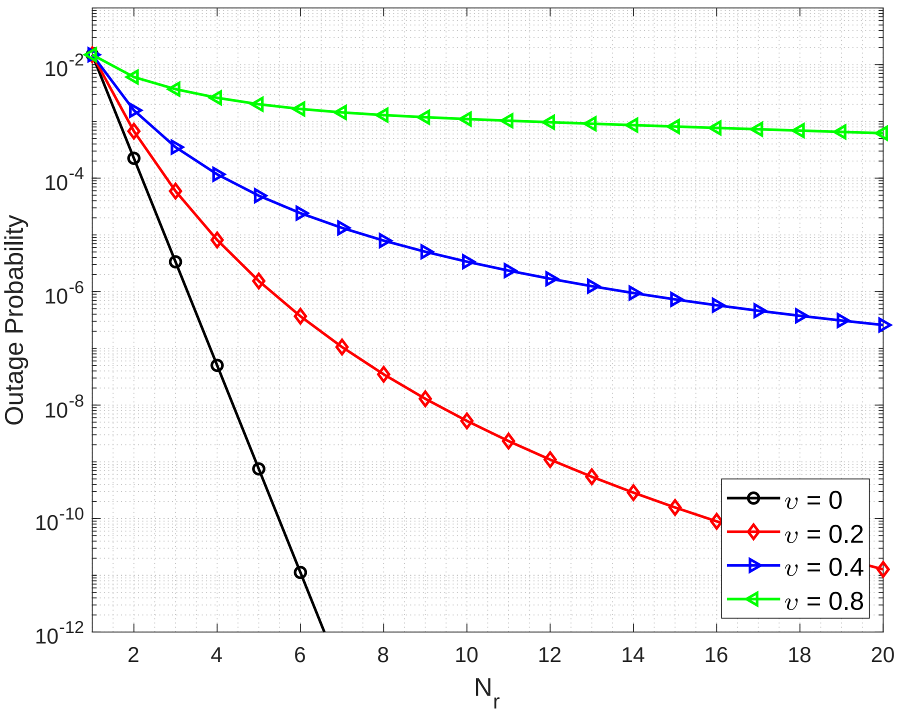

(b) Outage probability versus N_r ($\chi_\circ = 15$ dB)

Figure 2.2: Outage probability for $\chi_{th} = 4$ dB.

results for all the investigated cases, thus, confirming the accuracy of the derived expression of outage probability given in (2.19). It can be seen that the system

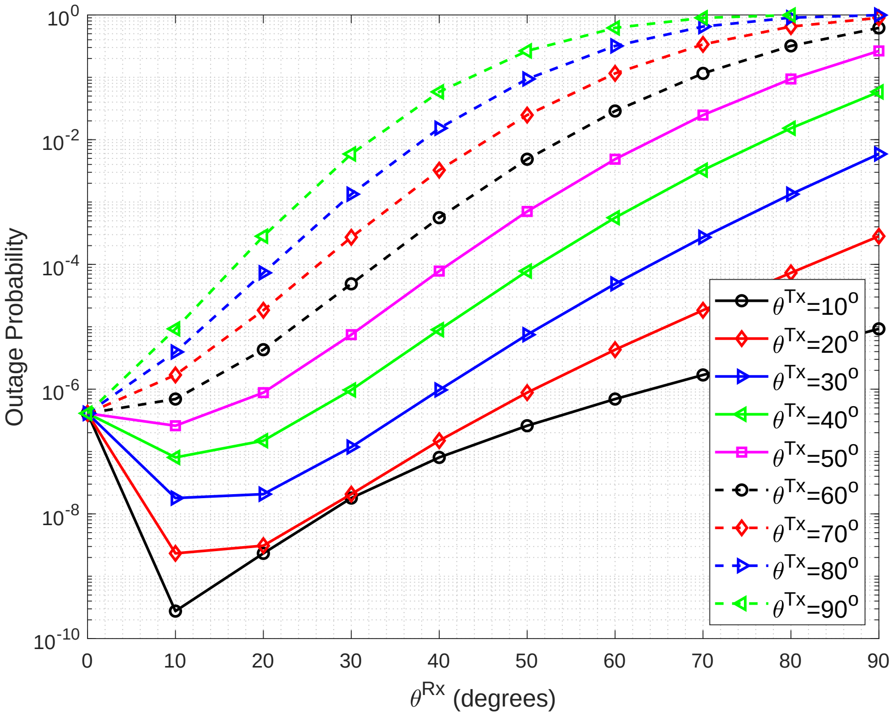

(c) Outage probability ($\upsilon = 0.4, \chi_\circ = 15$ dB$, N_r = 2$)

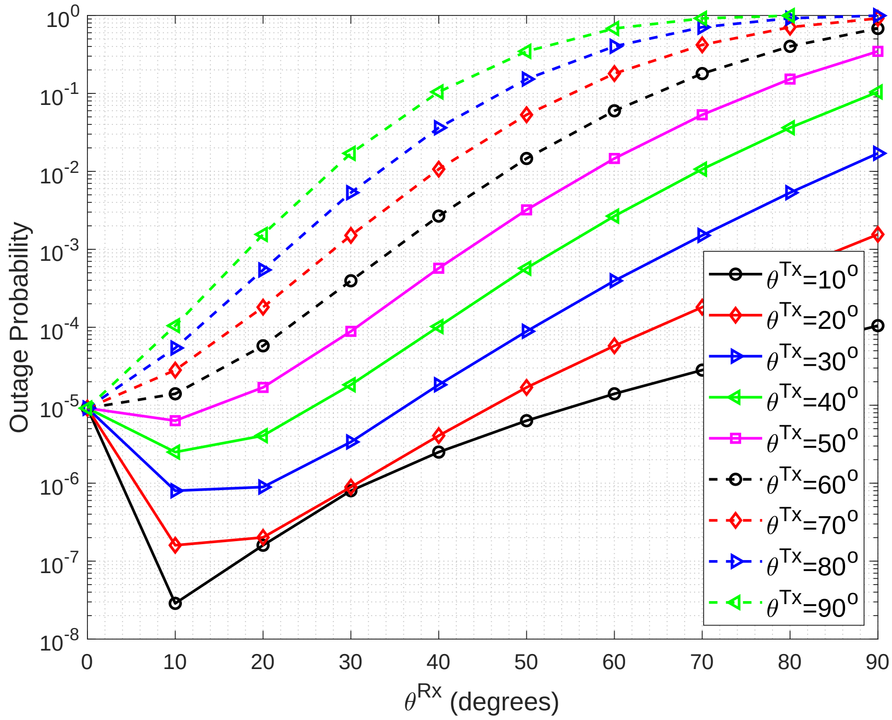

(d) Outage probability ($\upsilon = 0.8, \chi_\circ = 15$ dB$, N_r = 2$)

Figure 2.2: Outage probability for $\chi_{th} = 4$ dB (contd.).

performance degrades with the increase in correlation ($\upsilon > 0$). This is due to the fact that, for $\upsilon = 0$ the channels become independent and hence the system achieves

Table 2.1: System and Channel Configuration

Parameter	**Symbol**	**Value**
Wavelength	λ	260×10^{-9}m
Receiver aperture area	A_r	1.77 cm^2
Refractive index structure coefficient	C_n^2	1×10^{-15}m$^{-2/3}$
Rayleigh scattering coefficient	k_s^{Ray}	2.4×10^{-4} m^{-1}
Mie scattering coefficient	k_s^{Mie}	2.5×10^{-4} m^{-1}
Absorption coefficient	k_a	9×10^{-4} m^{-1}
Channel model parameters	γ, g, f	$0.017, 0.72, 0.5$ [10, 12]
Transmitter beam divergence	ϕ^{Tx}	8 mrd
Receiver FOV	ϕ^{Rx}	45°
Transmitter elevation angle	θ^{Tx}	30°
Receiver elevation angle	θ^{Rx}	30°
Distance between Tx and Rx	d	500 m [12, 66]

full diversity. However, as the channel correlation increases, the diversity order of the system reduces resulting in degraded system performance and increased outage probability. Fig. 2.2(b) shows the effect of increasing number of receiver branches on system performance for different channel correlations. It is observed that for uncorrelated channels, the outage probability increase linearly with N_r. However, as the correlation increases, increasing N_r beyond a certain number has limited performance improvement or no impact on the outage probability. Fig. 2.2(c) and 2.2(d) shows the impact of different transmitter and receiver elevation angles on the outage probability for $\upsilon = 0.4$ and 0.8, respectively. It can be observed that, irrespective of the channel correlation coefficient value, optimum performance is achieved for smaller elevation angles of $\sim 10°$. This is because, the smaller elevation angle reduces the distance from Tx and Rx to the CV, thus, reducing the signal attenuation. However, reducing the elevation angle below 10°, results in decreased CV area which leads to smaller number of photons being scattered towards the FOV of the receiver, thus, deteriorating the system performance.

In Fig. 2.3, the ASER performance of various QAM schemes, such as SQAM, RQAM, XQAM and HQAM, are studied for different constellation sizes and υ. It is observed that the theoretical curves overlap with the simulation results for all schemes which validate the theoretical analysis presented in Section 2.4. Fig. 2.3(a)

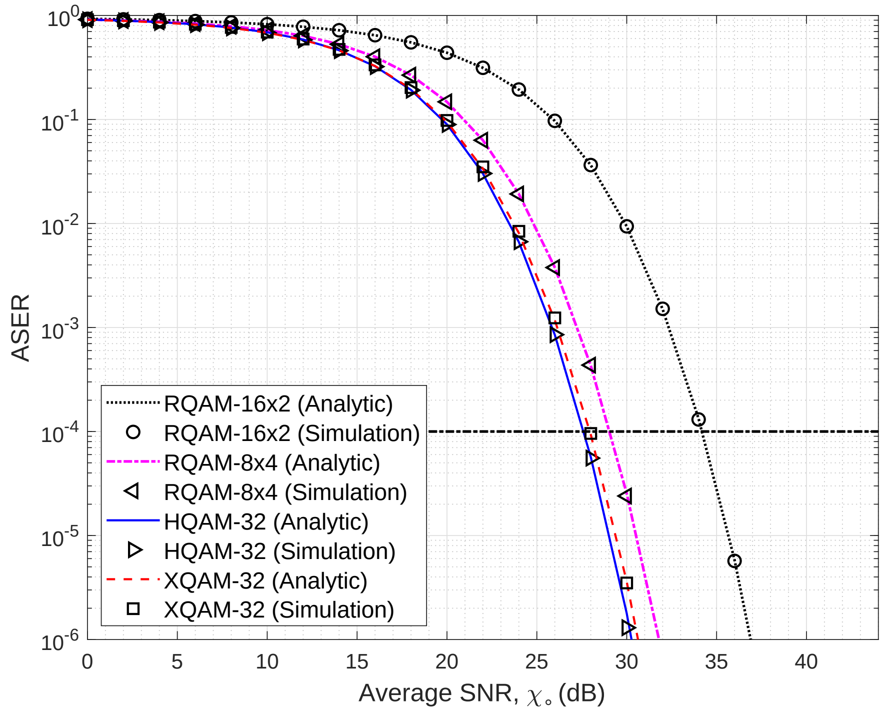

(a) 32-points constellations ($\upsilon = 0.8$)

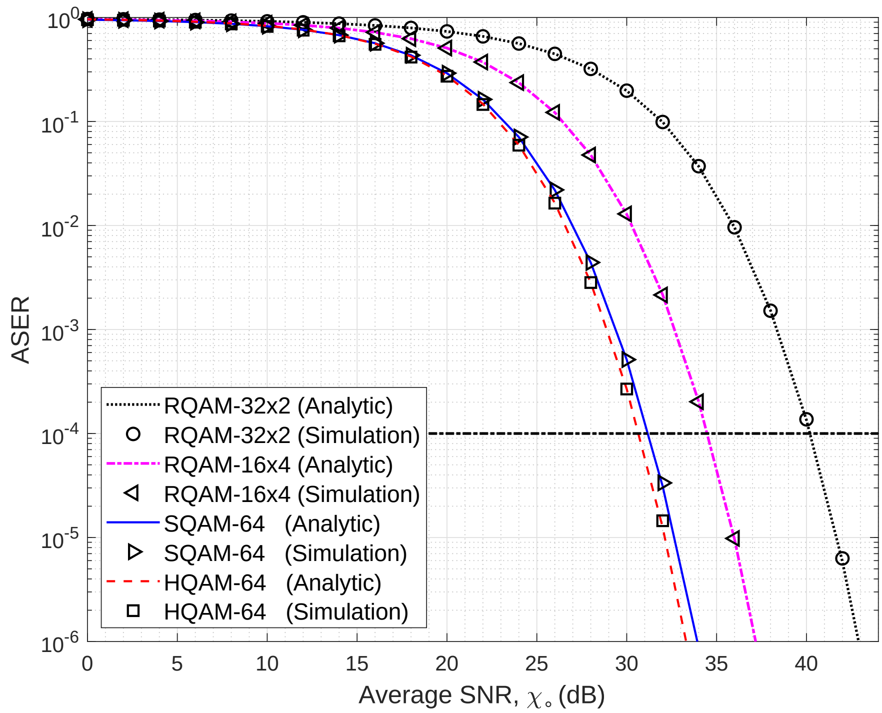

(b) 64-points constellations ($\upsilon = 0.8$)

Figure 2.3: Comparison of analytical and simulation results of ASER versus SNR for different modulation schemes.

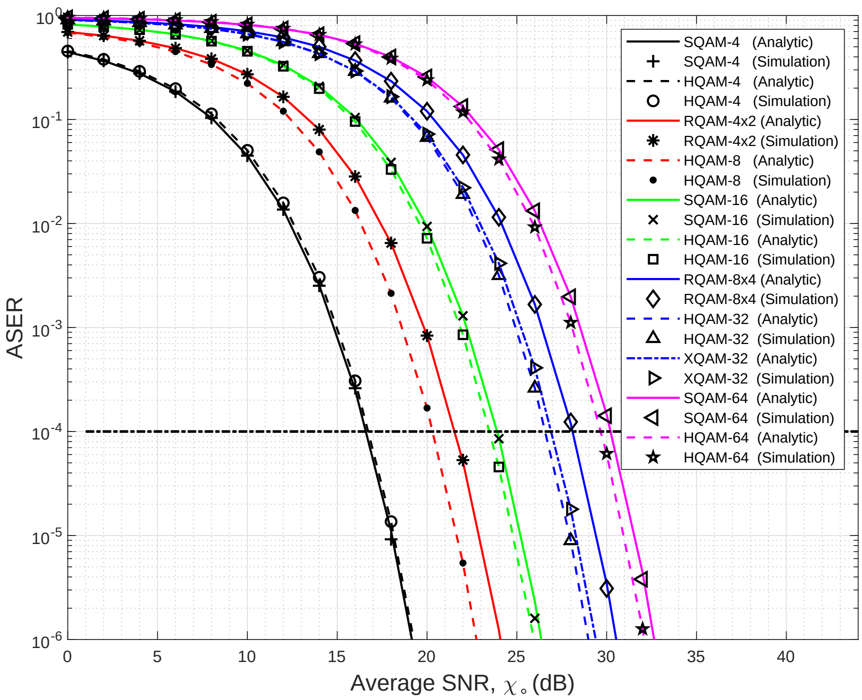

(c) $4, 8, 16, 32, 64$-points constellations ($\upsilon = 0$)

Figure 2.3: Comparison of analytical and simulation results of ASER versus SNR for different modulation schemes (contd.).

compares the simulation results for 32 points RQAM, HQAM and XQAM schemes for $\upsilon = 0.8$. Considering 10^{-4} as the target ASER, it is observed that RQAM-8×4 results in SNR gain of approx. 5.1 dB as compared to RQAM-16×2. Further, it is observed that XQAM-32 outperforms RQAM-8×4 scheme with a significant gain of ~ 1.1 dB. This is because of the lower peak and average power in XQAM as compared to RQAM. It is also observed that, HQAM-32 performs slightly better than XQAM-32 (~ 0.34 dB).

In Fig. 2.3(b), the ASER performance of RQAM-32×2, RQAM-16×4, SQAM-64 and HQAM-64 schemes is compared. It is observed that HQAM-64 performs better than SQAM-64, RQAM-32×2 and RQAM-16×4 modulation formats. For instance, to achieve ASER of 10^{-4} HQAM-64 requires approx. 0.6 dB lower SNR as compared to SQAM-64. Further, it can be inferred that, using SQAM-64 results in a significant gain of ~ 3.3 dB and ~ 8.9 dB as compared to RQAM-16×4 and RQAM-32×2 schemes, respectively. The reason for better performance of SQAM over non-square RQAM is that SQAM maximizes the minimum distance between the constellation points for a given energy, thus, requiring slightly less power as compared to non-square RQAM to achieve the target ASER.

Fig. 2.3(c) presents the ASER curves of different modulation schemes for $\upsilon = 0$ and constellation sizes of $4, 16, 32, 64$. It is observed that for a given constellation size, SQAM results in lower ASER as compared to RQAM. Further, it can be seen that SQAM-4 performs marginally better than HQAM-4. However, except for constellation size 4, HQAM always performs optimally, as compared to other modulation formats. As an example, for $\upsilon = 0$, HQAM-8, HQAM-16, HQAM-32 and HQAM-64 provides a significant gain of approx. 1.2 dB, 0.4 dB, 1.5 dB and 0.5 dB as compared to RQAM-4×2, SQAM-16, RQAM-8×4 and SQAM-64, respectively. As an important observation, XQAM-32 performs better than 32 points RQAM constellations, however, lags behind $\sim$ 0.3 dB SNR as compared to HQAM-32 to achieve the target ASER of 10^{-4}. The reason for optimal performance of HQAM is the densest 2D packing of its constellation points as compared to other modulation schemes [33].

In Fig. 2.4, the ergodic capacity versus average received SNR ($\chi_\circ$) is plotted for different values of υ and C_n^2. It can be depicted that the simulation results confirm correctness of the derived analytical expression. Further, it can be seen that the channel correlation has very little impact on the channel capacity for smaller values of C_n^2. Furthermore, it is observed that increase in C_n^2 adversely affects the ergodic capacity of the system. As an example, for $\upsilon = 0$, with the increase in C_n^2 from $1 \times 10^{-16}\mathrm{m}^{-2/3}$ to $1 \times 10^{-14}\mathrm{m}^{-2/3}$, 4.5 dB more SNR is required to achieve $\mathcal{C}_e = 4$ bits/sec/Hz. This is because, C_n^2 directly affects the log-amplitude variance of the received optical signal. Also, increase in C_n^2 increases turbulence strength, thus, deteriorating the ergodic capacity of the system.

As (2.15) approximates (2.18), all analysis equations are approximations and not exact, thereby resulting in slight deviation in the simulated and analytical plots. This deviation is quantified in terms of mean square deviation error (MSDE) and

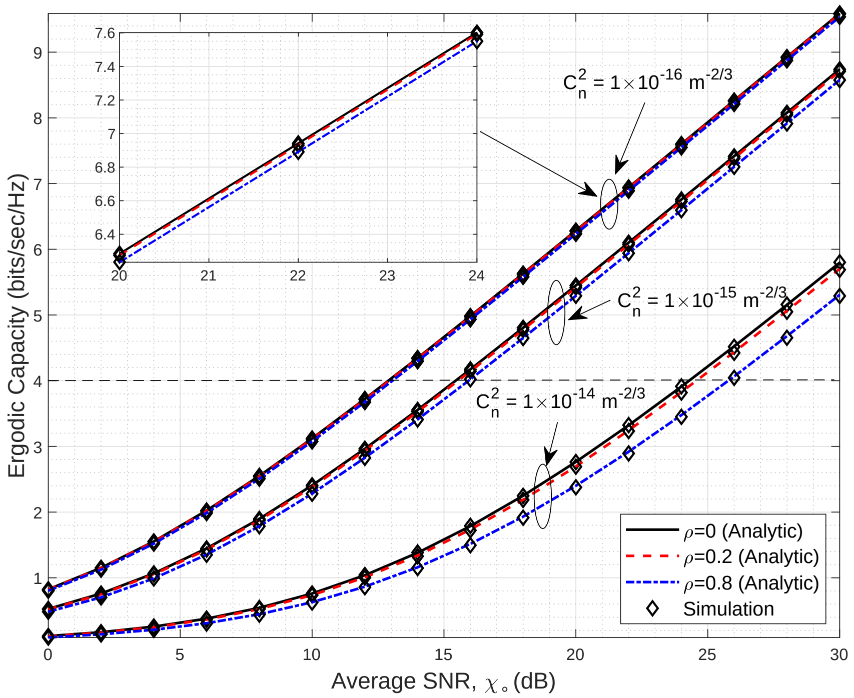

Figure 2.4: Ergodic capacity versus average SNR for different values of correlation coefficient.

the same is shown in Table 2.2, Table 2.3, Table 2.4, and Table 2.5, for the plots given in Fig. 2.2(a), Fig. 2.3(a), Fig. 2.3(b), and Fig. 2.4, respectively.

Table 2.2: MSDE in the analytical and simulated outage probability plots shown in Fig. 2.2(a).

N_r	$\rho = 0.2$	$\rho = 0.8$
2	2.4×10^{-8}	4.3×10^{-8}
3	4.3×10^{-6}	1.4×10^{-5}
4	1.1×10^{-5}	6.0×10^{-5}

Table 2.3: MSDE in the analytical and simulated ASER plots shown in Fig. 2.3(a).

Modulation Scheme	Mean Square Deviation
RQAM-16 $\times$ 2	1.1×10^{-8}
RQAM-8 $\times$ 4	1.0×10^{-8}
HQAM-32	9.7×10^{-6}
XQAM-32	2.3×10^{-5}

Table 2.4: MSDE in the analytical and simulated ASER plots shown in Fig. 2.3(b).

Modulation Scheme	Mean Square Deviation
RQAM-32 $\times$ 2	9.4×10^{-9}
RQAM-16 $\times$ 4	9.2×10^{-9}
SQAM-64	1.4×10^{-8}
HQAM-64	3.2×10^{-5}

Table 2.5: Mean square deviation in the analytical and simulated ergodic capacity plots shown in Fig. 2.4.

C_n^2	$\rho = 0$	$\rho = 0.2$	$\rho = 0.8$
1×10^{-14}	1.2×10^{-5}	1.7×10^{-6}	1.2×10^{-7}
1×10^{-15}	6.2×10^{-5}	1.7×10^{-6}	1.3×10^{-7}
1×10^{-16}	2.7×10^{-4}	0.7×10^{-5}	2.0×10^{-7}

2.7 Summary

An NLOS UVC system with multiple receiver branches and SC at the receiver is studied. The channels experienced by different receiver branches are assumed to be correlated and novel closed-form expressions are derived for the outage probability, ASER and ergodic capacity. Several simulation studies are conducted to validate the accuracy of the derived analytical expressions. The effects of receiver branches, channel correlation and elevation angles are evaluated on the system performance. It is demonstrated that for large channel correlation, increasing the number of receiver branches beyond a certain value has a very little impact on the system performance. Further, the ASER performance of different modulation schemes such as RQAM, SQAM, HQAM and XQAM is studied and it has been shown that HQAM is the optimum modulation scheme for all constellation sizes except for 4-points constellation where SQAM marginally outperforms HQAM. Additionally, it is shown that the ergodic capacity of the system improves as the channel correlation reduces. It is further been observed that for low value of refractive index structure coefficient, channel correlation has negligible impact on the ergodic capacity. This chapter addresses the problem of turbulence induced fading for NLOS UVC system. However, the considered system model does not deal with high-path loss in UVC, which exists due to strong interaction of deep UV wave with the atmospheric particles. The following chapter examines a cooperative NLOS UVC system that addresses both fading and path loss issues.

Chapter 3

Performance Analysis of AF Relayed Cooperative NLOS UVC System in the Presence of Turbulence

3.1 Introduction

In the previous chapter, spatial diversity was used to mitigate the fading effect caused by turbulence in an NLOS UVC system. Furthermore, the significance of higher-order modulation techniques in supporting a high data rate was emphasized. However, Chapter 2 did not address the issue of high path loss in UVC, which limits the communication range of a UVC link to shorter distances. There is a requirement for an NLOS UVC system that addresses both high-path loss and fading issues. This chapter examines a multi-relayed cooperative communication system that deals with the problem of high path loss by introducing relay nodes between source and destination and mitigates the effect of fading by employing multiple parallel relays. In the recent past, there have been several research studies conducted towards increasing the communication range of NLOS UVC by incorporating the cooperative communication techniques [12, 46, 66–68]. In [67], Ardakani et al. studied the BER performance of cooperative orthogonal frequency division multiplexing (OFDM) NLOS UVC; however, the authors did not consider the turbulence effect under the short distance assumption. In [46], the authors studied the performance of serially relayed multi-hop cooperative communication techniques and studied its performance for strong turbulence for which the irradiation fluctuations are modelled using gamma-gamma PDF. In [12], the authors derived a closed-form expression for the PDF of irradiance fluctuations of NLOS UVC links for weak turbulence and performed the outage analysis of DF based serially relayed multi-hop NLOS UVC system. Further, in [68], the BER performance of dual-hop AF relayed NLOS UVC system is evaluated for higher-order RQAM scheme. The multi-relay cooperative communication has also been extensively studied in the existing literature related to FSO and hybrid RF/FSO systems [54, 69–71].

In this work, an AF based multi-relay cooperative NLOS UVC system using higher-order modulation schemes, and selection combiner at the receiver is considered. The performance of the considered system is studied in terms of outage probability for both variable gain and fixed gain relaying. The diversity order of the system for variable-gain relaying as a function of system configuration parameters is derived. Further, the novel analytical expressions of ASER for higher order modulation formats including RQAM, HQAM and XQAM-32 schemes are derived. The numerical study is performed to verify correctness of the derived analytical expressions. It is shown that using parallel relays along with SC results in significant performance improvement as compared to no-relay case. It is further shown that the performance of the system further improves with an increase in number of relays, lower elevation angles, and higher FOVs.

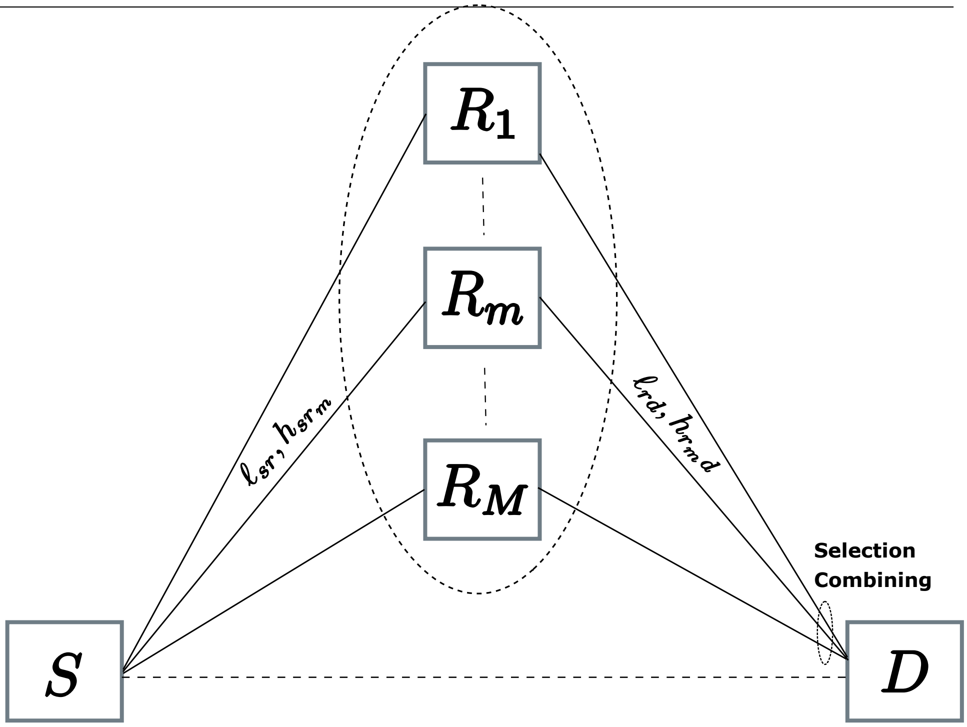

Figure 3.1: Parallel relayed NLOS UVC system.

3.2 System Model

Fig. 3.1 shows a parallel AF relayed NLOS UVC system, which consists of a source node S, a destination node D, and M relay nodes $\{R_m\}_{m=1}^{M}$. The relays are assumed to be placed in the middle such that the distance of SR_m and R_mD links are the same. All the nodes are assumed to operate in half-duplex mode. The exact CSI is assumed to be known at the receiving nodes. All the nodes are assumed to be time synchronized using decentralized algorithm [72]. Further, the total power budget is considered to be P_t, which is equally divided amongst S and $\{R_m\}_{m=1}^{M}$ nodes, such that the transmit power available at each transmitting node is $P = P_t/(M+1)$. With this system configuration, communication from S to D, via relayed path, takes place in $M+1$ time slots. In the first time slot, S transmits the information bearing signal to D and $\{R_m\}_{m=1}^{M}$ nodes. In the subsequent M time-slots, each relay node, one at a time, amplifies and forwards the received signal to D. Hence, D receives total $M+1$ copies of the signal from S and $\{R_m\}_{m=1}^{M}$. For the analytical tractability, the signal received via direct $S-D$ link is ignored at the selection combiner. This assumption has a negligible impact on the performance analysis because the direct $S-D$ link experiences very high path loss (due to long distance) as compared to the signal received via relayed link. The SC [14, 73] is used at the receiver, in which D selects the signal with maximum SNR to decode the information. A single SIM employing higher-order modulation scheme is used at Tx. In SIM, the information bearing signal is pre-modulated using an RF subcarrier. A DC bias is added to the modulated RF signal, and the resultant signal is then used to modulate the intensity of a laser diode [41, 46].

Let s be the transmitted optical signal by S in the first time-slot. The average power of s is assumed to be unity, $\mathbb{E}[|s|^2] = 1$. The signal received at the photodetector output of R_m is given as,

$$y_{r_m} = \eta P \ell_{sr} h_{sr_m} s + \nu_{r_m}, \quad m = 1 \ldots M, \tag{3.1}$$

where η is the effective optical-to-electrical conversion ratio. As the geometrical configurations are assumed to be same for all the relay nodes, therefore all the links from S to $\{R\}_{m=1}^{M}$ experience the same path loss given as ℓ_{sr}, which is normalized with the path loss of SD link. ν_r is the AWGN, $\nu_r \sim \mathcal{N}(0, \sigma_{\nu_r}^2)$ [12, 25, 46, 66, 68, 73]. $h_{sr_1} \ldots h_{sr_M}$ are the independent and identically distributed (IID) fading channel coefficients, $\ln(h_{sr_m}) \sim \mathcal{N}(\mu_{h_{sr}}, \sigma_{h_{sr}}^2)$.

In the subsequent phase, R_m amplifies the received signal by gain G and forwards the resultant signal to D. The signal received at D over $R_m D$ link is given by

$$y_m = \eta \ell_{rd} h_{r_m d} G y_{r_m} + \nu_d, \quad m = 1 \ldots M, \tag{3.2}$$

where $h_{r_1 d} \ldots h_{r_M d}$ are the IID fading coefficients, $\ln(h_{r_m d}) \sim \mathcal{N}(\mu_{h_{rd}}, \sigma_{h_{rd}})$, and $\nu_d \sim \mathcal{N}(0, \sigma_{\nu_d})^2$.

The gain (G) depends on the channel information at the relay. Both the fixed-gain relaying and variable-gain relaying are considered in the analysis depending on the CSI availability.

Fixed-gain relaying

When only the statistical information of h_{sr_m} is known, then the fixed-gain relaying is used, for which

$$G = P/\sqrt{\eta^2 P^2 \ell_{sr}^2 \mathbb{E}[h_{sr_m}^2] + \sigma_{\nu_r}^2}. \tag{3.3}$$

Using (3.1), (3.2) and (3.3), the instantaneous SNR of the SR_mD link for fixed-gain relaying is computed as

$$\chi_{sr_m d} = \frac{\chi_{sr_m}\chi_{r_m d}}{\chi_{r_m d} + C}, \tag{3.4}$$

where $C = \kappa \ell_{sr}^2 \mathbb{E}[h_{sr}^2]\chi_\circ + 1$, in which $\kappa = 1/(M+1)^2$. $\chi_{sr_m} = \kappa \ell_{sr}^2 h_{sr_m}^2 \chi_\circ$ and $\chi_{r_m d} = \kappa \ell_{rd}^2 h_{r_m d}^2 \chi_\circ$ are the instantaneous SNRs of SR_m and R_mD links, respectively. Using the properties of LN RV, it can be shown that both χ_{sr_m} and $\chi_{r_m d}$ follow LN distribution $\ln(\chi_{sr_m}) \sim \mathcal{N}(\mu_{sr}, \sigma_{sr})$ and $\ln(\chi_{r_m d}) \sim \mathcal{N}(\mu_{rd}, \sigma_{rd})$, respectively, with parameter values given by [74]

$$\mu_i = 2\mu_{h_i} + \ln\left(\kappa \ell_i^2 \chi_\circ\right) + \ln \chi_\circ, \quad \sigma_i = 4\sigma_{h_i}^2, \quad i \in \{sr, rd\}. \tag{3.5}$$

Variable-gain relaying

On the other hand, when the CSI is known at the relay, then G can be changed adaptively according to h_{sr_m}, and could be written as

$$G = P/\sqrt{\eta^2 P^2 \ell_{sr}^2 h_{sr_m}^2 + \sigma_{\nu_r}^2}. \tag{3.6}$$

Using (3.1), (3.2) and (3.6), the instantaneous SNR of the SR_mD link for variable-gain relaying can be computed as

$$\chi_{sr_m d} = \frac{\chi_{sr_m}\chi_{r_m d}}{\chi_{sr_m} + \chi_{r_m d} + 1}, \tag{3.7}$$

The SC employed at D selects the signal corresponding to the highest SNR. The resulting e2e instantaneous SNR at the output of SC is given as

$$\chi_{e2e} = \max_{m=1\ldots M} \chi_{sr_m d}. \tag{3.8}$$

3.3 Outage Probability

Using (3.8) and (1.20), the outage probability of the considered system is computed as

$$P_{out} = \prod_{m=1}^{M} F_{\chi_{sr_m d}}(\chi_{th}) = \left[F_{\chi_{sr_m d}}(\chi_{th})\right]^{M}, \tag{3.9}$$

where $F_{\chi_{sr_m d}}(\chi_{th})$ represents the CDF of $\chi_{sr_m d}$.

Fixed-gain relaying

Using (3.4), the CDF of $\chi_{sr_m d}$ is given as

$$F_{\chi_{sr_m d}}(\chi_{th}) = \Pr\left[\frac{\chi_{sr_m}\chi_{r_m d}}{\chi_{r_m d} + C} < \chi_{th}\right]. \tag{3.10}$$

On rearranging, (3.10) can alternatively be written as

$$F_{\chi_{sr_m d}}(\chi_{th}) = 1 - \Pr\left[Z \geq \frac{1}{\chi_{th}}\right], \tag{3.11}$$

where $Z = Z_1 + Z_2$, in which $Z_1 = \chi_{sr_m}^{-1}$, and $Z_2 = C\chi_{sr_m}^{-1}\chi_{r_m d}^{-1}$. Using the properties of LN RV it can be shown that both Z_1 and Z_2 follow LN distributions, $\ln(Z_i) \sim \mathcal{N}(\mu_{z_i}, \sigma_{z_i})$, $i = 1, 2$ [64]. The closed-form approximation for the distribution of sum of LN RVs is not yet known. However, according to [15, 17, 18], the sum of LN RVs can be approximated by another LN RV. Following the approach adopted in [17], Z is approximated as $\ln(Z) \sim \mathcal{N}(\mu_z, \sigma_z)$. The values of μ_z and σ_z are computed from μ_{z_i} and σ_{z_i} by following the steps given in [17]. Using the selected approximation, the

CDF of $\chi_{sr_m d}$ can be computed as $F_{\chi_{sr_m d}}(\chi_{th}) = Q\left(\frac{\ln(1/\chi_{th})-\mu_z}{\sigma_z}\right)$. On substituting $F_{\chi_{sr_m d}}(\chi_{th})$ into (3.9), the outage probability of the considered fixed-gain AF relayed system is obtained as

$$P_{out} = \left[Q\left(\frac{\ln(1/\chi_{th}) - \mu_z}{\sigma_z}\right)\right]^M. \tag{3.12}$$

Variable-gain relaying

At moderate-to-high value of $\chi_\circ$, the instantaneous SNR given in (3.7) can be approximated by

$$\tilde{\chi}_{sr_m d} = \frac{\chi_{sr_m}\chi_{r_m d}}{\chi_{sr_m} + \chi_{r_m d}}, \tag{3.13}$$

which is bounded as [34]

$$\underbrace{\frac{1}{2}\min(\chi_{sr_m}, \chi_{r_m d})}_{\chi^{lb}_{sr_m d}} \leq \tilde{\chi}_{sr_m d} \leq \underbrace{\min(\chi_{sr_m}, \chi_{r_m d})}_{\chi^{ub}_{sr_m d}}. \tag{3.14}$$

The CDF of $\chi^{ub}_{sr_m d}$ is given by [74]

$$F_{\chi^{ub}_{sr_m d}}(\chi_{th}) = 1 - \left[1 - F_{\chi_{sr_m}}(\chi_{th})\right]\left[1 - F_{\chi_{r_m d}}(\chi_{th})\right]. \tag{3.15}$$

On substituting the CDFs of LN RVs χ_{sr_m} and $\chi_{r_m d}$ into (3.15) and using the resulting expression in (3.9), the lower-bound (LB) of the outage probability for variable-gain relaying computed as

$$P^{lb}_{out} = \left[1 - Q\left(\frac{\ln(\chi_{th}) - \mu_{sr}}{\sigma_{sr}}\right) Q\left(\frac{\ln(\chi_{th}) - \mu_{rd}}{\sigma_{rd}}\right)\right]^M. \tag{3.16}$$

3.4 Diversity Gain Analysis

In this section the diversity analysis of the considered system for variable-gain relaying is computed using (1.21). The outage probability of direct SD link is given by

$$P_{out}^{sd} = 1 - Q\Big(\frac{\ln \chi_{th} - \mu_{sd}}{\sigma_{sd}}\Big), \tag{3.17}$$

with $\mu_{sd} = 2\mu_{h_{sd}} + \ln(\chi_\circ)$, $\sigma_{sd} = 4\sigma^2_{h_{sd}}$. On differentiating the logarithm of (3.16) and (3.17) with respect to $\ln \chi_\circ$, and substituting the resulting expressions into (1.21), the following RDO expression of the considered system for variable-gain relaying is obtained.

$$\text{RDO} = \frac{\sigma_{sd} M Q\Big(\frac{\ln(\chi_\circ)-\vartheta_{sd}}{\sigma_{sd}}\Big)\Big[\frac{1}{\sigma_{sr}}\exp\Big(\frac{-(\ln(\chi_\circ)-\vartheta_{sr})^2}{2\sigma^2_{sr}}\Big) + \frac{1}{\sigma_{rd}}\exp\Big(\frac{-(\ln(\chi_\circ)-\vartheta_{rd})^2}{2\sigma^2_{rd}}\Big)\Big]}{\exp\Big(\frac{-(\ln(\chi_\circ)-\vartheta_{sd})^2}{2\sigma^2_{sd}}\Big)\Big[Q\Big(\frac{\ln(\chi_\circ)-\vartheta_{sr}}{\sigma_{sr}}\Big) + Q\Big(\frac{\ln(\chi_\circ)-\vartheta_{rd}}{\sigma_{rd}}\Big)\Big]}, \tag{3.18}$$

where where $\vartheta_{sd} = \ln \chi_{th} - 2\mu_{h_{sd}}$, and $\vartheta_i = \ln \chi_{th} - 2\ln(\ell_i/(M+1)) - 2\mu_{h_i}$ for $i \in \{sr, rd\}$.

Next, the asymptotic RDO (ARDO) [47] of the system at high SNR values is computed. ARDO is defined as

$$\text{ARDO} = \lim_{\chi_\circ \to \infty} \text{RDO}. \tag{3.19}$$

Using the well known bounds of Q function [75] and evaluating the resulting expression for $\chi_\circ \to \infty$, the following approximate expression of ARDO of the considered system for variable-gain relaying is obtained.

$$\text{ARDO} \approx M\Big(\frac{\sigma^2_{sd}}{\sigma^2_{sr}} + \frac{\sigma^2_{sd}}{\sigma^2_{rd}} - \frac{\sigma^2_{sd}}{\sigma_{sr}\sigma_{rd}}\Big). \tag{3.20}$$

3.5 Average Symbol Error Rate

In this section, a variable-gain relaying is considered and the closed-form expressions of ASER for different modulation schemes including RQAM, HQAM and XQAM-32 are derived. Using the PDF based approach the LB on the ASER of the system under study can be computed as

$$P_s(e) = \int_0^\infty P_s(e|\chi) f_{\chi_{e2e}^{ub}}(\chi) d\chi. \tag{3.21}$$

Here $f_{\chi_{e2e}^{ub}}(\chi)$ is the PDF of the upper-bound (UB) of electrical SNR and can be computed by differentiating the outage probability expression given in (3.16) as

$$\begin{aligned} f_{\chi_{e2e}^{ub}}(\chi) = M &\left[f_{\chi_{sr}}(\chi) Q\left(\frac{\ln\chi - \mu_{rd}}{\sigma_{rd}} \right) + f_{\chi_{rd}}(\chi) Q\left(\frac{\ln\chi - \mu_{sr}}{\sigma_{sr}} \right) \right] \\ &\times \left[1 - Q\left(\frac{\ln\chi - \mu_{sr}}{\sigma_{sr}} \right) Q\left(\frac{\ln\chi - \mu_{rd}}{\sigma_{rd}} \right) \right]^{M-1}. \end{aligned} \tag{3.22}$$

Next, a lemma to compute averaging of a function over $f_{\chi_{e2e}^{ub}}(\chi)$ is defined.

Lemma 3.1. Let $g(\chi_{e2e}^{ub})$ is a function of the RV χ_{e2e}^{ub} whose PDF is given in (3.22), then

$$\mathbb{E}[g(\chi_{e2e}^{ub})] = \Xi_1 + \Xi_2, \tag{3.23}$$

where,

$$\begin{aligned} \Xi_1 = \frac{M}{\sqrt{\pi}} \sum_{i=1}^{N} w_i \, g\left(\sqrt{2}\,\sigma_{sr} x_i + \mu_{sr}\right) Q\left(\frac{\sqrt{2}\,\sigma_{sr} x_i + \mu_{sr} - \mu_{rd}}{\sigma_{rd}} \right) \\ \times \left[1 - Q(\sqrt{2}\,x_i) Q\left(\frac{\sqrt{2}\,\sigma_{sr} x_i + \mu_{sr} - \mu_{rd}}{\sigma_{rd}} \right) \right]^{M-1}, \end{aligned} \tag{3.24}$$

and,

$$\Xi_2 = \frac{M}{\sqrt{\pi}} \sum_{i=1}^{N} w_i \, g\Big(\sqrt{2}\,\sigma_{rd}x_i + \mu_{rd}\Big) Q\bigg(\frac{\sqrt{2}\,\sigma_{rd}x_i + \mu_{rd} - \mu_{sr}}{\sigma_{sr}}\bigg) \\ \times \left[1 - Q(\sqrt{2}\,x_i) Q\bigg(\frac{\sqrt{2}\,\sigma_{rd}x_i + \mu_{rd} - \mu_{sr}}{\sigma_{sr}}\bigg)\right]^{M-1}. \tag{3.25}$$

Here w_i and x_i, respectively, are the weight factors and zeros of the N^{th} order Hermite polynomial.

Proof. See Appendix A.1. ■

Lemma 3.1 is used to derive the ASER expressions for the higher-order modulation schemes in the following subsections.

3.5.1 Rectangular QAM Scheme

The conditional expression for the SER of $M_I \times M_Q$ RQAM over AWGN channel is given by (1.11). On substituting (1.11) into (3.21) and using Lemma 3.1, the LB of the ASER for RQAM modulation scheme is obtained as

$$P_s^{\text{RQAM}}(e) = \frac{M}{\sqrt{\pi}} \sum_{i=1}^{N} w_i \, Q\bigg(\frac{\sqrt{2}\,\sigma_{sr}x_i + \mu_{sr} - \mu_{rd}}{\sigma_{rd}}\bigg) \bigg[2p_0 Q\Big(a_0\sqrt{\sqrt{2}\,\sigma_{sr}x_i + \mu_{sr}}\Big) \\ + 2q_0 Q\Big(b_0\sqrt{\sqrt{2}\,\sigma_{sr}x_i + \mu_{sr}}\Big) - 4p_0q_0 Q\Big(a_0\sqrt{\sqrt{2}\,\sigma_{sr}x_i + \mu_{sr}}\Big) Q\Big(b_0\sqrt{\sqrt{2}\,\sigma_{sr}x_i + \mu_{sr}}\Big)\bigg] \\ \times \left[1 - Q(\sqrt{2}\,x_i) Q\bigg(\frac{\sqrt{2}\,\sigma_{sr}x_i + \mu_{sr} - \mu_{rd}}{\sigma_{rd}}\bigg)\right]^{M-1} + \frac{M}{\sqrt{\pi}} \sum_{i=1}^{N} w_i \, Q\bigg(\frac{\sqrt{2}\,\sigma_{rd}x_i + \mu_{rd} - \mu_{sr}}{\sigma_{sr}}\bigg) \\ \times \bigg[2p_0 Q\Big(a_0\sqrt{\sqrt{2}\,\sigma_{rd}x_i + \mu_{rd}}\Big) + 2q_0 Q\Big(b_0\sqrt{\sqrt{2}\,\sigma_{rd}x_i + \mu_{rd}}\Big) - 4p_0q_0 Q\Big(a_0\sqrt{\sqrt{2}\,\sigma_{rd}x_i + \mu_{rd}}\Big) \\ \times Q\Big(b_0\sqrt{\sqrt{2}\,\sigma_{rd}x_i + \mu_{rd}}\Big)\bigg] \left[1 - Q(\sqrt{2}\,x_i) Q\bigg(\frac{\sqrt{2}\,\sigma_{rd}x_i + \mu_{rd} - \mu_{sr}}{\sigma_{sr}}\bigg)\right]^{M-1}. \tag{3.26}$$

3.5.2 Hexagonal QAM Scheme

The conditional expression for the SER of HQAM over AWGN channel is given by (1.13). On substituting (1.13) into (3.21) and using Lemma 3.1, the final expression for the LB of ASER for HQAM modulation scheme is computed as

$$
\begin{aligned}
P_s^{\mathrm{HQAM}}(e) &= \frac{M}{\sqrt{\pi}} \sum_{i=1}^{N} w_i\, Q\left(\frac{\sqrt{2}\,\sigma_{sr}x_i + \mu_{sr} - \mu_{rd}}{\sigma_{rd}}\right) \Bigg[DQ\Big(\sqrt{q_1\sqrt{2}\,\sigma_{sr}x_i + \mu_{sr}}\Big) \\
&+ \frac{2}{3} D_C Q^2\Big(\sqrt{2q_1\sqrt{2}\,\sigma_{sr}x_i + \mu_{sr}/3}\Big) - 2D_C Q\Big(\sqrt{q_1\sqrt{2}\,\sigma_{sr}x_i + \mu_{sr}}\Big) Q\Big(\sqrt{q_1\sqrt{2}\,\sigma_{sr}x_i + \mu_{sr}/3}\Big)\Bigg] \\
&\times \left[1 - Q(\sqrt{2}\,x_i)Q\left(\frac{\sqrt{2}\,\sigma_{sr}x_i + \mu_{sr} - \mu_{rd}}{\sigma_{rd}}\right)\right]^{M-1} + \frac{M}{\sqrt{\pi}} \sum_{i=1}^{N} w_i\, Q\left(\frac{\sqrt{2}\,\sigma_{rd}x_i + \mu_{rd} - \mu_{sr}}{\sigma_{sr}}\right) \\
&\times \Bigg[DQ\Big(\sqrt{q_1\sqrt{2}\,\sigma_{rd}x_i + \mu_{rd}}\Big) + \frac{2}{3} D_C Q^2\Big(\sqrt{2q_1\sqrt{2}\,\sigma_{rd}x_i + \mu_{rd}/3}\Big) - 2D_C Q\Big(\sqrt{q_1\sqrt{2}\,\sigma_{rd}x_i + \mu_{rd}}\Big) \\
&\times Q\Big(\sqrt{q_1\sqrt{2}\,\sigma_{rd}x_i + \mu_{rd}/3}\Big)\Bigg] \left[1 - Q(\sqrt{2}\,x_i)Q\left(\frac{\sqrt{2}\,\sigma_{rd}x_i + \mu_{rd} - \mu_{sr}}{\sigma_{sr}}\right)\right]^{M-1}. \qquad (3.27)
\end{aligned}
$$

3.5.3 Cross QAM Scheme

The conditional expression for XQAM-32 is given by (1.12) Using (1.12), (3.21) and Lemma 3.1, the final expression for the LB of the ASER for XQAM-32 modulation scheme is computed as

$$
\begin{aligned}
P_s^{\mathrm{XQAM\text{-}32}}(e) &= \frac{M}{\sqrt{\pi}} \sum_{i=1}^{N} w_i\, Q\left(\frac{\sqrt{2}\,\sigma_{sr}x_i + \mu_{sr} - \mu_{rd}}{\sigma_{rd}}\right) \Bigg[26Q\Big(\sqrt{2A\sqrt{2}\,\sigma_{sr}x_i + \mu_{sr}}\Big) \\
&+ Q\Big(2\sqrt{A\sqrt{2}\,\sigma_{sr}x_i + \mu_{sr}}\Big) - 23Q^2\Big(\sqrt{2A\sqrt{2}\,\sigma_{sr}x_i + \mu_{sr}}\Big)\Bigg] \Bigg[1 - Q(\sqrt{2}\,x_i) \\
&\times Q\left(\frac{\sqrt{2}\,\sigma_{sr}x_i + \mu_{sr} - \mu_{rd}}{\sigma_{rd}}\right)\Bigg]^{M-1} + \frac{M}{\sqrt{\pi}} \sum_{i=1}^{N} w_i Q\left(\frac{\sqrt{2}\,\sigma_{rd}x_i + \mu_{rd} - \mu_{sr}}{\sigma_{sr}}\right) \\
&\times \Bigg[26Q\Big(\sqrt{2A\sqrt{2}\,\sigma_{rd}x_i + \mu_{rd}}\Big) + Q\Big(2\sqrt{A\sqrt{2}\,\sigma_{rd}x_i + \mu_{rd}}\Big) - 23Q^2\Big(\sqrt{2A\sqrt{2}\,\sigma_{rd}x_i + \mu_{rd}}\Big)\Bigg] \\
&\times \left[1 - Q(\sqrt{2}\,x_i)Q\left(\frac{\sqrt{2}\,\sigma_{rd}x_i + \mu_{rd} - \mu_{sr}}{\sigma_{sr}}\right)\right]^{M-1}. \qquad (3.28)
\end{aligned}
$$

3.6 Numerical and Simulation Results

In this section, the numerical results is presented for the outage probability and ASER from the derived analytical expressions and prove their correctness through Monte-Carlo simulations. Unless otherwise stated, for the presented numerical re-

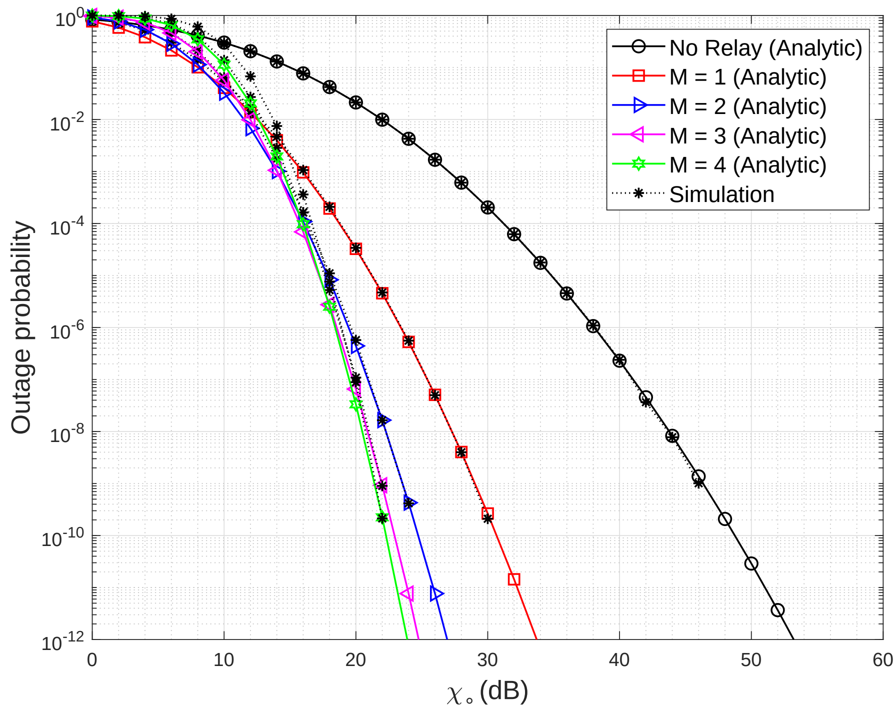

(a) For variable-gain relaying.

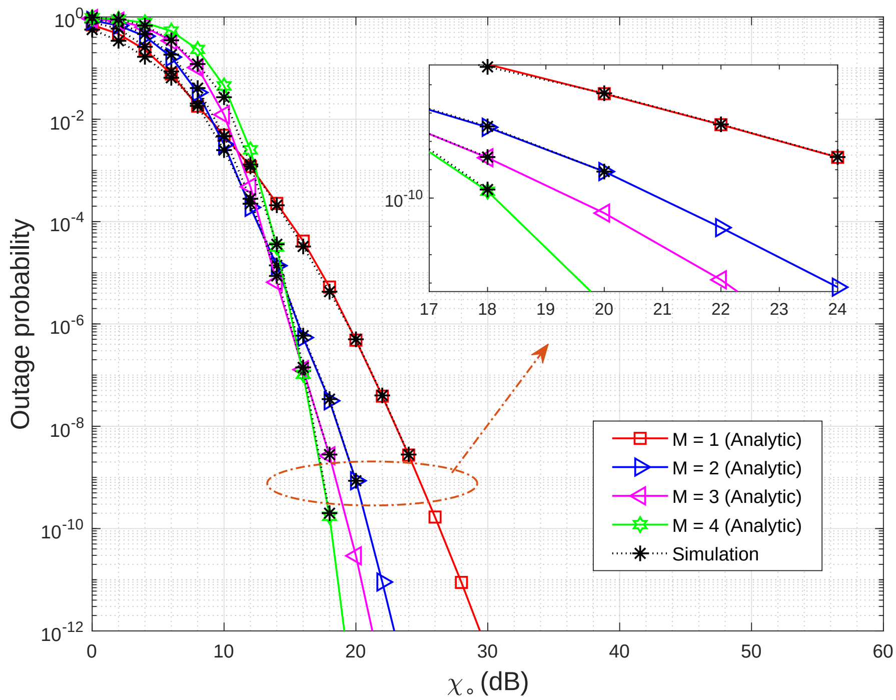

(b) For fixed-gain relaying.

Figure 3.2: Comparison of analytical and simulation results of outage probability versus SNR for different values of M.

sults, the parameter values considered are as follows: wavelength $\lambda = 260$ nm, receiver aperture area $A_r = 1.77$ cm^2, refractive index structure coefficient $C_n^2 = 5 \times 10^{-15}$ m$^{-2/3}$, Rayleigh scattering coefficient $k_s^{Ray} = 2.4 \times 10^{-4}$ m^{-1}, Mie scattering coefficient $k_s^{Mie} = 2.5 \times 10^{-4}$ m^{-1} and absorption coefficient $k_a = 9 \times 10^{-4}$ m^{-1}. The values for the channel model parameters t, f and g are considered as $0.017, 0.72$ and 0.5, respectively [10, 12]. The Tx and Rx elevation angles of S and D nodes are set as $\theta_{sd} = 30°$; and Tx and Rx elevation angle of relay node as $\theta_r = 70°$. Further, the beam divergence of S and R nodes are considered to be $\phi^{Tx} = 8$ mrad; and the FOV of the R and D nodes are configured as $\phi^{Rx} = 45°$. The total link distance between S and D nodes are considered as 1 Km. The R_m node is assumed to be placed in the middle of S and D nodes, resulting in the distance between S and R nodes; and R_m and D nodes as 500 m [12, 66, 68, 73]. In Fig. 3.2, the theoretical

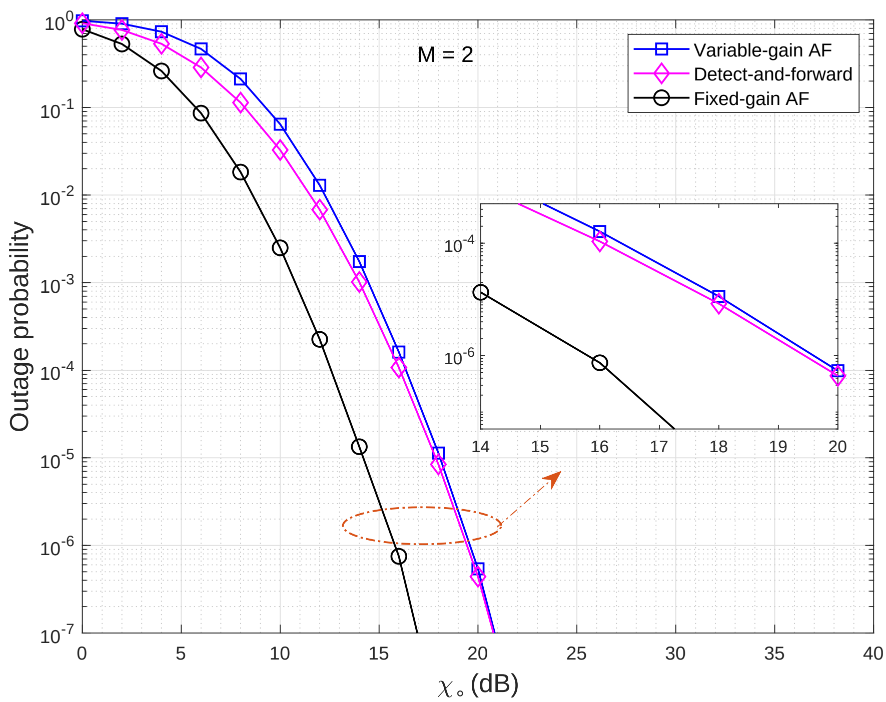

Figure 3.3: Comparison of outage probability for AF and detect-and-forward (DF).

and simulation results of the outage probability versus $\chi_\circ$ are plotted for different number of relays and $\chi_{th} = 4$ dB [25]. Fig. 3.2(a) and Fig. 3.2(b) shows the outage probability results for variable-gain and fixed-gain relaying, respectively.

It can be seen that, for moderate to high values of SNR, the numerical results

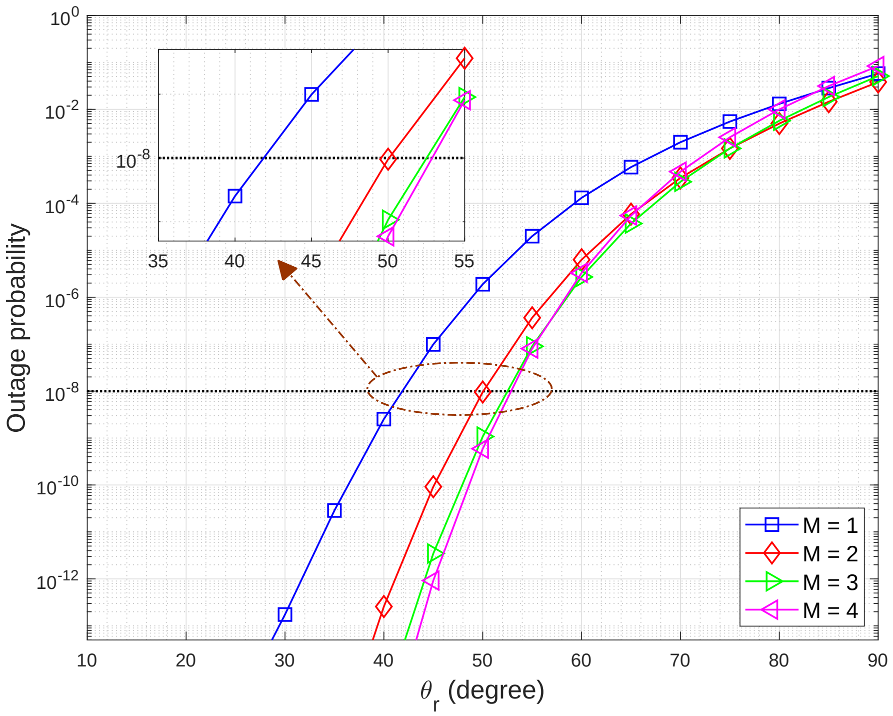

Figure 3.4: Outage probability versus relay elevation angle ($\chi_\circ = 15$ dB).

closely overlap with the theoretical results, thus confirming the accuracy of the derived analytical expression of the outage probability. It is observed that, for both fixed-gain and variable-gain cases, incorporating relays significantly improves the system performance due to reduction in the required average SNR for a given outage probability. As an example, for variable-gain relaying and target outage probability of 10^{-8}, when compared with direct SD link, an SNR gain of 16.5 dB, 21.5 dB, 22.75 dB and 23.25 dB is obtained for $M = 1, 2, 3$ and 4, respectively. Further, it is observed that for a given SNR, the outage probability of fixed-gain relaying is lower than that of the variable-gain case. This is because of the high amplification gain of fixed-gain relaying, irrespective of the channel conditions. On the other hand, the amplification gain in the case of variable-gain is comparatively less due to its dependence on the CSI [70].

Fig. 3.3 compares the simulation results for variable-gain AF, fixed-gain AF, and DF relaying. It can be seen that fixed-gain AF outperforms both DF and variable-gain AF with an SNR gain of 3.51 dB and 3.75 dB, respectively, for 10^{-4}

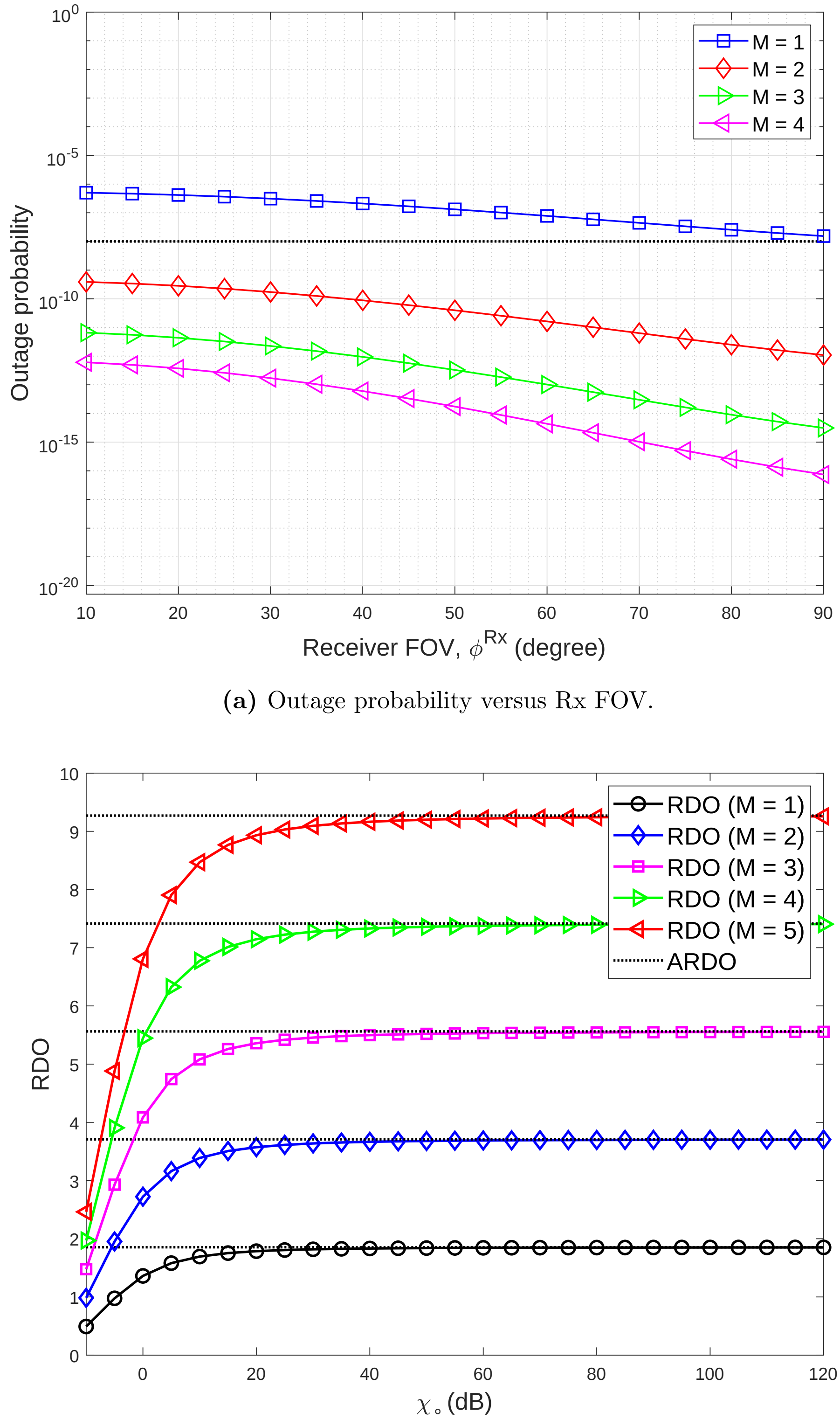

(a) Outage probability versus Rx FOV.

(b) RDO versus $\chi_\circ$ for different M values.

Figure 3.5: Theoretical results of outage probability and RDO for variable-gain relaying.

outage probability. It is observed that DF performs better than the variable-gain AF for lower values of SNR, however, as the SNR increases, outage curves for DF

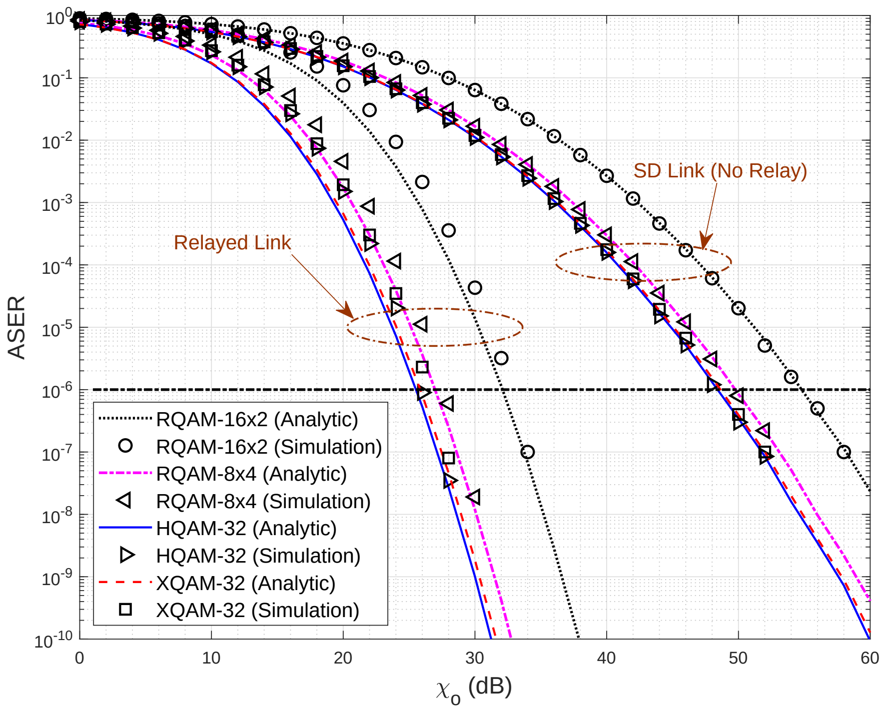

(a) 32-points constellations.

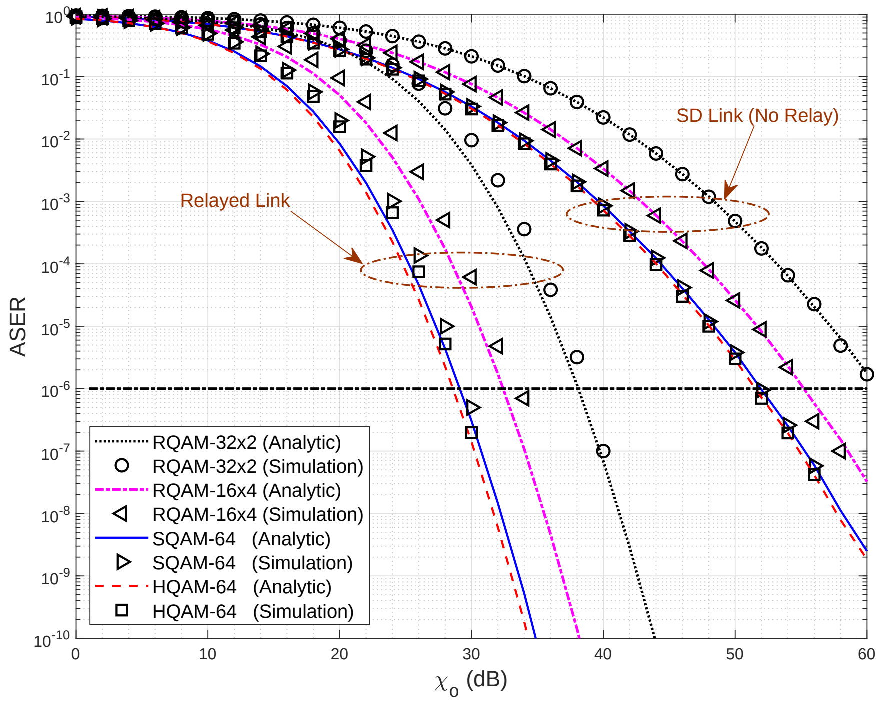

(b) 64-points constellations.

Figure 3.6: Comparison of analytical and simulation results of ASER versus SNR for variable-gain relaying and different modulation schemes.

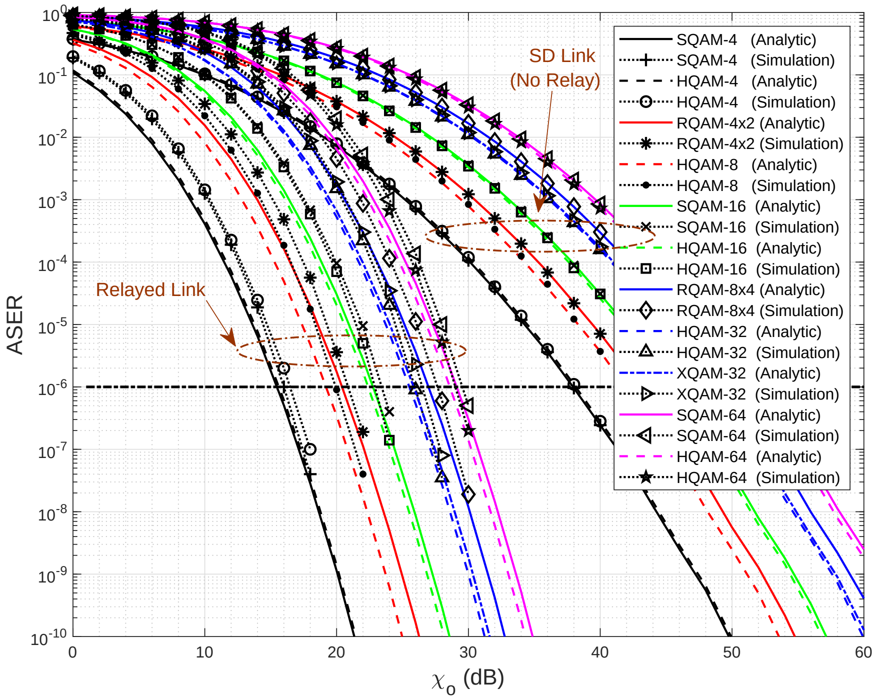

(c) 4, 8, 16, 32, 64-points constellations.

Figure 3.6: Comparison of analytical and simulation results of ASER versus SNR for variable-gain relaying and different modulation schemes (contd.).

and variable-gain AF start overlapping. This is because, outage probability of DF is same as that of outage probability of LB for variable-gain AF, and the LB becomes tight for higher SNR values.

Fig. 3.4 presents theoretical plots to show the effect of relay elevation angle (θ^r) on the system outage probability for different M. It can be seen that the outage probability reduces as the relay elevation angle decreases. This behavior is due to the fact that as the relay angle decreases, the relative distance between the Tx and Rx with CV decreases, thereby reducing the effective path loss and improvement in the system performance.

Fig. 3.5(a) studies the impact of receiver FOV on the system outage probability. It can be seen that the system performs better for higher values of FOV. The reason for this improvement is that for large FOV, more number of photons are received by the Rx, which in turn participates in the detection process, thus resulting in enhanced system performance. Using the higher value of FOV is practically possible as the UV-C band is solar blind and results in negligible noise at the Rx. Fig. 3.5(b) depicts the RDO of the system for different number of relays. It is observed that RDO converges to ARDO at higher SNR values confirming the accuracy of the derived analytical results in Section 3.4. Further, it is observed that the diversity order improves with the increase of number of relays. For example, the diversity order of $1.85, 3.71, 5.51$, and 7.42 are achieved for $M = 1, 2, 3$, and 4, respectively.

In Fig. 3.6, the numerical and simulation curves of ASER are plotted for different modulation formats and constellation sizes, considering $M = 2$ and $\theta^r = 50°$. It can be seen that irrespective of the modulation format used, relayed links always provide significant performance gains as compared to no-relay case. Further, the simulation curves closely follow the theoretical ASER and nearly starts overlapping for moderate to higher values of average SNR.

Fig. 3.6(a) presents the ASER vs. $\chi_\circ$ curves for 32-points RQAM, HQAM and XQAM schemes for a target ASER of 10^{-6}. It can be seen that XQAM-32 outperforms RQAM-16×2 and RQAM-8×4 scheme with a significant gain of ~ 6 dB and ~ 5 dB, respectively. The reason for better performance of XQAM-32 is due its lower peak and average power as compared with RQAM. Further, it can be seen that on using HQAM-32, an additional gain of 0.5 dB is achieved as compared to XQAM-32.

In Fig. 3.6(b), the ASER performance curves for RQAM-32×2, RQAM-16×4, SQAM-64 and HQAM-64 schemes are presented. It can be seen that for the target ASER of 10^{-6}, HQAM-64 performs better than SQAM-64, RQAM-32×2 and RQAM-16×4 schemes by providing a significant SNR gains of 0.5 dB, 4 dB and 9.5 dB, respectively. Further, using SQAM-64 results in the significant gain of ~ 4.5 dB and ~ 9 dB as compared to RQAM-16×4 and RQAM-32×2 schemes, respectively. The SQAM outperforms non-square RQAM by maximizing the minimum distance between the constellation points for a given energy. As a result, SQAM requires less power as compared to non-square RQAM for the target ASER.

In Fig. 3.6(c) ASER curves of different modulation formats are compared for the constellation sizes of $4, 16, 32, 64$. It is observed that for $4, 16$, and 64 points constellation, SQAM always outperforms the non-square RQAM in terms of required average SER. Further, it can be seen that, except for the 4-points constellation size, HQAM always performs optimally, as compared to other modulation formats. For instance, to achieve an ASER of 10^{-6}, HQAM-8, HQAM-16, HQAM-32, and HQAM-64 results in the SNR gain of approx. 1.5 dB, 0.5 dB, 1.5 dB and 0.5 dB as compared to RQAM-4×2, SQAM-16, RQAM-8×4 and SQAM-64, respectively. The HQAM optimum performance is attributed to the densest packing of its 2D constellation points as compared to other modulation formats [33].

3.7 Summary

In this work, a parallel AF relayed NLOS UVC system with SC employed at the destination node is considered. Performance of the system is analyzed by deriving the closed-form analytical expressions for the outage probability, RDO, ARDO, and ASER. The outage performance for the fixed-gain and variable-gain relaying cases is studied. It is shown that the fixed-gain relaying outperforms the variable-gain relaying irrespective of the number of relays. A detailed study of the considered system is studied for higher-order modulation scheme for a wide variety of system parameters. It is shown that large performance gains can be achieved by using parallel relays, however, increasing the number of relays beyond a certain value has a very limited impact on the system performance. Further, it is shown that the system performs optimally well for lower elevation angles and higher Rx FOV. Furthermore, it is observed that HQAM results in significant performance gains as compared to RQAM and XQAM schemes for the considered UVC system. This chapter investigates the parallel relayed cooperative communication system, which requires $M + 1$ slots to carry out one e2e communication. The channel coefficients are also assumed to be perfectly known at the receiver. In the following chapter, a cooperative communication system based on best relay selection is presented, which requires only two time slots regardless of the number of relays used. The impact of CSI imperfection on system performance is also assessed.

Chapter 4

Impact of CSI Imperfections on Multiple Relay DF NLOS UVC Systems

4.1 Introduction

In the previous chapter, an NLOS UVC cooperative communication system involving AF based parallel relays was presented. Even though, the parallel relayed cooperative system effectively addresses the problem of high path loss and fading in the UV channel. However, due to the greater time duration required to achieve a single e2e communication, it has a limited system capacity. Additionally, the receiver's CSI is supposed to be exactly known, which is not realistic in a practical system. This chapter describes an NLOS UVC cooperative communication system that utilizes best-relay selection. This solution takes into account the practical issue of imperfect CSI knowledge at the receiver and also offers data-rate improvement by shortening the time required for single e2e communication.

Although, the relay-assisted NLOS UVC cooperative system has piqued the interest of researchers. The use of best relay selection in conjunction with imperfect CSI remains unexplored in the UVC literature. In [12], Ardakani et al. studied the performance of a serial relayed NLOS UVC system considering binary PPM (BPPM) and weak atmospheric turbulence modeled using LN distribution. Authors computed the outage probability and diversity order assuming perfect knowledge of the CSI at the Rx nodes. In [67], Ardakani et al. proposed a three-node dual-hop cooperative NLOS UVC system ignoring the effect of atmospheric turbulence under the assumption of short-distance link. A frequency selective UVC channel is considered, and DC-biased optical OFDM (DCO-OFDM) scheme is used to mitigate the inter-symbol interference (ISI). Authors studied the BER performance of DCO-OFDM in the absence of fading and optimized the source and relay node's power allocation. Further, the system throughput is maximized using bit loading. In [25], Arya et al. considered strong turbulence scenarios and derived outage probability of a system with multiple correlated Rx branches. In [66], the performance of a multi-relay NLOS UVC system is studied in terms of outage probability assuming the perfect knowledge of CSI. Further, the important performance metrics such as diversity order and ASER are not computed in this work. In [73], authors conducted a detailed performance study of SIMO NLOS UVC system under weak turbulence scenarios. Further, the authors derived outage probability, ASER for higher-order QAM schemes. The performance of a multihop AF relayed NLOS UVC system is studied in [46] considering the SIM scheme. In [76], authors considered a parallel dual-hop AF-relayed NLOS UVC system, and evaluated the LB on the outage probability and ASER for higher order modulation schemes. In all these studies, the CSI is assumed to be perfectly known at the Rx, which is impossible to achieve in practical systems [77, 78]. In [79], a dual-hop DF based single-relayed NLOS UVC system is considered with multiple receiver branches at the destination node only. SC is employed at the destination node and ASER performance of the system is evaluated only for RQAM scheme. There has been several studies conducted in the past, in which researchers evaluated the impact of imperfect CSI on the performance of RF cooperative communication systems [24, 34, 35]. In [34], authors evaluated the performance of a dual-hop variable-gain AF relayed RF communication system for Nakagami-m fading channel and studied the impact of imperfect CSI on the ASER performance of the system for a variety of higher order QAM schemes. In [24], a multi-relay RF communication system with best relay selection is considered with imperfect CSI at the Rx. The ASER performance of the system is analyzed for higher order modulation schemes including RQAM, HQAM, and XQAM over Nakagami-m fading links. In [35], the performance of a MIMO non-regenerative RF cooperative network with transmit antenna selection (TAS) and MRC employed at the Tx and Rx, respectively, is studied. The authors analyzed the impact of imperfect CSI on the ASER performance of the considered system. In addition, most communication receivers estimate CSI at the Rx for symbol detection. Thus, for practical applicability of UVC operating on futuristic higher-order modulation schemes, it is important to study the impact of CEEs on its performance. Main contributions of this work are as follows:

1. For the first time in multi-relay NLOS UVC studies, the practical case of imperfect CSI at the Rx is considered and its impact on the performance of the considered multi-relay system is evaluated.

2. A DF based cooperative NLOS UVC system employing relay selection is presented and its performance in terms of outage probability is analyzed. Further, the novel PDF expression of e2e SNR of the considered system is derived. Furthermore, the ASER analysis is conducted for higher-order modulation schemes, such as RQAM, HQAM and XQAM, by deriving the closed-form expressions using PDF based approach.

3. The diversity analysis of the system is performed and novel expressions of the RDO and ARDO are computed. The reason for computing RDO is due to the non-convergent nature of the conventional diversity order for LN faded UVC channels. To overcome this difficulty, the RDO is computed as an alternative performance metric in the literature. The RDO and ARDO expressions are derived by considering non-relay NLOS UVC link as the benchmark scheme

and provide comprehensive analysis. The impact of varying number of relays and system configurations on the achieved diversity gains is demonstrated.

4. Although there has been considerable research in RF cooperative communication systems. However, the underlying analysis, analytical results, and inferences are not applicable to NLOS UVC system due to its entirely different channel characteristics and system configurations. The system limiting factors such as turbulence severity, elevation angles, and Rx FOV are not considered in RF, FSO, and VLC communication systems. Therefore, the results presented in this study are useful to gain insights about multi-relay NLOS UVC performance and its dependence on various configuration parameters.

As both the current chapter and Chapter 3 involve multiple parallel relays, it is worth mentioning how the system model of the current chapter differs from the one considered in Chapter 3. There are three major differences, as stated below:

1. In the current chapter, a best relay selection scheme is employed in which there is only one active link from the best relay to the destination node. However, in the parallel cooperative relaying setup considered in Chapter 3, there exist M active links from relays to the destination nodes. Due to this difference, in best relay selection, two time slots are needed to realise one full e2e communication. However, in parallel relaying of chapter 3, $M+1$ time slots are needed for one communication, which is way higher than that of best relay selection.

2. The second difference is in the cooperative protocol. In Chapter 3, AF cooperative relaying is used, considering both the fixed-relaying and variable-gain relaying scenarios. However, in the current chapter, a DF cooperative relaying protocol is used.

3. The third significant difference is with regard to the availability of CSI. In Chapter 3, the CSI is assumed to be perfectly known at Rx. However, in the current chapter, the practical case of imperfect CSI is considered and its impact on the system performance is studied.

4.2 System Model

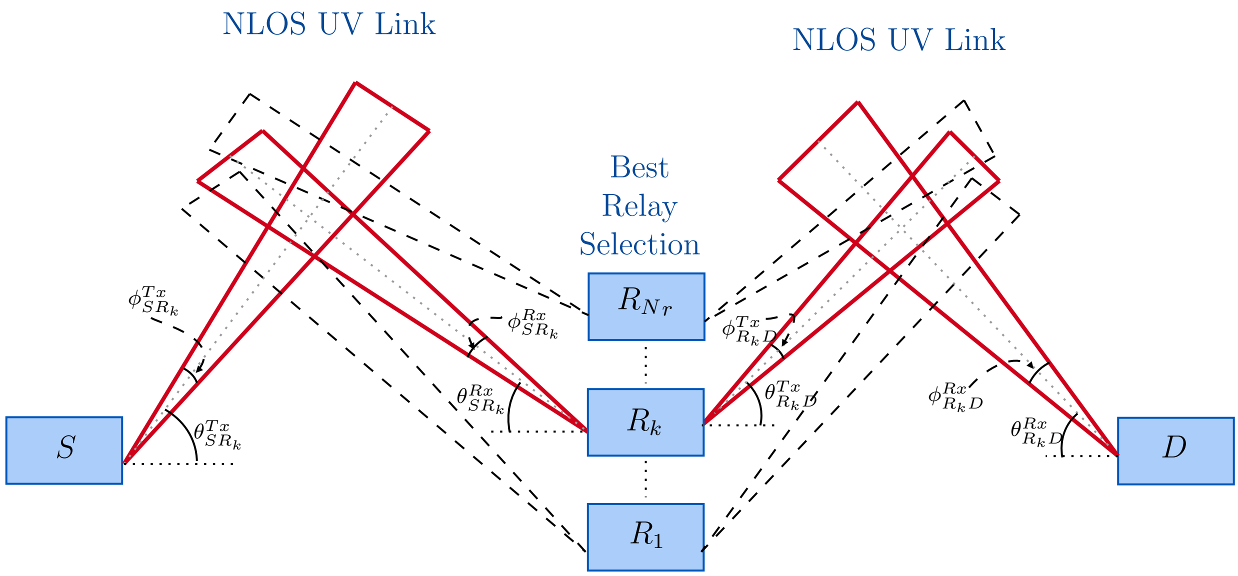

Figure 4.1: A multi-relay NLOS UVC system with best relay selection.

In this work, a dual-hop planar NLOS UVC system is considered which has a source (S), a destination (D) and N_r parallel relays R_k, $k = 1 \ldots N_r$ as shown in Fig. 4.1. All the nodes are assumed to operate in half-duplex mode. The channel coefficients corresponding to SR_k and R_kD links are independent and follow LN distribution for weak turbulence case. The relays are configured with the same elevation angles and FOVs, resulting in identical distribution of h_{SR_k} links,

$$\ln(h_{SR_k}) \sim \mathcal{N}(\mu_{h_{SR_k}}, \sigma^2_{h_{SR_k}}), \tag{4.1}$$

with $\mu_{h_{SR_k}} = \mu_{h_{SR}}$ and $\sigma^2_{h_{SR_k}} = \sigma^2_{h_{SR}}$, $\quad k = 1 \ldots N_r$; and identical distribution of h_{R_kD} links,

$$\ln(h_{R_kD}) \sim \mathcal{N}(\mu_{h_{R_kD}}, \sigma^2_{h_{R_kD}}) \tag{4.2}$$

with $\mu_{h_{R_kD}} = \mu_{h_{RD}}$ and $\sigma^2_{h_{R_kD}} = \sigma^2_{h_{RD}}$, $\quad k = 1 \ldots N_r$. Further, with similar system configurations the path loss of SR_k and R_kD links are given as $\ell_{SR_k} = \ell_{SR}$ and $\ell_{R_kD} = \ell_{RD}$, respectively. To avoid the adaptive threshold requirement of

OOK modulation and to achieve higher spectral efficiency, SIM is used at Tx.

At the UVC Rx, the CSI is not known a priori, and is thus estimated prior to the symbol detection. Considering MMSE at the Rx, the actual channel (h_m) and its estimate ($\hat{h}_m$) are related as $h_m = \hat{h}_m + e_m$, where $e_m \sim \mathcal{N}(0, \sigma_{e,m}^2)$ is the CEE with $\sigma_{e,m}^2 = \frac{v_{h_m}}{1+\rho \ell_m^2 \chi_\circ v_{h_m}}$, $m \in \{SR_k, R_kD\}$ [24, 34, 35, 74]. $v_{h_m} = [\exp(\sigma_{h_m}^2) - 1]\exp(2\mu_{h_m} + \sigma_{h_m}^2)$ is the variance of h_m, $\rho > 0$ represents quality of the channel estimate, and $\chi_\circ$ is the average received SNR of the non-relayed link.

The instantaneous electrical SNR of the SR_kD link at Rx is given as

$$\chi_{DF}^{(k)} = \min(\chi_{SR_k}, \chi_{R_kD}), \tag{4.3}$$

where $\chi_m = \frac{\ell_m^2 \iota_{eo}^2 \iota_{oe}^2 \chi_\circ \hat{h}_m^2}{4(1+\ell_m^2 \sigma_{e,m}^2 \chi_\circ)}$, $m \in \{SR_k, R_kD\}$ represents the instantaneous SNR of the m^{th} link in which i_{eo} is the optical to electrical conversion efficiency of the PD. For moderate to high SNRs, $\sigma_{e,m}^2$ is very small as compared to v_{h_m}, and hence, the distribution of h_m and $\hat{h}_m$ is considered as approximately same with negligible impact on the performance analysis [34, 59]. Using the properties of LN RVs, it can be shown that χ_m also follows LN distribution as

$$\ln(\chi_m) \sim \mathcal{N}\big(2\mu_{h_m} - \ln\big(4\epsilon_m + 4\sigma_{e,m}^2\big), 2\sigma_{h_m}\big), \tag{4.4}$$

where $\epsilon_m = \ell_m^{-2}\chi_\circ^{-1}$. The best-relay selection technique is used, in which the relay with the highest SNR is chosen for communication to D [33]. Due to relatively high path loss of SD link ($\sim$ 123 dB for 1 Km distance [10]) as compared to SR_kD link, the SNR of the SD link is not considered by the selection combiner at D for UVC cases. Thus, the instantaneous e2e electrical SNR at node D is given by

$$\chi_{e2e} = \max_{k=1\ldots N_r} \chi_{DF}^{(k)} \,. \tag{4.5}$$

In the next section, the e2e SNR (χ_{e2e}) is used to compute outage probability of the considered system.

4.3 Outage Probability

The outage probability of SR_kD link is computed as

$$P_{out}^{SR_kD} = \Pr[\chi_{DF}^{(k)} \leq \chi_{th}] = F_{\chi_{DF}^{(k)}}(\chi_{th}), \tag{4.6}$$

where $F_{\chi_{DF}^{(k)}}(\chi_{th})$ is recognized as the CDF of $\chi_{DF}^{(k)}$. Substituting (4.3) into (4.6) and rearranging results in

$$F_{\chi_{DF}^{(k)}} = 1 - \Pr[\min(\chi_{SR_k}, \chi_{R_kD}) \geq \chi_{th}]. \tag{4.7}$$

For independent RVs χ_{SR_k} and χ_{R_kD}, (4.7) can alternatively be represented as [12]

$$F_{\chi_{DF}^{(k)}} = 1 - [1 - F_{\chi_{SR_k}}(\chi_{th})][1 - F_{\chi_{SR_k}}(\chi_{th})], \tag{4.8}$$

where $F_{\chi_{SR_k}}(\cdot)$ and $F_{\chi_{R_kD}}(\cdot)$ represent CDFs of RVs χ_{SR_k} and χ_{R_kD}, respectively. For independent RVs $\chi_{DF}^{(1)}, \chi_{DF}^{(2)}, \ldots \chi_{DF}^{(N_r)}$, the outage probability of the e2e system can be computed from (4.5) and (4.8) as [80]

$$P_{out}^{e2e} = \prod_{k=1}^{N_r} \Big(1 - \big[1 - F_{\chi_{SR_k}}(\chi_{th})\big]\big[1 - F_{\chi_{R_kD}}(\chi_{th})\big]\Big). \tag{4.9}$$

On substituting the CDFs of identically distributed LN RVs $\{\chi_{SR_k}\}_{k=1}^{N_r}$ and $\{\chi_{R_kD}\}_{k=1}^{N_r}$ into (4.9), the following closed expression of the outage probability for the considered system is obtained. [1]

$$\begin{aligned} P_{out}^{e2e} = \Bigg[1 - Q\Bigg(\frac{\ln(\chi) - 2\mu_{h_{SR}} + \ln\big(4\epsilon_{SR} + 4\sigma_{e,SR}^2\big)}{2\sigma_{h_{SR}}}\Bigg) \\ \times Q\Bigg(\frac{\ln(\chi) - 2\mu_{h_{RD}} + \ln\big(4\epsilon_{RD} + 4\sigma_{e,RD}^2\big)}{2\sigma_{h_{RD}}}\Bigg)\Bigg]^{N_r}. \end{aligned} \tag{4.10}$$

[1] Using (4.1) and (4.2), $\sigma_{e,SR} = \sigma_{e,SR_k}, \epsilon_{SR} = \epsilon_{SR_k}, \sigma_{e,RD} = \sigma_{e,R_kD}$, and $\epsilon_{RD} = \epsilon_{R_kD}$ for $k = 1 \ldots N_r$.

Note that, for notational simplicity, the symbol χ_{th} is replaced with χ in (4.10). Further, observing P_{out}^{e2e} as the CDF of χ_{e2e}, (4.10) is differentiated with respect to χ to obtain the PDF for χ_{e2e} as

$$\begin{aligned}
&f_{\chi_{e2e}}(\chi) = \\
&N_r\left[f_{\chi_{SR}}(\chi)Q\left(\frac{\ln(\chi)-2\mu_{h_{RD}}+\ln\left(4\epsilon_{RD}+4\sigma_{e,RD}^2\right)}{2\sigma_{h_{RD}}}\right)\right.\\
&\left.+f_{\chi_{RD}}(\chi)Q\left(\frac{\ln(\chi)-2\mu_{h_{SR}}+\ln\left(4\epsilon_{SR}+4\sigma_{e,SR}^2\right)}{2\sigma_{h_{SR}}}\right)\right]\\
&\times\left[1-Q\left(\frac{\ln(\chi)-2\mu_{h_{SR}}+\ln\left(4\epsilon_{SR}+4\sigma_{e,SR}^2\right)}{2\sigma_{h_{SR}}}\right)Q\left(\frac{\ln(\chi)-2\mu_{h_{RD}}+\ln\left(4\epsilon_{RD}+4\sigma_{e,RD}^2\right)}{2\sigma_{h_{RD}}}\right)\right]^{N_r-1},
\end{aligned} \tag{4.11}$$

where $f_{\chi_j}(\chi)=\frac{1}{\sqrt{2\pi}\,2\sigma_{h_j}}\exp\left[\frac{-\left(\ln(\chi)-2\mu_{h_j}+\ln\left(4\epsilon_j+4\sigma_{e,j}^2\right)\right)^2}{8\sigma_{h_j}^2}\right]$, $j\in\{SR,RD\}$. The $f_{\chi_{e2e}}(\chi)$ is used in deriving analytical expressions of ASER in later sections. Therefore, Theorem-4.1 is defined which compute ensemble average of an arbitrary function of χ_{e2e} using the PDF derived in (4.11).

Theorem 4.1. Let $g(\cdot)$ be an arbitrary function of RV χ_{e2e}, whose PDF is given in (4.11). The ensemble average of $g(\chi_{e2e})$ can be computed as

$$\begin{aligned}
&\mathbb{E}[g(\chi_{e2e})]=\int_0^\infty g(\chi)f_{\chi_{e2e}}(\chi)d\chi=\frac{N_r}{\sqrt{\pi}}\sum_{n=1}^{N}w_n g\left(\exp\left(\kappa_n^{SR}-\ln\left(4\epsilon_{SR}+4\sigma_{e,SR}^2\right)\right)\right)\\
&\times Q\left(\Delta_{RD}\kappa_n^{SR}-\Upsilon_{RD}-\Delta_{RD}\ln(\vartheta)\right)\left[1-Q\left(\sqrt{2}\xi_n\right)Q\left(\Delta_{RD}\kappa_n^{SR}-\Upsilon_{RD}-\Delta_{RD}\ln(\vartheta)\right)\right]^{N_r-1}\\
&+\frac{N_r}{\sqrt{\pi}}\sum_{n=1}^{N}w_n g\left(\exp\left(\kappa_n^{RD}-\ln\left(4\epsilon_{RD}+4\sigma_{e,RD}^2\right)\right)\right)Q\left(\Delta_{SR}\kappa_n^{RD}-\Upsilon_{SR}+\Delta_{SR}\ln(\vartheta)\right)\\
&\times\left[1-Q\left(\sqrt{2}\xi_n\right)Q\left(\Delta_{SR}\kappa_n^{RD}-\Upsilon_{SR}+\Delta_{SR}\ln(\vartheta)\right)\right]^{N_r-1},
\end{aligned} \tag{4.12}$$

where $\kappa_n^j=2\sqrt{2}\,\sigma_{h_j}\xi_n+2\mu_{h_j}$, $\Delta_j=1/2\sigma_{h_j}$, $\Upsilon_j=\mu_{h_j}/\sigma_{h_j}$ with $j\in\{SR,RD\}$, and $\vartheta=\left(\epsilon_{SR}+\sigma_{e,SR}^2\right)/\left(\epsilon_{RD}+\sigma_{e,RD}^2\right)$. w_n and ξ_n are the weights and zeros of N^{th} order Hermite polynomial, respectively.

Proof. See Appendix B.1. ■

4.4 Diversity Analysis

4.4.1 Relative Diversity Order (RDO)

For systems incorporating multiple relays, non-relayed (SD link) is typically considered as the benchmark scheme [12]. With this consideration, the RDO of the system is defined as,

$$\text{RDO} = \frac{\partial \ln P_{out}^{e2e} / \partial \ln \chi_\circ}{\partial \ln P_{out}^{SD} / \partial \ln \chi_\circ}, \tag{4.13}$$

where

$$P_{out}^{SD} = 1 - Q\Big(\frac{\ln(\chi) - 2\mu_{h_{SD}} + \ln\big(4\epsilon_{SD} + 4\sigma_{e,SD}^2\big)}{2\sigma_{h_{SD}}}\Big) \tag{4.14}$$

is the outage probability of the SD link.

Theorem 4.2. The RDO of the considered system is computed as

$$\begin{aligned}\text{RDO} = {} & \frac{2\sigma_{h_{SD}} N_r Q\left(\frac{\ln(\chi_\circ)-\ln(\zeta_{SD})+2\mu_{h_{SD}}}{2\sigma_{h_{SD}}}\right)}{\exp\left(\frac{-\left(\ln(\chi_\circ)-\ln(\zeta_{SD})+2\mu_{h_{SD}}\right)^2}{8\sigma_{h_{SD}}^2}\right)} \Bigg[\frac{\frac{1}{2\sigma_{h_{SR}}}\exp\left(\frac{-\left(\ln(\chi_\circ)-\ln(\zeta_{SR})+2\mu_{h_{SR}}\right)^2}{8\sigma_{h_{SR}}^2}\right)}{Q\left(\frac{\ln(\chi_\circ)-\ln(\zeta_{SR})+2\mu_{h_{SR}}}{2\sigma_{h_{SR}}}\right)+Q\left(\frac{\ln(\chi_\circ)-\ln(\zeta_{RD})+2\mu_{h_{RD}}}{2\sigma_{h_{RD}}}\right)} \\ & + \frac{\frac{1}{2\sigma_{h_{RD}}}\exp\left(\frac{-\left(\ln(\chi_\circ)-\ln(\zeta_{RD})+2\mu_{h_{RD}}\right)^2}{8\sigma_{h_{RD}}^2}\right)}{Q\left(\frac{\ln(\chi_\circ)-\ln(\zeta_{SR})+2\mu_{h_{SR}}}{2\sigma_{h_{SR}}}\right)+Q\left(\frac{\ln(\chi_\circ)-\ln(\zeta_{RD})+2\mu_{h_{RD}}}{2\sigma_{h_{RD}}}\right)}\Bigg],\end{aligned} \tag{4.15}$$

where $\zeta_p = 4\ell_p^{-2}\chi^{-1}, p \in \{SD, SR, RD\}$ with χ is the threshold SNR.

Proof. See Appendix B.2. ■

The RDO expression of (4.15) is quite complex and does not explicitly state about the obtained diversity order and its dependence on the system configuration.

To gain further insights on the achieved diversity gain, the asymptotic value of the RDO is computed at high SNR values below.

4.4.2 Asymptotic RDO (ARDO)

The ARDO is computed as higher SNR approximation of RDO as [47]

$$\mathrm{ARDO} = \lim_{\chi_\circ \to \infty} \mathrm{RDO}. \tag{4.16}$$

Theorem 4.3. The ARDO of considered system is given as

$$\mathrm{ARDO} \approx N_r \sigma_{h_{SD}}^2 \left[\left(\sigma_{h_{SR}}^{-1} - \sigma_{h_{RD}}^{-1} \right)^2 + \sigma_{h_{SR}}^{-1} \sigma_{h_{RD}}^{-1} \right]. \tag{4.17}$$

Proof. See Appendix B.3. ∎

Corollary 4.1. For the special case of same elevation angles at S, R, and D; and $d_{SR} = d_{RD} = d_{SD}/2$, the ARDO expression converges to $N_r 2^{11/6}$. ∎

It is noteworthy to see that, due to its simplicity, ARDO gives more insight about the achieved diversity order as compared to RDO derived in the previous section. ARDO expression clearly shows dependence of the diversity order on the number of relays, and scintillation indexes of SR_k, R_kD and SD links. It can be inferred that for a fixed $\sigma_{h_{SD}}^2$, relative diversity order of the system is directly proportional to N_r, however, the presence of additional term $\left(\sigma_{h_{SR}}^{-1} - \sigma_{h_{RD}}^{-1} \right)^2 + \sigma_{h_{SR}}^{-1} \sigma_{h_{RD}}^{-1}$ lowers the diversity order of system for high turbulence scenarios. The same is expected because due to high turbulence, the optical wave front distortion becomes more prominent, thereby resulting in increased molecular dispersion, and deteriorated system performance [81]. Further, from Corollary 4.1, it can be observed that the dependence of the diversity order on scintillation index vanishes when identical configurations are chosen for SR_k, R_kD and SD links.

4.5 ASER analysis

In this section, the ASER analysis of the considered system is presented for a variety of different modulation schemes including RQAM, HQAM and XQAM-32. Using the PDF based approach, the ASER expression of the system can be computed as [73]

$$P_s(e) = \int_0^{\infty} P_s(e|\chi) f_{\chi_{e2e}}(\chi) d\chi, \tag{4.18}$$

where $P_s(e|\chi)$ is the conditional SER for the AWGN channel, and $f_{\chi_{e2e}}(\chi)$ is the PDF of the e2e SNR of the system given by (4.11).

4.5.1 Rectangular QAM Scheme

The conditional SER expression of RQAM-$M_I \times M_Q$ scheme is given in (1.11). On substituting the (1.11) into (4.18) and applying Theorem-4.1, the ASER expression of the RQAM scheme is obtained as

$$\begin{aligned}
P_s^{\mathrm{RQAM}}(e) &= \frac{N_r}{\sqrt{\pi}} \sum_{n=1}^{N} w_n \Bigg[2p_0 Q\left(a_0 \sqrt{\exp\left(\kappa_n^{SR} - \ln\left(4\epsilon_{SR} + 4\sigma_{e,SR}^2\right)\right)} \right) \\
&+ 2q_0 Q\left(b_0 \sqrt{\exp\left(\kappa_n^{SR} - \ln\left(4\epsilon_{SR} + 4\sigma_{e,SR}^2\right)\right)} \right) - 4p_0 q_0 Q\left(a_0 \sqrt{\exp\left(\kappa_n^{SR} - \ln\left(4\epsilon_{SR} + 4\sigma_{e,SR}^2\right)\right)} \right) \\
&\times Q\left(b_0 \sqrt{\exp\left(\kappa_n^{SR} - \ln\left(4\epsilon_{SR} + 4\sigma_{e,SR}^2\right)\right)} \right) \Bigg] Q\Big(\Delta_{RD}\kappa_n^{SR} - \Upsilon_{RD} - \Delta_{RD}\ln(\vartheta)\Big) \\
&\times \left[1 - Q(\sqrt{2}\xi_n) Q\Big(\Delta_{RD}\kappa_n^{SR} - \Upsilon_{RD} - \Delta_{RD}\ln(\vartheta)\Big) \right]^{N_r - 1} \\
&+ \frac{N_r}{\sqrt{\pi}} \sum_{n=1}^{N} w_n \Bigg[2p_0 Q\left(a_0 \sqrt{\exp\left(\kappa_n^{RD} - \ln\left(4\epsilon_{RD} + 4\sigma_{e,RD}^2\right)\right)} \right) \\
&+ 2q_0 Q\left(b_0 \sqrt{\exp\left(\kappa_n^{RD} - \ln\left(4\epsilon_{RD} + 4\sigma_{e,RD}^2\right)\right)} \right) 4p_0 q_0 Q\left(a_0 \sqrt{\exp\left(\kappa_n^{RD} - \ln\left(4\epsilon_{RD} + 4\sigma_{e,RD}^2\right)\right)} \right) \\
&\times Q\left(b_0 \sqrt{\exp\left(\kappa_n^{RD} - \ln\left(4\epsilon_{RD} + 4\sigma_{e,RD}^2\right)\right)} \right) \Bigg] Q\Big(\Delta_{SR}\kappa_n^{RD} - \Upsilon_{SR} + \Delta_{SR}\ln(\vartheta)\Big) \\
&\times \left[1 - Q(\sqrt{2}\xi_n) Q\Big(\Delta_{SR}\kappa_n^{RD} - \Upsilon_{SR} + \Delta_{SR}\ln(\vartheta)\Big) \right]^{N_r - 1}.
\end{aligned} \tag{4.19}$$

4.5.2 Cross QAM Scheme

Here, the ASER expression of XQAM scheme is derived for constellation size of 32 (XQAM-32). The conditional SER expression of XQAM for AWGN channel is given in (1.12). Using (1.12) into (4.18) and applying Theorem-4.1, the ASER expression of XQAM-32 scheme is obtained as

$$
\begin{aligned}
P_s^{\text{XQAM-32}}(e) &= \frac{N_r}{8\sqrt{\pi}} \sum_{n=1}^{N} w_n \Bigg[26Q\left(\sqrt{2A \exp\left(\kappa_n^{SR} - \ln\left(4\epsilon_{SR} + 4\sigma_{e,SR}^2\right)\right)}\right) \\
&+ Q\left(2\sqrt{A \exp\left(\kappa_n^{SR} - \ln\left(4\epsilon_{SR} + 4\sigma_{e,SR}^2\right)\right)}\right) - 23Q^2\left(\sqrt{2A \exp\left(\kappa_n^{SR} - \ln\left(4\epsilon_{SR} + 4\sigma_{e,SR}^2\right)\right)}\right)\Bigg] \\
&\times Q\Big(\Delta_{RD}\kappa_n^{SR} - \Upsilon_{RD} - \Delta_{RD}\ln(\vartheta)\Big)\Big[1 - Q(\sqrt{2}\xi_n)Q\Big(\Delta_{RD}\kappa_n^{SR} - \Upsilon_{RD} - \Delta_{RD}\ln(\vartheta)\Big)\Big]^{N_r-1} \\
&+ \frac{N_r}{\sqrt{8\pi}} \sum_{n=1}^{N} w_n \Bigg[26Q\left(\sqrt{2A \exp\left(\kappa_n^{RD} - \ln\left(4\epsilon_{RD} + 4\sigma_{e,RD}^2\right)\right)}\right) \\
&+ Q\left(2\sqrt{A \exp\left(\kappa_n^{RD} - \ln\left(4\epsilon_{RD} + 4\sigma_{e,RD}^2\right)\right)}\right) - 23Q^2\left(\sqrt{2A \exp\left(\kappa_n^{RD} - \ln\left(4\epsilon_{RD} + 4\sigma_{e,RD}^2\right)\right)}\right)\Bigg] \\
&\times Q\Big(\Delta_{SR}\kappa_n^{RD} - \Upsilon_{SR} + \Delta_{SR}\ln(\vartheta)\Big)\Big[1 - Q(\sqrt{2}\xi_n)Q\Big(\Delta_{SR}\kappa_n^{RD} - \Upsilon_{SR} + \Delta_{SR}\ln(\vartheta)\Big)\Big]^{N_r-1}.
\end{aligned}
\tag{4.20}
$$

4.5.3 Hexagonal QAM Scheme

The condition SER expression of M-ary HQAM constellation for AWGN channel is given as (1.13). Substituting (1.13) into (4.18), and applying Theorem-4.1 results in the following ASER expression of M-ary HQAM scheme for the considered system.

$$
\begin{aligned}
P_s^{\mathrm{HQAM}}(e) &= \frac{N_r}{\sqrt{\pi}} \sum_{n=1}^{N} w_n \Bigg[DQ\Bigg(\sqrt{q_1 \exp\left(\kappa_n^{SR} - \ln\left(4\epsilon_{SR} + 4\sigma_{e,SR}^2\right)\right)} \Bigg) + \frac{2}{3} D_C \\
&\times Q^2\Bigg(\sqrt{\frac{2q_1}{3} \exp\left(\kappa_n^{SR} - \ln\left(4\epsilon_{SR} + 4\sigma_{e,SR}^2\right)\right)} \Bigg) - 2D_C Q\Bigg(\sqrt{q_1 \exp\left(\kappa_n^{SR} - \ln\left(4\epsilon_{SR} + 4\sigma_{e,SR}^2\right)\right)} \Bigg) \\
&\times Q\Bigg(\sqrt{\frac{q_1}{3} \exp\left(\kappa_n^{SR} - \ln\left(4\epsilon_{SR} + 4\sigma_{e,SR}^2\right)\right)} \Bigg) \Bigg] Q\Big(\Delta_{RD} \kappa_n^{SR} - \Upsilon_{RD} - \Delta_{RD} \ln(\vartheta) \Big) \\
&\times \Bigg[1 - Q(\sqrt{2}\xi_n) Q\Big(\Delta_{RD} \kappa_n^{SR} - \Upsilon_{RD} - \Delta_{RD} \ln(\vartheta) \Big) \Bigg]^{N_r - 1} + \frac{N_r}{\sqrt{\pi}} \sum_{n=1}^{N} w_n \\
&\times \Bigg[DQ\Bigg(\sqrt{q_1 \exp\left(\kappa_n^{RD} - \ln\left(4\epsilon_{RD} + 4\sigma_{e,RD}^2\right)\right)} \Bigg) + \frac{2}{3} D_C \\
&\times Q^2\Bigg(\sqrt{\frac{2q_1}{3} \exp\left(\kappa_n^{RD} - \ln\left(4\epsilon_{RD} + 4\sigma_{e,RD}^2\right)\right)} \Bigg) - 2D_C Q\Bigg(\sqrt{q_1 \exp\left(\kappa_n^{RD} - \ln\left(4\epsilon_{RD} + 4\sigma_{e,RD}^2\right)\right)} \Bigg) \\
&\times Q\Bigg(\sqrt{\frac{q_1}{3} \exp\left(\kappa_n^{RD} - \ln\left(4\epsilon_{RD} + 4\sigma_{e,RD}^2\right)\right)} \Bigg) \Bigg] Q\Big(\Delta_{SR} \kappa_n^{RD} - \Upsilon_{SR} + \Delta_{SR} \ln(\vartheta) \Big) \\
&\times \Bigg[1 - Q(\sqrt{2}\xi_n) Q\Big(\Delta_{SR} \kappa_n^{RD} - \Upsilon_{SR} + \Delta_{SR} \ln(\vartheta) \Big) \Bigg]^{N_r - 1}.
\end{aligned}
\tag{4.21}
$$

4.6 Numerical and Simulation Results

In this section, the numerical investigations are presented, and validate accuracy of the derived analytical expressions using Monte-Carlo simulations. Unless otherwise stated, it is considered that $\lambda = 260$ nm, $k_s^{Ray} = 2.4 \times 10^{-4}$ m^{-1}, $k_s^{Mie} = 2.5 \times 10^{-4}$ m^{-1}, $k_a = 9 \times 10^{-4}$ m^{-1}, $C_n^2 = 5 \times 10^{-15}$ m$^{-2/3}$, $\iota_{eo} = \iota_{oe} = 1$, and Rx aperture area $A_r = 1.77$ cm^2. Distance between S and D nodes is $d_{SD} = 1000$ m [12, 73] and relays are assumed to be placed in the middle of S and D, $d_{SR_k} = d_{R_kD} = 500$ m. Further, elevation angles are configured as $\theta_{SR_k}^{Tx} = \theta_{R_kD}^{Rx} = 30^\circ$, and $\theta_{SR_k}^{Rx} = \theta_{R_kD}^{Tx} = 70^\circ$. [12] Furthermore, the beam divergence of Tx and FOV of Rx are considered to be 10° and 60°, respectively [10].

In Fig. 4.2, outage probability of the considered multi-relay system are presented for different system configurations, ρ values and turbulence strengths. Fig. 4.2(a)

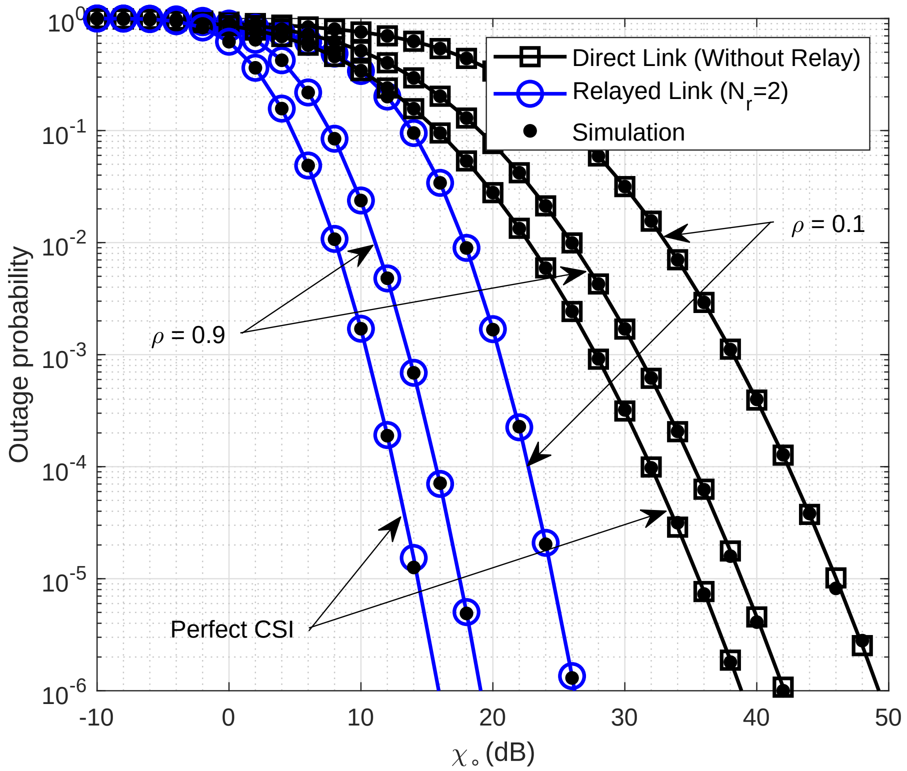

(a) Comparison of analytical and simulation results of P_{out} versus $\chi_\circ$ with the benchmark system for $N_r = 2$.

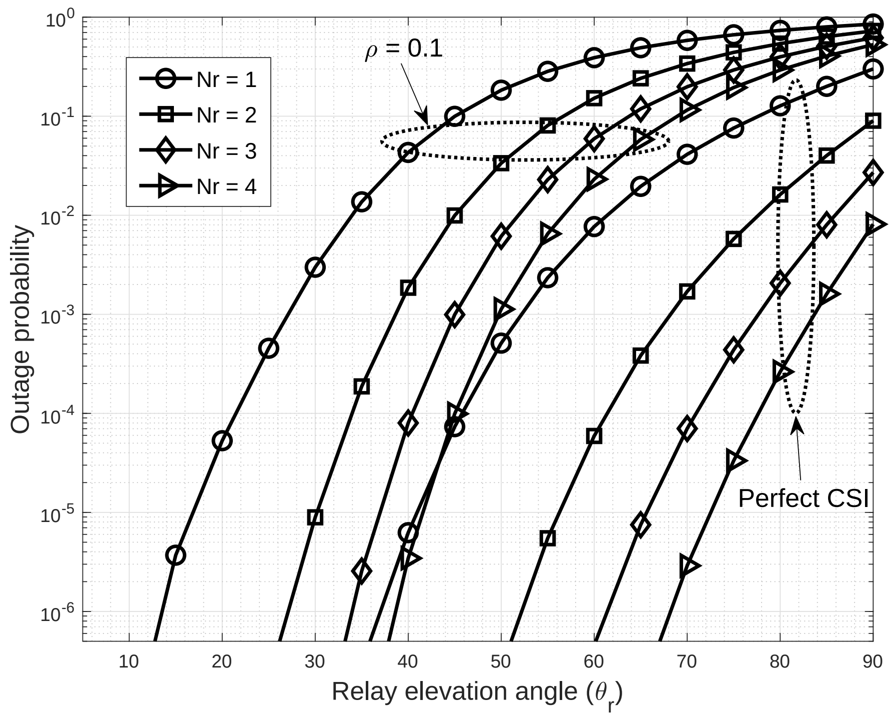

(b) P_{out} versus relay elevation angle (θ_r) for $N_r = (1, 2, 3, 4)$ and $\chi_\circ = 10$ dB.

Figure 4.2: Outage probability results for different average SNRs, number of relays, elevation angles, Rx FOVs, and turbulence strength (C_n^2).

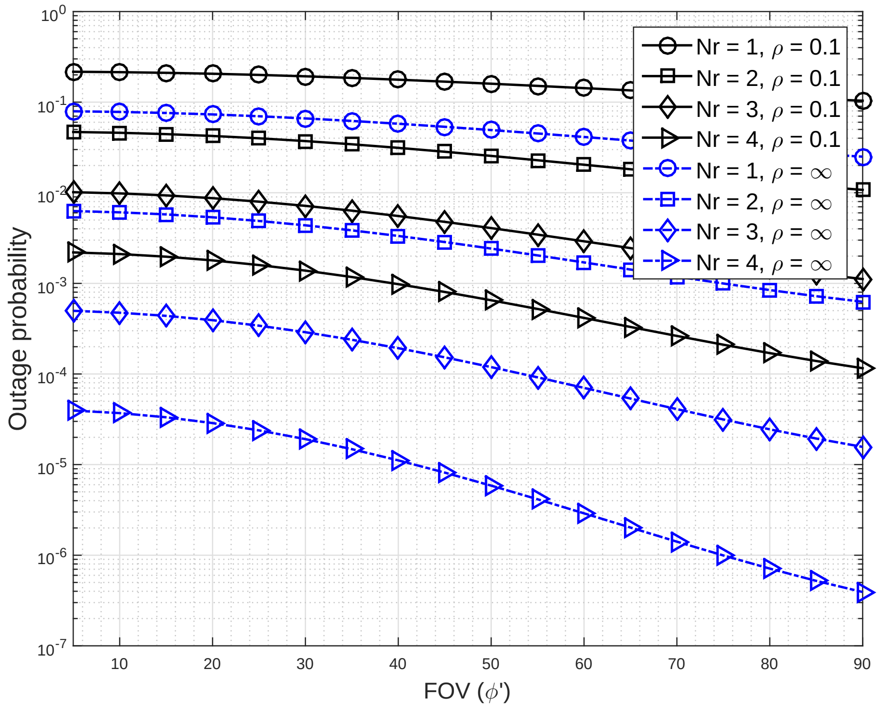

(c) P_{out} versus FOV (ϕ') for $\rho = (0.1, \infty)$ and $\chi_{\circ} = 10$ dB.

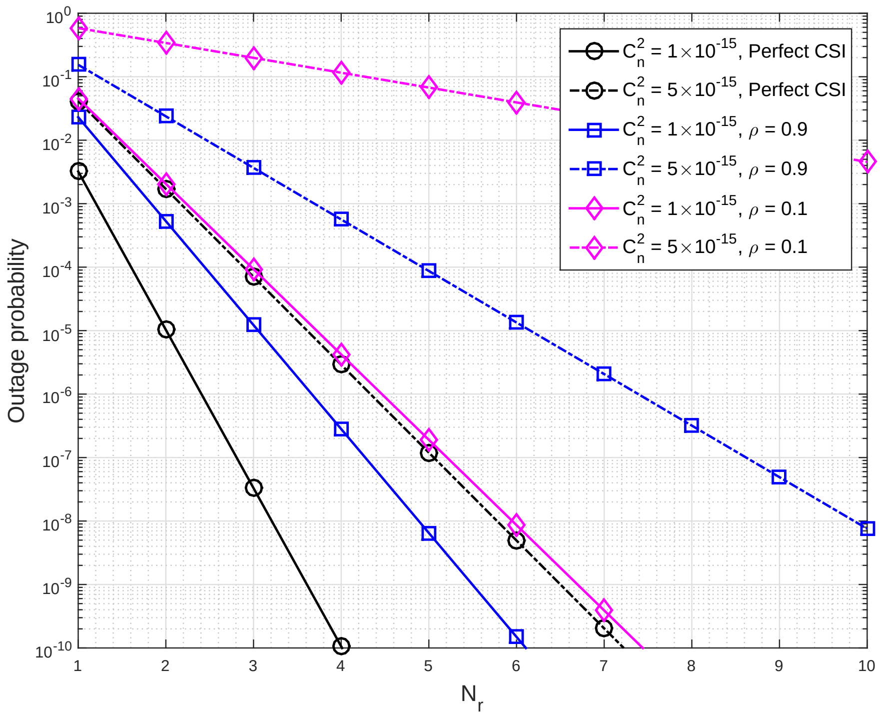

(d) P_{out} versus N_r for different C_n^2, $\rho = (0.1, 0.9, \infty)$ and $\chi_{\circ} = 10$ dB.

Figure 4.2: Outage probability results for different average SNRs, number of relays, elevation angles, Rx FOVs, and turbulence strength (C_n^2) (contd.).

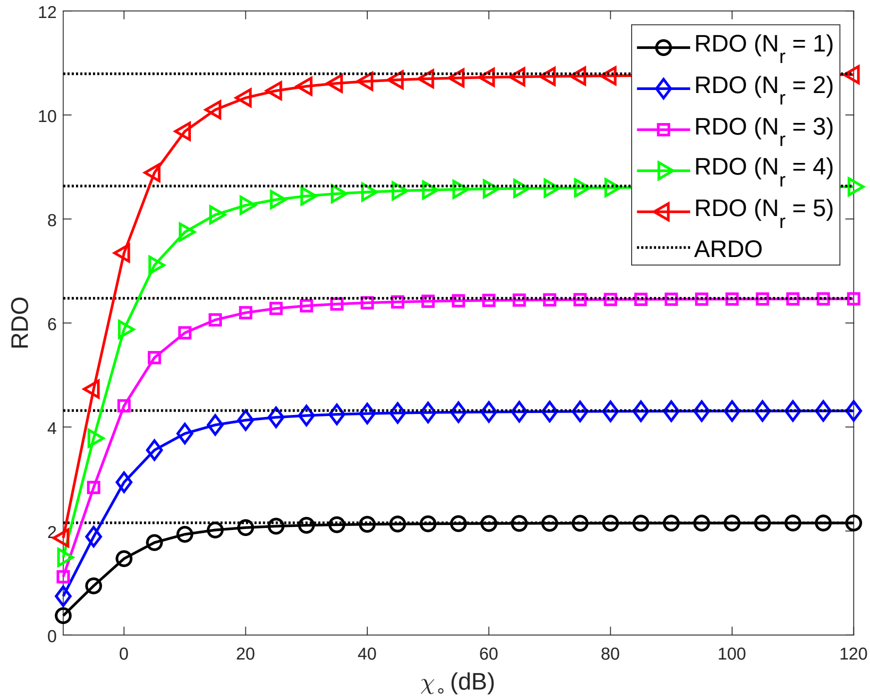

(a) RDO and ARDO versus $\chi_\circ$ for different N_r.

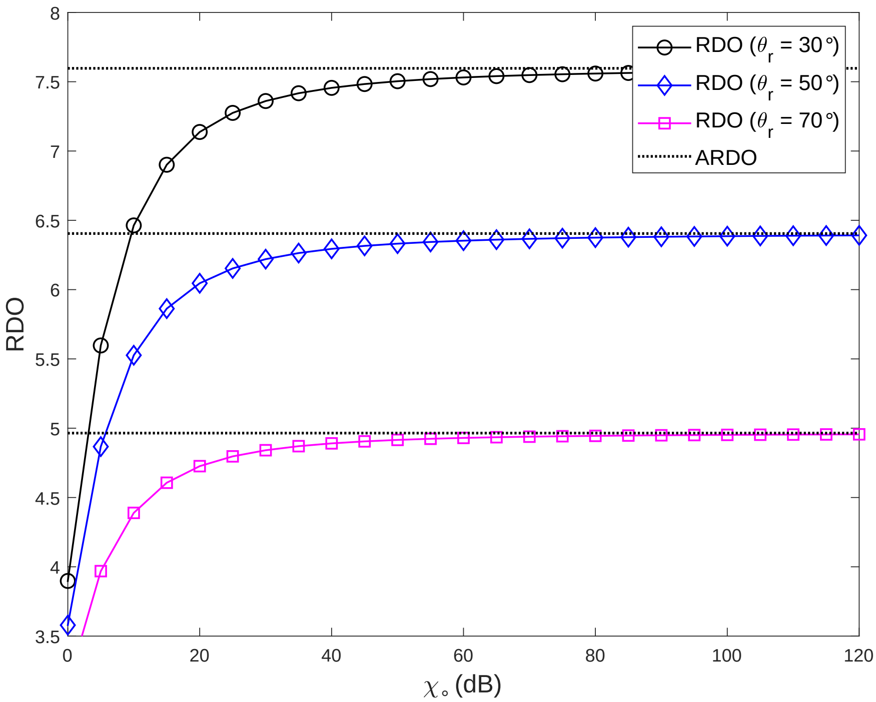

(b) RDO and ARDO versus $\chi_\circ$ for different θ_r.

Figure 4.3: RDO and ARDO for different number of relays and elevation angles.

compares the analytical and simulation results of the outage probability versus $\chi_\circ$ for $N_r = 2$, considering both the perfect CSI ($\rho \to \infty$) and imperfect CSI ($\rho = 0.1, 0.9$)

cases. It can be observed that the simulation results overlap with the theoretical results, thereby confirming accuracy of the derived analytical expressions of outage probability. It is observed that the outage probability increases with imperfections in the CSI for both the no-relay and relayed link. Further, considering no-relay case as the benchmark, it is observed that the use of relays significantly improves performance of the system as compared to the no-relay case for both perfect and imperfect channel estimates. As an example, for a target outage probability of 10^{-4}, with $N_r = 2$, an SNR gain of around 19.5 dB is achieved over benchmark case for both the perfect CSI ($\rho \to \infty$) and imperfect CSI ($\rho = 0.1, 0.9$) cases.

Fig. 4.2(b) illustrates the outage probability versus relay elevation angle ($\theta_{SR_k}^{Rx} = \theta_{R_kD}^{Tx} = \theta_r$) for $\rho = (0.1, \infty)$ and $N_r = (1, 2, 3, 4)$. It can be seen that irrespective of the value of N_r and ρ, the system performs better for a lower elevation angle. This performance improvement can be attributed to the reduced distance from Tx and Rx to the CV for a lower elevation angle. In Fig. 4.2(c), theoretical results of outage probability versus Rx FOV angles ($\phi_{SR_k}^{Rx} = \phi_{R_kD}^{Rx} = \phi'$) are presented for different values of N_r and ρ. It is shown that the system performs better for a large value of FOV irrespective of the number of relays and the quality of channel estimation. This is because, with large FOV, more number of photons are received by the Rx, thereby resulting in improved signal quality. This results in significant reduction in the outage probability of the considered system for a given $\chi_\circ$.

Fig. 4.2(d) presents theoretical results of outage probability versus N_r for different values of C_n^2, considering both perfect CSI and imperfect CSI cases. It is observed that for all the scenarios, the outage probability improves with increase in number of relays. However, the imperfect estimate of the channel severely degrades the system performance and requires more number of relays to achieve the same performance as that of perfect CSI case. As an example, for $C_n^2 = 1 \times 10^{-5}$, and a target outage probability of 10^{-5}, the required number of relays increases by 1.5 times and 1.8 times for $\rho = 0.9$ and $\rho = 0.1$, respectively, when compared to the perfect CSI case. This can be a tradeoff for system designers to increase relays or

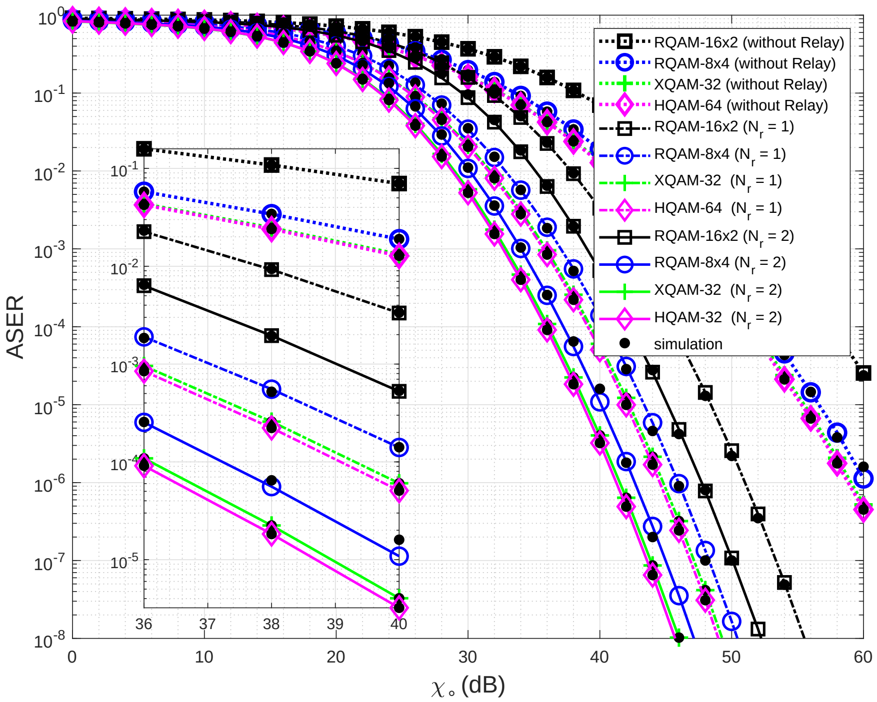

(a) 32-points constellations with comparison to the benchmark system for $N_r = (1, 2)$, and $\rho = 0.1$.

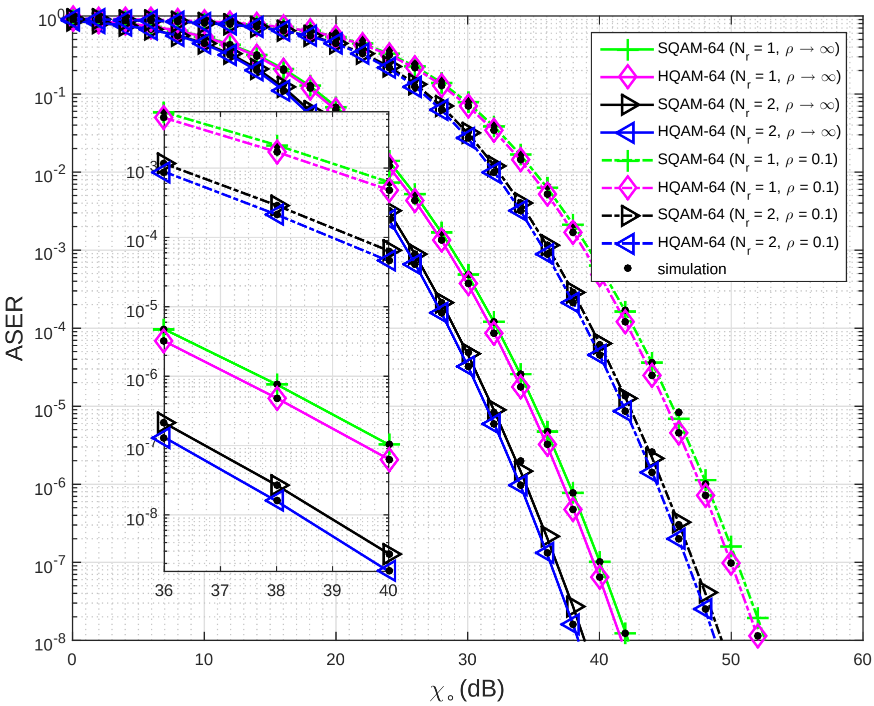

(b) 64-points constellations for $N_r = (1, 2)$, and $\rho = (0.1, \infty)$.

Figure 4.4: Analytical and simulation results of ASER versus SNR.

use more sophisticated computationally complex CSI estimator at the Rx. Further, it is observed that the outage probability of the system increases with C_n^2. This is

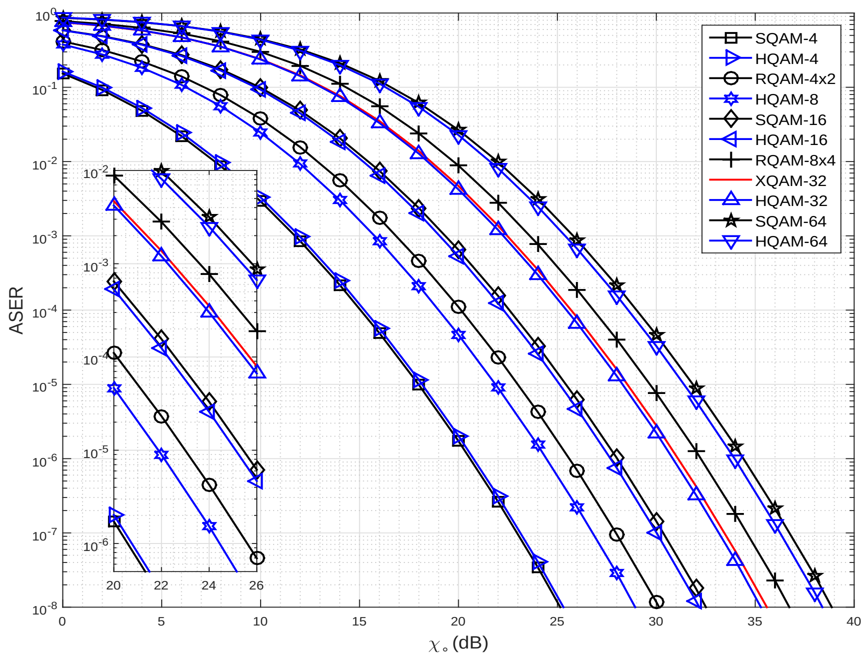

Figure 4.5: Theoretical ASER results for $4, 8, 16, 32, 64$-points constellations in perfect CSI conditions and $N_r = 2$.

because, the turbulence scintillation index is directly proportional to the C_n^2, as a result, higher value of C_n^2 increases fading severity and adversely affects the system performance. Furthermore, as an interesting observation, it can be observed that the impact of the increased fading severity becomes worse as the imperfection in the channel estimation increases.

Fig. 4.3 depicts RDO of the considered system for different configurations. The ARDO is also plotted considering high SNR values for asymptotic analysis. In Fig 4.3(a), it is observed that the diversity order of the system improves with the increase in the number of relays. For instance, ARDO of $2.1584, 4.3168, 6.4752, 8.6336$, and 10.7919 are obtained for $N_r = 1, 2, 3, 4$ and 5, respectively. The observed asymptotic values coincides with the RDO curves for higher $\chi_\circ$, thereby confirming accuracy of the derived ARDO expression in (4.17). Fig 4.3(b) shows the RDO and ARDO curves for $N_r = 2$ and different θ_r. As an important observation, it can be seen that, for a constant N_r, the RDO of the system significantly improves for lower elevation angles at relay nodes. It is observed that the ARDO of the system comes out to be

$7.1272, 5.6626$, and 4.3168 for $\beta_r = 30°, 50°$, and $70°$, respectively.

Fig. 4.4 presents both numerical and simulation results of ASER versus $\chi_\circ$ for different modulation schemes, N_r, and ρ. It is observed that for all cases, analytical results and simulation results closely overlap, thus, validating correctness of the derived ASER analytical expressions. Fig. 4.4(a) presents comparison of different 32-points RQAM, HQAM, and XQAM constellations for the considered multi-relay case with benchmark system for $N_r = (1, 2)$ and $\rho = 0.1$. It is observed that the use of relays provide significant gain in terms of the required SNR for a target ASER. Considering a target ASER of 10^{-5}, the SNR gains of around 13 dB, 13.14 dB, 13.28 dB, and 13.3 dB are obtained with $N_r = 1$ for RQAM-16×2, RQAM-8×4, XQAM-32, and HQAM-32, respectively, when compared with no-relay case. Further, ASER performance of the system improves significantly by increasing the number of relays. As an example, it is observed that for $N_r = 2$, considerable SNR gains of approximately 3.3 dB, 3.3 dB, 3.1 dB, and 3.2 dB are obtained for RQAM-16×2, RQAM-8×4, XQAM-32, and HQAM-32, respectively, as compared with $N_r = 1$.

In Fig. 4.4(b), the ASER performance of SQAM-64 and HQAM-64 constellations are presented for $N_r = (1, 2)$ and $\rho = (0.1, \infty)$. It is observed that HQAM-64 shows better performance as compared to SQAM-64 schemes due to its higher value of q, and low peak and average powers as compared to SQAM. Further, it is observed that irrespective of the selected modulation scheme, the ASER of the system increases as the quality of the channel estimate deteriorates. As an example, to achieve a target ASER of 10^{-5}, for $\rho = 0.1$, HQAM-64 provides a significant gain of 0.4 dB as compared to SQAM-64. Further, using two relays ($N_r = 2$) provides an additional gain of approx. 3.3 dB when compared with single relay ($N_r = 1$) case, due to the improved diversity order.

Fig. 4.5, illustrates the ASER performance comparison of RQAM, SQAM, XQAM, and HQAM schemes with different constellation points for perfect CSI case and $N_r = 2$. It can be seen that XQAM-32 outperforms RQAM-8×4 with a significant gain of 1.1 dB. This is because, XQAM is spectrally more efficient than RQAM for odd number of bits, due to its better peak and average powers as compared to RQAM. It can be seen that, except for HQAM-4, HQAM outperforms SQAM, RQAM, and XQAM irrespective of the number of constellation points. For perfect CSI case and $N_r = 2$, for ASER of 10^{-5}, HQAM-64 provides approx. 0.4 dB gain over SQAM-64; HQAM-32 provides approx. 0.24 dB gain over XQAM-32; and HQAM-16 provides SNR gain of approx. 0.3 dB over SQAM-16. This performance improvement can be attributed to the optimum placement of constellation points in HQAM as compared to other modulation schemes.

Finally, Fig. 4.6 shows the comparison of the outage probability of the parallel relaying model considered in Chapter 3 with the best relay selection model of the current Chapter. It can be seen that the best relay selection outperforms parallel relaying for wide range of relay elevation angles. For instance, for a target outage probability of 10^{-4}, the significant SNR gain of 4.6 dB, 6 dB, and 7.6 dB is achieved by using best relay selection as opposed to parallel relaying for the elevation angles of 20°, 50°, and 80°, respectively.

4.7 Summary

In this chapter, a DF based cooperative NLOS UVC system employing the best relay selection technique is proposed. The outage and ASER analysis of the system is carried out for practical imperfect knowledge of CSI at the Rx. The RDO and ARDO of the system are derived and it is observed that the ARDO of the system improves with the increase in the number of relays. Further, it is shown that, for a fixed number of relays the diversity order of the system improves for the lower elevation angles at the relay nodes. It is also shown that imperfect CSI downgrades the performance of the considered NLOS UVC system. However, the performance loss due to imperfect CSI can be compensated to an extent by using cooperating relaying techniques. Further, it is shown that the lower elevation angle

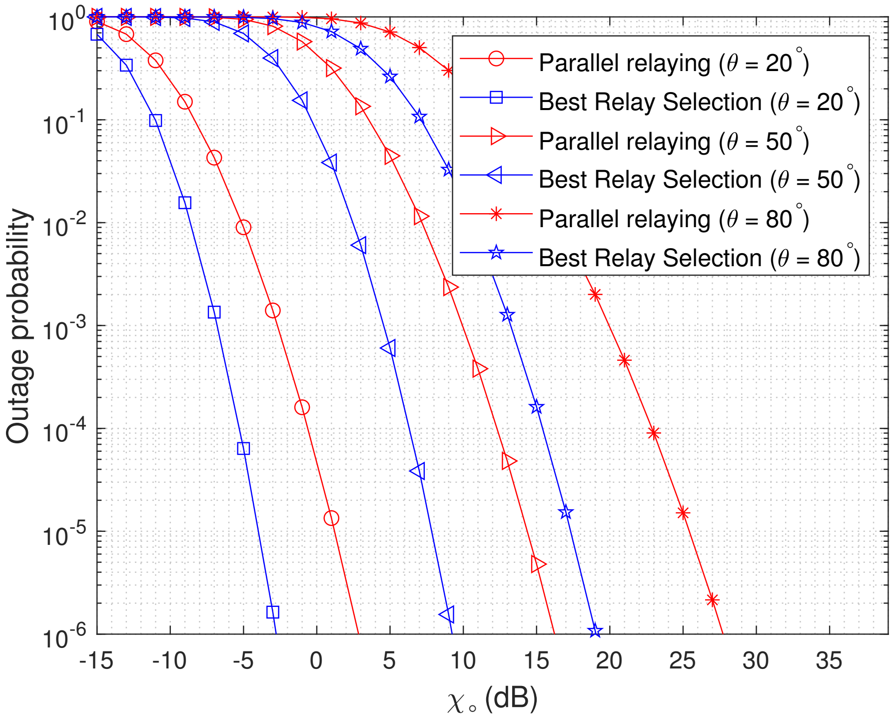

Figure 4.6: Outage probability comparison between parallel relaying of Chapter 3 versus the best relay selection of Chapter 4 ($N_r = 2$, $\chi_{th} = 3$ dB).

at the relay, and higher Rx FOV, significantly improves the system performance. As an interesting observation, it is seen that the impact of imperfect CSI becomes severe as the turbulence severity increases, which results in higher SNR requirements to achieve the target system's performance. Furthermore, it is observed that the HQAM scheme performs significantly better and is robust than RQAM, SQAM, and XQAM schemes for the same average constellation energy and constellation size in multi-relay UVC systems. All communication links in the dual-hop cooperative system model studied in this chapter are considered to be UV. In the following chapter, a novel hybrid RF/NLOS UVC system is examined to address the issue of extending the communication range of an RF system to RF-restricted regions with no LOS availability.

Chapter 5

Relay Assisted Hybrid RF-NLOS UVC System with Imperfect Channel Estimation

5.1 Introduction

As discussed earlier, the UVC overcomes the limitations of FSO and VLC systems due to its unique ability to operate in NLOS mode. In previous chapters, the challenge of turbulence induced fading and high path loss in UVC were addressed using space diversity and cooperative relaying techniques. In this chapter, the challenge of providing long distance wireless connectivity to RF prohibited areas with no LOS availability is addressed by mixing NLOS UVC with RF communication using a cooperative DF relay. There are numerous practical applications in which the proposed system model fits best. One such application is the radiology department in hospitals where the use of RF are restricted due to the possible interference with the medical imaging equipment. Another application is to provide wireless connectivity to military personnel during covert operations due to security reasons as RF signals are vulnerable to eavesdropping. In this arrangement, NLOS UVC can be used in the RF prohibited area, which is comparatively small, while using RF link for the remaining distance.

Recently, for increased coverage, hybrid of RF with OWC technologies such as FSO and VLC are extensively investigated in the literature [40, 55–57, 69, 71, 82–84]. In [57], the performance of a fixed-gain AF relayed dual-hop mixed FSO/RF is evaluated with FSO and RF links modeled using Gamma-Gamma and Nakagami-m distribution, respectively. In [69], the authors' conducted the performance analysis of a multi-hop hybrid FSO/RF communication system in terms of outage probability and BER for differential phase-shift keying (DPSK) scheme. In [55], the authors' investigated the performance of a DF relayed hybrid RF/VLC system in terms of secrecy outage probability, capacity, and consumed power. In [85], Pan et al. considered a MISO simultaneous wireless information and power transfer (SWIPT) based system employing TAS and studied its physical layer security performance for Rayleigh fading and imperfect CSI case. This work was extended in [56] for mixed RF/FSO system. The fading distributions for the RF and FSO links are considered to be Nakagami-m and Málaga, respectively. In [40], Praveen et al. carried out an ASER performance analysis of hybrid RF/FSO system for higher-order modulation schemes. In [82], Sanya et al. conducted the performance study of a fixed-gain AF relayed dual-hop mixed RF-FSO communication system considering Nakagami-m fading and Gamma-Gamma fading for the RF and FSO links, respectively; In [83] the authors considered a DF based dual-hop mixed RF-FSO communication system and evaluated its BER performance and capacity, considering pointing error in the FSO link. In [71], the authors' studied the outage and BER performance of a novel multi-user multi-hop hybrid FSO/RF communication system considering fixed-gain and variable-gain AF relay; and in [84], the outage probability, ASER, and capacity performance of a mixed RF/FSO system were studied using Rayleigh fading model for the RF link, and unified Gamma–Gamma atmospheric turbulence fading model for the FSO link. A few more recently published studies in hybrid RF/FSO communication systems are [86–88].

5.1.1 Contributions

The ASER performance of the futuristic higher-order modulation schemes for dual-hop hybrid RF/NLOS UVC DF relay system by considering Rayleigh and LN distributions for RF and NLOS UVC links, respectively, is not available in the literature. Further, in the current UVC literature, CSI is usually assumed to be perfectly known at Rx. However, it is not possible to obtain the perfect estimate of CSI in practical systems [78]. Therefore, it is worthwhile to evaluate the robustness of the proposed system under such practical constraints. Following are major contributions of this work:

- The outage probability of the considered system is derived, and the impact of CEE on the system's outage performance is investigated under various scenarios, including when the actual CSI and estimated CSI are completely correlated, and when their correlation is moderate or severely poor.

- The diversity order analysis of the considered system is performed and it is shown that with the increase in CEE, the rate at which the diversity order converges to its eventual value of one slows down.

- A novel closed-form expression of the PDF of the e2e SNR is derived. Further, the PDF based approach is used to derive the generic analytical expression of ASER.

- The SIM based technique for NLOS UVC link is considered, and the system's ASER performance is evaluated for futuristic higher order modulation schemes including RQAM, XQAM, and HQAM. Thorough numerical investigation is performed to compare the performance of these modulation methods for different CEE.

- Extensive numerical study is carried out and some highly valuable insights are drawn. The impact of different CEE of the RF and UV link is studied, and it is demonstrated that the RF link is more susceptible to CEE as compared to

UV link at high SNR. Further, the impact of elevations angles on the overall system performance is evaluated and it is shown that keeping the elevation angle below 70° results in better performance.

5.2 System and Channel Model

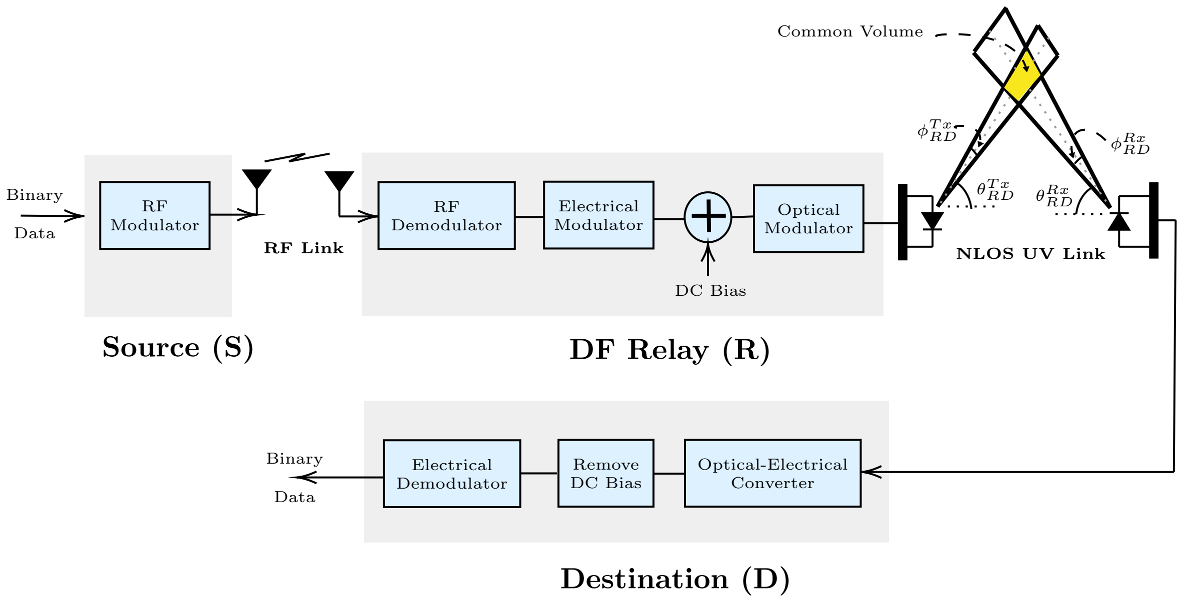

Figure 5.1: System model of dual-hop hybrid RF/NLOS UVC DF cooperative system.

Fig. 5.1 shows a dual-hop hybrid RF/NLOS UVC DF cooperative communication system consisting of source (S) node, relay (R) node, and a destination (D) node. All nodes are assumed to be equipped with a single Tx and Rx, and operating in a half-duplex mode. The SR link is considered to be an RF link with channel coefficient following a Rayleigh distribution, and RD is NLOS UVC link modeled using LN distribution assuming weak turbulence. The narrowband fading model is assumed for both the RF and UV link. In the NLOS UVC channel, temporal dispersion (T_d) can reach 1μs [89]. If the symbol transmission rate $R_s \geq \frac{1}{T_d}$, the ISI may become a concern. The transmission bandwidth is considered to be well below 1 Mega symbols/second to support our assumption of narrowband fading model. Hence, the pulse broadening and the impact of phase shift are considered to be negligible in the proposed system design analysis. These assumptions draw the benchmark result for practical system design insights. Relay R uses DF relaying protocols and has hybrid capabilities. It first decodes the data transmitted by S over SR link, re-modulates the data using the SIM technique, and transmits it towards D over the NLOS UVC link. In a practical system, since the CSI is estimated at the Rx, the imperfect CSI at R and D is considered. For unbiased MMSE used at Rx, actual channel (h_j) and its estimate ($\hat{h}_j$) are related as $h_j = \hat{h}_j + e_j$ in which $e_j \sim \mathcal{N}(0, \Omega_{e_j})$ [90–93] is the CEE of the j^{th} link, where $j \in \{sr, rd\}$. CEE variance can be computed as $\Omega_{e_j} = \frac{\Omega_{h_j}}{1+\rho\overline{\chi}_j\Omega_{h_j}}$, where ρ is the correlation coefficient between h_j and $\hat{h}_j$, $\overline{\chi}_j$ is the average received SNR of the j^{th} link, and Ω_{h_j} is the variance of h_j. The variance of $\hat{h}$ can be computed as $\Omega_{\hat{h}_j} = \Omega_{h_j} - \Omega_{e_j}$.

The e2e SNR of a dual-hop DF relaying system is given by [12, 76]

$$\chi_{e2e} = \min(\chi_{sr}, \chi_{rd}), \tag{5.1}$$

where $\chi_j = \overline{\chi}_j\hat{h}_j^2/(1+\overline{\chi}_j\Omega_{e_j})$ is the instantaneous electrical SNRs of SR and RD links, respectively. It is assumed that the channel coefficient of RF SR link follows Rayleigh distribution, and hence χ_{sr} will have exponential distribution with PDF, and CDF given by [14]

$$f_{\chi_{sr}}(\chi) = \frac{1+\overline{\chi}_{sr}\Omega_{e_{sr}}}{\overline{\chi}_{sr}} \exp\Big(-\frac{(1+\overline{\chi}_{sr}\Omega_{e_{sr}})\chi}{\overline{\chi}_{sr}}\Big), \tag{5.2}$$

and

$$F_{\chi_{sr}}(\chi) = 1 - \exp\Big(-\frac{(1+\overline{\chi}_{sr}\Omega_{e_{sr}})\chi}{\overline{\chi}_{sr}}\Big), \tag{5.3}$$

respectively. The RD link uses a UV-C frequency band for communication and operates in NLOS mode. The RD link is assumed to experience the atmospheric turbulence with the scintillation index adhering to the weak turbulence condition, $\sigma^2_{\chi_{rd}} \leq 1.2$ [12]. For weak turbulence, the channel coefficient h_{rd} is modelled using LN distribution, $\ln(h_{rd}) \sim \mathcal{N}(\mu_{h_{rd}}, \sigma^2_{h_{rd}})$. Parameters $\mu_{h_{rd}}$ and $\sigma_{h_{rd}}$, respectively, are the mean and standard deviation of the corresponding Gaussian random variable, $\ln(h_{rd})$ [14]. Using transformation of random variable, it can be shown that $\chi_{rd} = [\overline{\chi}_{rd}/(1+\overline{\chi}_{rd}\Omega_{e_{rd}})]h_{rd}^2$ also follows LN distribution, $\ln(\chi_{rd}) \sim \mathcal{N}\big(2\mu_{h_{rd}} + ln(\overline{\chi}_{rd}/(1+\overline{\chi}_{rd}\Omega_{e_{rd}})), 4\sigma_{h_{rd}^2}\big)$ [64]. The PDF and CDF of χ_{rd} is given as [12, 73],

$$f_{\chi_{rd}}(\chi) = \frac{\exp\left(\frac{-\left[\ln\left((1+\overline{\chi}_{rd}\Omega_{e_{rd}})\chi/\overline{\chi}_{rd}\right)-2\mu_{h_{rd}}\right]^2}{8\sigma_{h_{rd}}^2}\right)}{2\sqrt{2\pi}\,\sigma_{h_{rd}}\chi}, \tag{5.4}$$

$$F_{\chi_{rd}}(\chi) = 1 - Q\left(\frac{\ln((1+\overline{\chi}_{rd}\Omega_{e_{rd}})\chi/\overline{\chi}_{rd}) - 2\mu_{h_{rd}}}{2\sigma_{h_{rd}}}\right). \tag{5.5}$$

5.3 Outage Probability

Outage probability is computed by evaluating the CDF of e2e SNR at χ_{th}.

$$P_{out} = F_{\chi_{e2e}}(\chi_{th}) = \Pr[\chi_{e2e} \leq \chi_{th}], \tag{5.6}$$

where $F_{\chi_{e2e}}(\cdot)$ represents the CDF of χ_{e2e}. From (5.1) and (5.6) we get,

$$P_{out} = \Pr[\min(\chi_{sr}, \chi_{rd}) \leq \chi_{th}] = 1 - \left[1 - F_{\chi_{sr}}(\chi_{th})\right]\left[1 - F_{\chi_{rd}}(\chi_{th})\right]. \tag{5.7}$$

Using (5.3) and (5.5) in (5.7), the outage probability of the considered system is computed as

$$P_{out} = 1 - \exp\left(-\frac{(1+\overline{\chi}_{sr}\Omega_{e_{sr}})\chi_{th}}{\overline{\chi}_{sr}}\right)Q\left(\frac{\ln((1+\overline{\chi}_{rd}\Omega_{e_{rd}})\chi_{th}/\overline{\chi}_{rd}) - 2\mu_{h_{rd}}}{2\sigma_{h_{rd}}}\right). \tag{5.8}$$

5.4 Diversity Order Analysis

The diversity order is calculated to obtain immediate insights on the system's performance at high SNR values. On a log-log scale, the term "diversity order" refers to the negative asymptotic slope of outage probability versus SNR. For finite SNR, the diversity order is defined as [47]

$$DO = \frac{\partial \ln P_{out}}{\partial \ln \chi_\circ}. \tag{5.9}$$

where $\chi_\circ = \overline{\chi}_{sr} = \overline{\chi}_{rd}$. On substituting (5.8) into (5.9) and simplifying the resulting expression for high SNR, we obtain the diversity order of the system as given in (5.10), in which $\kappa_{sr} = \frac{1+\rho_{sr}}{\rho_{sr}}$, and $\kappa_{rd} = \frac{1+\rho_{rd}}{\rho_{rd}}$.

$$DO = \frac{\exp\left(-\frac{\chi_{th}\kappa_{sr}}{\chi_\circ}\right)\left[-\frac{1}{2\sqrt{2\pi}\sigma_{h_{rd}}}\exp\left(-\frac{(\ln(\chi_{th}\kappa_{rd}/\chi_\circ)-2\mu_{h_{rd}})^2}{8\sigma_{h_{rd}}^2}\right) - \frac{\chi_{th}\kappa_{sr}}{\chi_\circ}Q\left(\frac{\ln(\chi_{th}\kappa_{rd}/\chi_\circ)-2\mu_{h_{rd}}}{2\,\sigma_{h_{rd}}}\right)\right]}{1-\exp\left(-\frac{\chi_{th}\kappa_{sr}}{\chi_\circ}\right)Q\left(\frac{\ln(\chi_{th}\kappa_{rd}/\chi_\circ)-2\mu_{h_{rd}}}{2\,\sigma_{h_{rd}}}\right)}. \tag{5.10}$$

5.5 ASER Analysis

In this section, we evaluate ASER expression of the various QAM schemes using the PDF based approach as follows,

$$P_s(e) = \mathbb{E}[P_s(e|\chi_{e2e})] = \int_0^\infty P_s(e|\chi) f_{\chi_{e2e}}(\chi) d\chi, \tag{5.11}$$

where $P_s(e|\chi)$ is the conditional symbol error probability of received SNR. The PDF of e2e SNR can be computed by differentiating P_{out} derived in (5.8), and is given by

$$\begin{aligned} f_{e2e}(\chi) = &\left(\frac{1+\overline{\chi}_{sr}\Omega_{e_{sr}}}{\overline{\chi}_{sr}}\right)\exp\left(\frac{-(1+\overline{\chi}_{sr}\Omega_{e_{sr}})\chi}{\overline{\chi}_{sr}}\right)Q\left(\frac{\ln((1+\overline{\chi}_{rd}\Omega_{e_{rd}})\chi/\overline{\chi}_{rd})-2\mu_{h_{rd}}}{2\sigma_{h_{rd}}}\right) \\ &+ \frac{\exp\left(\frac{-\left[\ln\left((1+\overline{\chi}_{rd}\Omega_{e_{rd}})\chi/\overline{\chi}_{rd}\right)-2\mu_{h_{rd}}\right]^2}{8\sigma_{h_{rd}}^2}\right)}{2\sqrt{2\pi}\,\sigma_{h_{rd}}\chi}\exp\left(\frac{-(1+\overline{\chi}_{sr}\Omega_{e_{sr}})\chi}{\overline{\chi}_{sr}}\right). \end{aligned} \tag{5.12}$$

Next, we define a theorem that will be used to evaluate convenient closed-form analytical ASER expressions for different modulation schemes.

Theorem 5.1. Let $\Psi(\cdot)$ is an arbitrary function of RV χ_{e2e}, then

$$\mathbb{E}[\Psi(\chi_{e2e})] = \mathcal{I}_1 - \mathcal{I}_2, \tag{5.13}$$

where,

$$\mathcal{I}_1 = \Big(\frac{1+\overline{\chi}_{sr}\Omega_{e_{sr}}}{\overline{\chi}_{sr}}\Big)\int_0^{\infty}\Psi(\chi)\exp\left(\frac{-(1+\overline{\chi}_{sr}\Omega_{e_{sr}})\chi}{\overline{\chi}_{sr}}\right)d\chi, \tag{5.14}$$

and

$$\mathcal{I}_2 = \frac{1}{\sqrt{\pi}}\sum_{i=1}^{N} w_i\Psi\Big(\frac{\overline{\chi}_{rd}}{1+\overline{\chi}_{rd}\Omega_{e_{rd}}}\exp\left(2\sqrt{2}\,\sigma_{h_{rd}}y_i+2\mu_{h_{rd}}\right)\Big)\exp\left(\frac{-\overline{\chi}_{rd}(1+\overline{\chi}_{sr}\Omega_{e_{sr}}))}{\overline{\chi}_{sr}(1+\overline{\chi}_{rd}\Omega_{e_{rd}})}\right.$$
$$\left.\times\exp\left(2\sqrt{2}\,\sigma_{h_{rd}}y_i+2\mu_{h_{rd}}\right)\right)\left\{\frac{2\,\sigma_{h_{rd}}\overline{\chi}_{rd}(1+\overline{\chi}_{sr}\Omega_{e_{sr}})}{\overline{\chi}_{sr}(1+\overline{\chi}_{rd}\Omega_{e_{rd}})}\frac{\exp\left(2\sqrt{2}\,\sigma_{h_{rd}}y_i+2\mu_{h_{rd}}\right)}{\sqrt{2y_i^2+1}}-1\right\}, \tag{5.15}$$

where $\{y_i\}_{i=1}^{N}$ and $\{w_i\}_{i=1}^{N}$, respectively, are zeros and weights of a N^{th} order Hermite polynomial, whose values are tabulated in [63, Table 25.10] for $N=2$ to 20.

Proof. See Appendix C.1. ■

5.5.1 Rectangular QAM Scheme

The conditional SER expression for RQAM scheme is given as (1.11). On substituting (1.11) into (5.11) and applying Theorem 5.1, the generalized novel closed-form ASER expression of RQAM scheme for RF/NLOS UVC system is evaluated as

$$P_s^{\mathrm{RQAM}}(e) = p_0+q_0-p_0q_0-p_0\sqrt{\frac{\overline{\chi}_{sr}a_0^2}{(2(1+\overline{\chi}_{sr}\Omega_{e_{sr}})+\overline{\chi}_{sr}a_0^2)}}-q_0\sqrt{\frac{\overline{\chi}_{sr}b_0^2}{(2(1+\overline{\chi}_{sr}\Omega_{e_{sr}})+\overline{\chi}_{sr}b_0^2)}}$$
$$+\frac{2p_0q_0}{\pi}\sqrt{\frac{\overline{\chi}_{sr}a_0^2}{(2(1+\overline{\chi}_{sr}\Omega_{e_{sr}})+\overline{\chi}_{sr}a_0^2)}}\tan^{-1}\left(\frac{a_0}{b_0}\sqrt{\frac{(2(1+\overline{\chi}_{sr}\Omega_{e_{sr}})+\overline{\chi}_{sr}a_0^2)}{\overline{\chi}_{sr}a_0^2}}\right)$$
$$+\frac{2p_0q_0}{\pi}\sqrt{\frac{\overline{\chi}_{sr}b_0^2}{(2(1+\overline{\chi}_{sr}\Omega_{e_{sr}})+\overline{\chi}_{sr}b_0^2)}}\tan^{-1}\left(\frac{b_0}{a_0}\sqrt{\frac{(2(1+\overline{\chi}_{sr}\Omega_{e_{sr}})+\overline{\chi}_{sr}b_0^2)}{\overline{\chi}_{sr}b_0^2}}\right)-\frac{1}{\sqrt{\pi}}\sum_{i=1}^{N}w_i$$
$$\times\exp\left(\frac{-(1+\overline{\chi}_{sr}\Omega_{e_{sr}})\overline{\chi}_{rd}\exp\left[2\sqrt{2}\,\sigma_{h_{rd}}y_i+2\mu_{h_{rd}}\right]}{(1+\overline{\chi}_{rd}\Omega_{e_{rd}})\overline{\chi}_{sr}}\right)\left[2p_0Q\left(a_0\sqrt{\frac{\overline{\chi}_{rd}}{(1+\overline{\chi}_{rd}\Omega_{e_{rd}})}}\right.\right.$$
$$\left.\times\sqrt{\exp\left[2\sqrt{2}\,\sigma_{h_{rd}}y_i+2\mu_{h_{rd}}\right]}\right)+2q_0Q\left(b_0\sqrt{\frac{\overline{\chi}_{rd}}{(1+\overline{\chi}_{rd}\Omega_{e_{rd}})}\exp\left[2\sqrt{2}\,\sigma_{h_{rd}}y_i+2\mu_{h_{rd}}\right]}\right)$$
$$-4p_0q_0Q\left(a_0\sqrt{\frac{\overline{\chi}_{rd}}{(1+\overline{\chi}_{rd}\Omega_{e_{rd}})}\exp\left[2\sqrt{2}\,\sigma_{h_{rd}}y_i+2\mu_{h_{rd}}\right]}\right)Q\left(b_0\sqrt{\frac{\overline{\chi}_{rd}}{(1+\overline{\chi}_{rd}\Omega_{e_{rd}})}}\right.$$
$$\left.\left.\times\sqrt{\exp\left[2\sqrt{2}\,\sigma_{h_{rd}}y_i+2\mu_{h_{rd}}\right]}\right)\right]\left[\frac{2\sigma_{h_{rd}}\overline{\chi}_{rd}}{(1+\overline{\chi}_{rd}\Omega_{e_{rd}})}\exp\left[2\sqrt{2}\,\sigma_{h_{rd}}y_i+2\mu_{h_{rd}}\right](2y_i^2+1)^{-1/2}-1\right]. \tag{5.16}$$

Obtaining (5.16) involves solving the following integral

$$\mathcal{I}_1 = \Big(\frac{1+\overline{\chi}_{sr}\Omega_{e_{sr}}}{\overline{\chi}_{sr}}\Big)\int_0^{\infty}\Big[2p_0Q(a_0\sqrt{\chi}) + 2q_0Q(b_0\sqrt{\chi}) - 4p_0q_0Q(a_0\sqrt{\chi})Q(b_0\sqrt{\chi})\Big] \times \exp\left(\frac{-(1+\overline{\chi}_{sr}\Omega_{e_{sr}})\chi}{\overline{\chi}_{sr}}\right)d\chi. \tag{5.17}$$

This integral is solved in Appendix C.2.

5.5.2 Cross QAM Scheme

The exact conditional SER expression for XQAM-32 scheme is given as (1.12). On substituting (1.12) into (5.11) and applying Theorem 5.1, the closed-form ASER expression for XQAM-32 modulation scheme is evaluated as

$$\begin{aligned}P_s^{\text{XQAM-32}}(e) &= \frac{47}{32} - \frac{13}{8}\sqrt{\frac{2A\overline{\chi}_{sr}}{(2(1+\overline{\chi}_{sr}\Omega_{e_{sr}})+2A\overline{\chi}_{sr})}} - \frac{1}{16}\sqrt{\frac{4A\overline{\chi}_{sr}}{(2(1+\overline{\chi}_{sr}\Omega_{e_{sr}})+4A\overline{\chi}_{sr})}} \\ &+ \frac{23}{8\pi}\sqrt{\frac{\overline{\chi}_{sr}A}{((1+\overline{\chi}_{sr}\Omega_{e_{sr}})+\overline{\chi}_{sr}A)}}\tan^{-1}\left(\sqrt{\frac{((1+\overline{\chi}_{sr}\Omega_{e_{sr}})+\overline{\chi}_{sr}A)}{\overline{\chi}_{sr}A}}\right) \\ &- \frac{1}{\sqrt{\pi}}\sum_{i=1}^{N} w_i \exp\left(\frac{-(1+\overline{\chi}_{sr}\Omega_{e_{sr}})\overline{\chi}_{rd}\exp\left[2\sqrt{2}\,\sigma_{h_{rd}}y_i + 2\mu_{h_{rd}}\right]}{(1+\overline{\chi}_{rd}\Omega_{e_{rd}})\overline{\chi}_{sr}}\right) \\ &\times \Bigg[\frac{13}{4}Q\Big(\sqrt{\frac{2A\overline{\chi}_{rd}}{(1+\overline{\chi}_{rd}\Omega_{e_{rd}})}\exp\left[2\sqrt{2}\,\sigma_{h_{rd}}y_i + 2\mu_{h_{rd}}\right]}\Big) + \frac{1}{8}Q\Big(2\sqrt{\frac{A\overline{\chi}_{rd}}{(1+\overline{\chi}_{rd}\Omega_{e_{rd}})}\exp\left[2\sqrt{2}\,\sigma_{h_{rd}}y_i + 2\mu_{h_{rd}}\right]}\Big) \\ &- \frac{23}{8}Q^2\Big(\sqrt{\frac{2A\overline{\chi}_{rd}}{(1+\overline{\chi}_{rd}\Omega_{e_{rd}})}\exp\left[2\sqrt{2}\,\sigma_{h_{rd}}y_i + 2\mu_{h_{rd}}\right]}\Big)\Bigg] \\ &\times \left[\frac{2\sigma_{h_{rd}}\overline{\chi}_{rd}}{(1+\overline{\chi}_{rd}\Omega_{e_{rd}})}\exp\left[2\sqrt{2}\,\sigma_{h_{rd}}y_i + 2\mu_{h_{rd}}\right]\left(2y_i^2+1\right)^{-1/2} - 1\right].\end{aligned} \tag{5.18}$$

Obtaining (5.18) involves solving the following integral

$$\mathcal{I}_1 = \Big(\frac{1+\overline{\chi}_{sr}\Omega_{e_{sr}}}{\overline{\chi}_{sr}}\Big)\int_0^{\infty}\left[\frac{13}{4}Q(\sqrt{2A\chi}) + \frac{1}{8}Q(2\sqrt{A\chi}) - \frac{23}{8}Q^2(\sqrt{2A\chi})\right] \times \exp\left(\frac{-(1+\overline{\chi}_{sr}\Omega_{e_{sr}})\chi}{\overline{\chi}_{sr}}\right)d\chi. \tag{5.19}$$

This integral is solved in Appendix C.3.

5.5.3 Hexagonal QAM Scheme

The exact conditional SER expression for HQAM scheme is given as (1.13). On substituting (1.13) into (5.11) and applying Theorem 5.1, the generalized novel closed-form ASER expression of HQAM scheme for hybrid RF/NLOS UVC system is evaluated as

$$P_s^{\mathrm{HQAM}}(e) = \frac{D}{2} + \frac{1}{6} - \frac{D_C}{2} - \frac{D_C}{2}\sqrt{\frac{\overline{\chi}_{sr}q_1}{(2(1+\overline{\chi}_{sr}\Omega_{e_{sr}}) + \overline{\chi}_{sr}q_1}} - \frac{2}{3\pi}\sqrt{\frac{\overline{\chi}_{sr}q_1}{(3(1+\overline{\chi}_{sr}\Omega_{e_{sr}}) + \overline{\chi}_{sr}q_1)}}$$
$$\times \tan^{-1}\left(\sqrt{\frac{(3(1+\overline{\chi}_{sr}\Omega_{e_{sr}}) + \overline{\chi}_{sr}q_1)}{\overline{\chi}_{sr}q_1}}\right) + \frac{D_C}{\pi}\sqrt{\frac{\overline{\chi}_{sr}q_1}{(2(1+\overline{\chi}_{sr}\Omega_{e_{sr}}) + \overline{\chi}_{sr}q_1)}}$$
$$\times \tan^{-1}\left(\sqrt{\frac{\sqrt{3}(2(1+\overline{\chi}_{sr}\Omega_{e_{sr}}) + \overline{\chi}_{sr}q_1)}{\overline{\chi}_{sr}q_1}}\right) + \frac{D_C}{\pi}\sqrt{\frac{\overline{\chi}_{sr}q_1}{(6(1+\overline{\chi}_{sr}\Omega_{e_{sr}}) + \overline{\chi}_{sr}q_1)}}$$
$$\times \tan^{-1}\left(\sqrt{\frac{(6(1+\overline{\chi}_{sr}\Omega_{e_{sr}}) + \overline{\chi}_{sr}q_1)}{\sqrt{3}\overline{\chi}_{sr}q_1}}\right) - \frac{1}{\sqrt{\pi}}\sum_{i=1}^{N} w_i \exp\left(\frac{-(1+\overline{\chi}_{sr}\Omega_{e_{sr}})\overline{\chi}_{rd}\exp\left[2\sqrt{2}\,\sigma_{h_{rd}}y_i + 2\mu_{h_{rd}}\right]}{(1+\overline{\chi}_{rd}\Omega_{e_{rd}})\overline{\chi}_{sr}}\right)$$
$$\times \Bigg[D_C Q\Big(\sqrt{\frac{q_1\overline{\chi}_{rd}}{(1+\overline{\chi}_{rd}\Omega_{e_{rd}})}\exp\left[2\sqrt{2}\,\sigma_{h_{rd}}y_i + 2\mu_{h_{rd}}\right]}\Big) + \frac{2}{3}D_C Q^2\Big(\sqrt{\frac{2q_1\overline{\chi}_{rd}}{3(1+\overline{\chi}_{rd}\Omega_{e_{rd}})}\exp\left[2\sqrt{2}\,\sigma_{h_{rd}}y_i + 2\mu_{h_{rd}}\right]}\Big)$$
$$- 2D_C Q\Big(\sqrt{\frac{q_1\overline{\chi}_{rd}}{(1+\overline{\chi}_{rd}\Omega_{e_{rd}})}\exp\left[2\sqrt{2}\,\sigma_{h_{rd}}y_i + 2\mu_{h_{rd}}\right]}\Big)Q\Big(\sqrt{\frac{q_1\overline{\chi}_{rd}}{3(1+\overline{\chi}_{rd}\Omega_{e_{rd}})}\exp\left[2\sqrt{2}\,\sigma_{h_{rd}}y_i + 2\mu_{h_{rd}}\right]}\Big)\Bigg]$$
$$\times \left[\frac{2\sigma_{h_{rd}}\overline{\chi}_{rd}}{(1+\overline{\chi}_{rd}\Omega_{e_{rd}})}\exp\left[2\sqrt{2}\,\sigma_{h_{rd}}y_i + 2\mu_{h_{rd}}\right]\left(2y_i^2+1\right)^{-1/2} - 1\right]. \tag{5.20}$$

Obtaining (5.20) involves solving the following integral

$$\mathcal{I}_1 = \Big(\frac{1+\overline{\chi}_{sr}\Omega_{e_{sr}}}{\overline{\chi}_{sr}}\Big)\int_0^\infty \left[D_C Q(\sqrt{q_1\chi}) + \frac{2}{3}D_C Q^2(\sqrt{2q_1\chi/3}) - 2D_C Q(\sqrt{q_1\chi})Q(\sqrt{q_1\chi/3})\right]$$
$$\times \exp\left(\frac{-(1+\overline{\chi}_{sr}\Omega_{e_{sr}})\chi}{\overline{\chi}_{sr}}\right)d\chi. \tag{5.21}$$

This integral is solved in Appendix C.4.

5.6 Numerical and Simulation Results

In this section, the performance of the proposed hybrid RF/NLOS UVC system is investigated and the accuracy of derived analytical expressions is confirmed using Monte-Carlo simulations. The system and channel configuration parameters of the NLOS UVC link are considered as $\lambda = 260$ nm, $C_n^2 = 5\times 10^{-15}\mathrm{m}^{-2/3}$, $\theta_{rd}^{Tx} = \theta_{rd}^{Rx} = 50°$, $L_{rd} = 500$ m [12]. Under these conditions, the scintillation index of the RD link is evaluated as 0.2830, which conforms to the weak turbulence conditions of NLOS UVC as stated in Section 5.2. Unless otherwise stated, it is considered that $\rho = \rho_{sr} = \rho_{rd}$. Without loss of generality and for simplicity, it is considered that $\chi_{th} = 3$ dB, and $\overline{\chi}_{sr} = \overline{\chi}_{rd} = \chi_\circ$ [71]. The performance of the system is evaluated in terms of outage probability and ASER for both perfect CSI case $\rho = \infty$, and imperfect CSI cases.

Fig. 5.2a show the analytical and simulation plots of the outage probability versus the average SNR for $\rho = (0.01, 0.1, 1, 10, \infty)$. Firstly, it can be observed that the analytical curves coincide with the simulation curves, thus confirming the accuracy of the derived analytical expression of outage probability. Further, it can be observed that imperfection in the channel estimate significantly degrades the system's outage performance. As an example, to achieve the outage probability of 10^{-4}, additional SNRs of around 20 dB, 19.6 dB, 17 dB, and 9.6 dB are required for $\rho = 0.01, 0.1, 1, 10$, respectively, when compared to perfect CSI case. This observation follows our intuition since a lower value of correlation coefficient ρ signifies poor channel estimate, leading to a higher value of CEE variance (Ω_{e_j}). An increase in Ω_{e_j} (with decreasing ρ) reduces the received instantaneous SNR of the system at Rx, thereby resulting in degraded system performance.

In Fig. 5.2b, effect of different CEEs in SR and RD links on the system's outage probability is evaluated. It is observed that for lower SNR values, the channel estimation quality of both SR and RD links have a significant impact on the system performance. However, in the case of high SNRs, the SR link is more vulnerable to CEE as compared to the RD link. This observation is very important from the system designer's perspective and suggests that a more sophisticated channel estimation technique [78, 94] should be employed at R to minimize CEE for the RF link, irrespective of the SNR. However, for high SNR regimes, the CEE of the NLOS UV link does not affect the system performance much, and hence, the signal processing at D can be switched to less complex circuitry irrespective of the value of ρ_{sr}.

Fig. 5.3 depicts the effect of elevation angles ($\theta' = \theta_{RD}^{Tx} = \theta_{RD}^{Rx}$) on the system performance for $\chi_{th} = 3$ dB, $\chi_\circ = 40$ dB, and different values of ρ. It can be seen that irrespective of the amount of CEE present, the system performs invariably better for $\theta' \leq 70°$. On the other hand, for elevation angle greater than 70°, the performance degrades drastically. This happens due to larger link distance from S to CV, and from CV to D for higher values of elevation angle, thereby increasing the turbulence strength in NLOS UVC link.

The diversity order of the considered system is illustrated in Fig. 5.4 for different ρ values. It is inferred that, regardless of the value of ρ, the system's diversity order attains the maximum value 1, for large SNR. This is owing to the fact that each of the

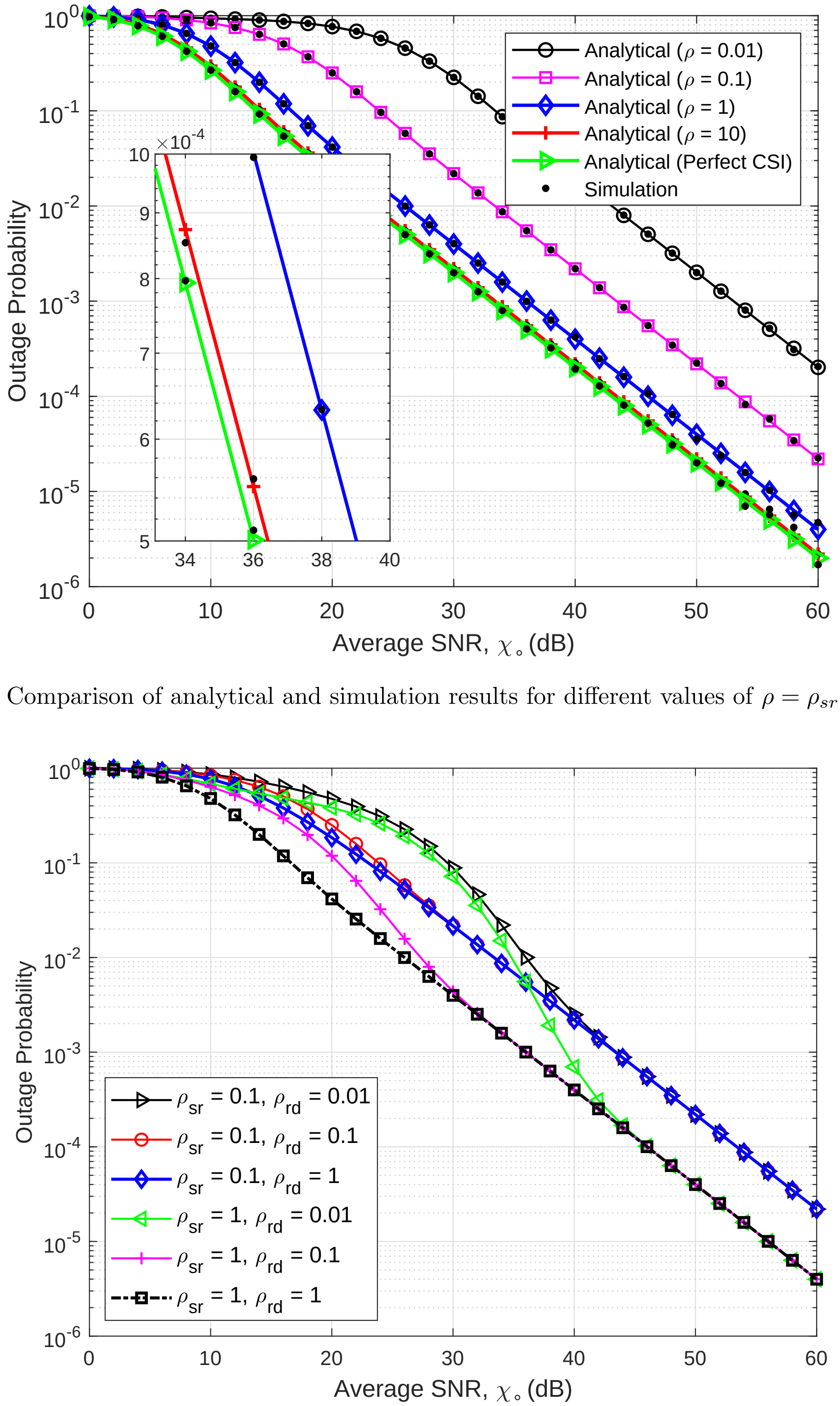

(a) Comparison of analytical and simulation results for different values of $\rho = \rho_{sr} = \rho_{rd}$.

(b) Analytical results for $\rho_{sr} = (0.1, 0.01)$, and $\rho_{rd} = (0.01, 0.1, 1)$.

Figure 5.2: Outage probability versus average SNR ($\chi_\circ$) for $\chi_{th} = 3$ dB.

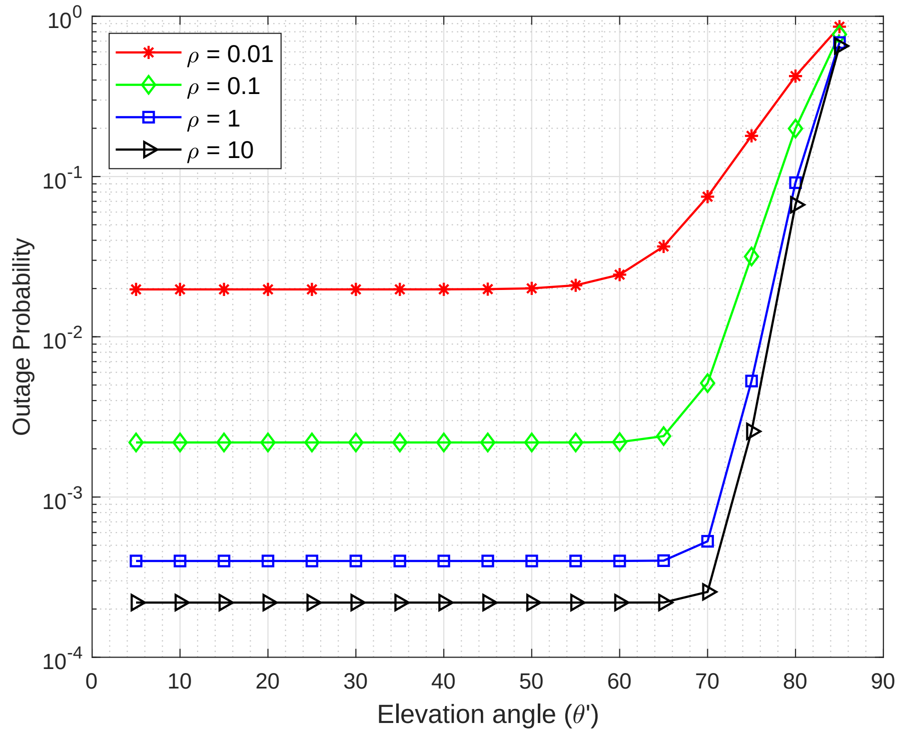

Figure 5.3: Analytical results of outage probability versus θ' for $\chi_{th} = 3$ dB.

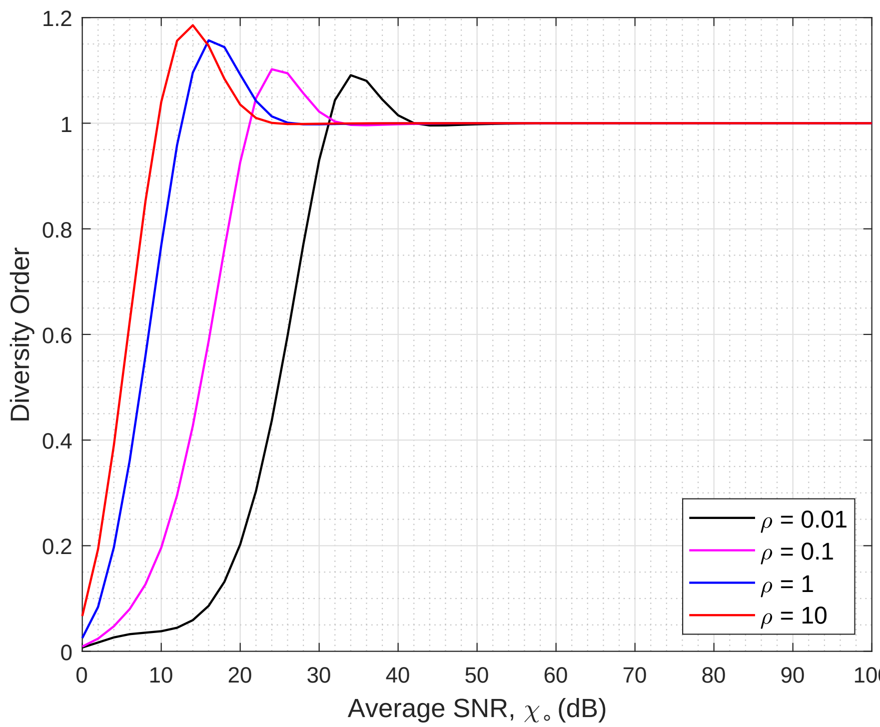

Figure 5.4: Diversity order versus $\chi_\circ$ for $\chi_{th} = 3$ dB, and $\rho = (0.01, 0.1, 1, 10)$.

SR and RD links has just one communication channel. As a result, at high SNR levels, the considered system does not provide any diversity gain. Further, it is observed that, the rate of convergence of the diversity order to it's final value reduces with the increase in CEE.

Fig. 5.5 demonstrates the ASER performance of the considered system for different QAM schemes through analytical and simulation plots. Here also, the analytical and simulation curves overlap for both perfect CSI ($\rho = 0$), and imperfect CSI ($\rho = \infty$) cases, thus validating the derived analytical expression of ASER. In Fig. 5.5(a), the ASER results for 16-points constellation size and $\rho = (0.1, \infty)$ are presented. It is observed that imperfection in the channel estimation significantly degrades the ASER performance of the system. For instance, to maintain an ASER of 10^{-4} with $\rho = 0.1$, an additional SNRs of 10.25 dB is required for all modulation schemes when compared to perfect CSI case. Further, it can be seen that SQAM-16 performs better than RQAM-8 $\times$ 2, irrespective of the amount of CEE present. This is because, for a given energy, SQAM maximizes the minimum distance among its constellation points as opposed to the RQAM scheme.

Fig. 5.5(b) depicts the ASER performance of 32-points RQAM, XQAM and HQAM schemes for perfect CSI case. It is observed that, for a target ASER of 10^{-4}, HQAM-32 outperforms RQAM-16 $\times$ 2, RQAM-8 $\times$ 4, and XQAM-32 with an SNR gain of 6.01 dB, 1.2 db, and 0.08 dB, respectively. Fig. 5.5(c) shows comparative performance of different modulation schemes for 64-points constellation, and $\rho = \infty$. It is observed that SQAM-64 provides a significant SNR gain of 7.65 dB, 3.19 dB, when compared to RQAM-16 $\times$ 4, and RQAM-32 $\times$ 2 for an ASER of 10^{-4}. Further, it is observed that HQAM-64 shows an SNR improvement of 0.26 dB (approx.) over SQAM-64. The optimum performance of HQAM is due to the densest packing of its constellation points as compared to other modulation formats.

In Fig. 5.5(d), ASER curves for different modulation formats are plotted for imperfect CSI with $\rho = 0.1$. It can be seen that the HQAM always outperforms other modulation schemes for a constellation size of 8 or more. For example, HQAM-64, HQAM-32, HQAM-16, and HQAM-8, provides an SNR gain of 0.26 dB, 0.08 dB, 0.24 dB, and 0.94 dB, respectively, over SQAM-64, XQAM-32, SQAM-16, and RQAM-4 $\times$ 2 to achieve an ASER of 10^{-3}. The better performance of HQAM is attributed to the optimum Euclidean

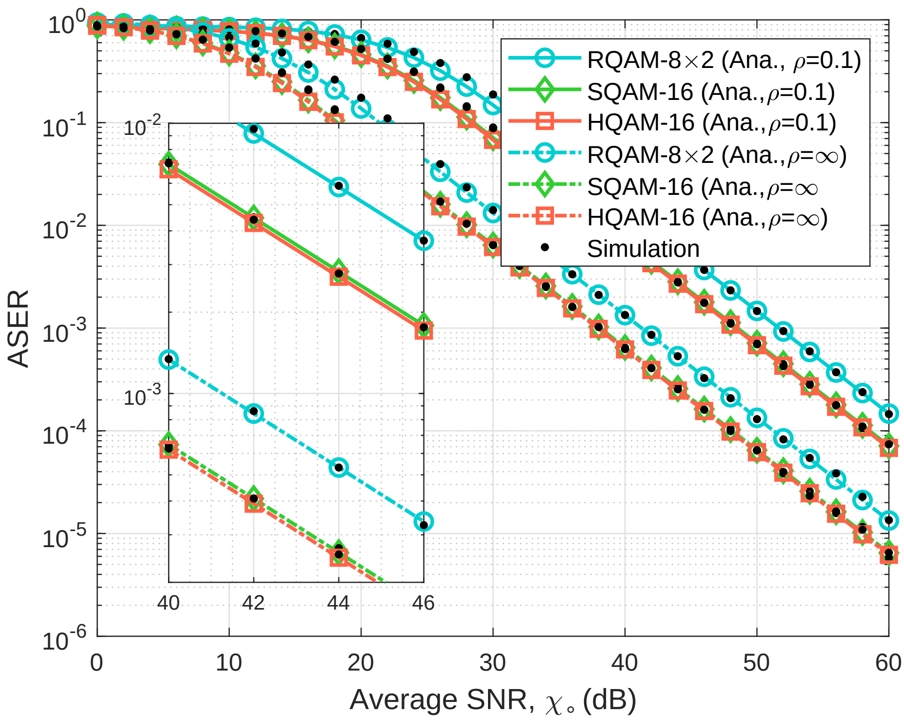

(a) 16-points constellation, $\rho = (0.1, \infty)$

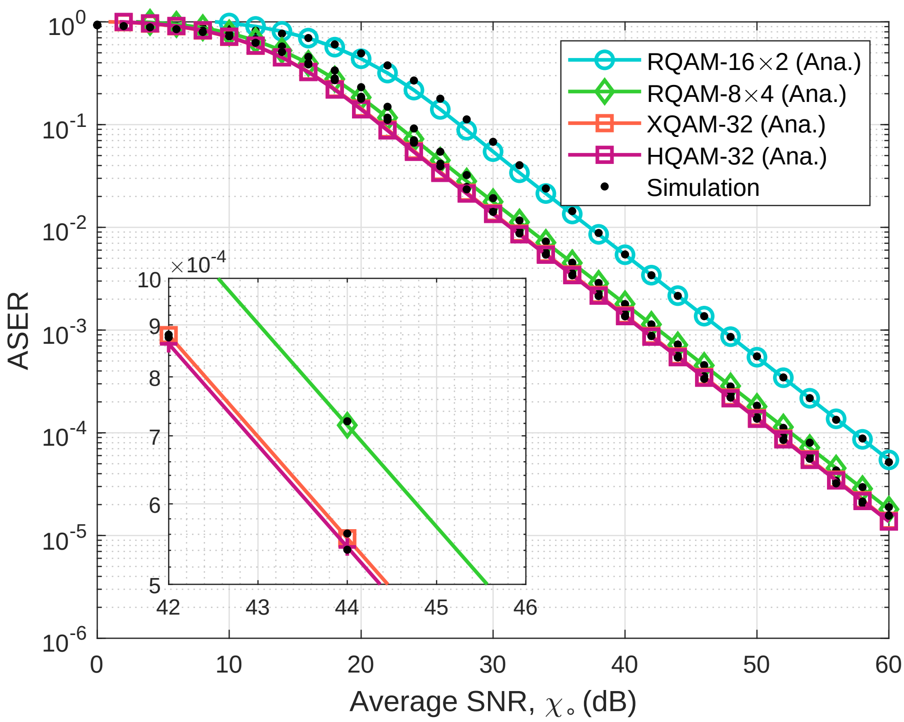

(b) 32-points constellation, $\rho = \infty$

Figure 5.5: ASER versus $\chi_\circ$ for various QAM modulation schemes.

distance of its 2D hexagonal lattice. For the constellation size of 4, SQAM performs marginally better than HQAM. This is due to a larger number of nearest neighborhoods

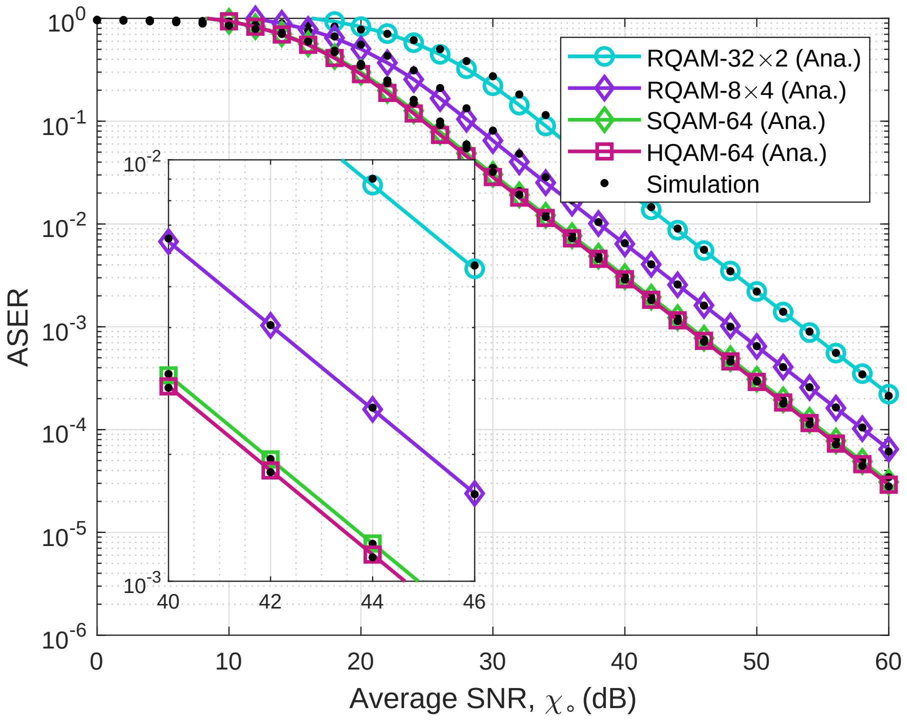

(c) 64-points constellation, $\rho = \infty$

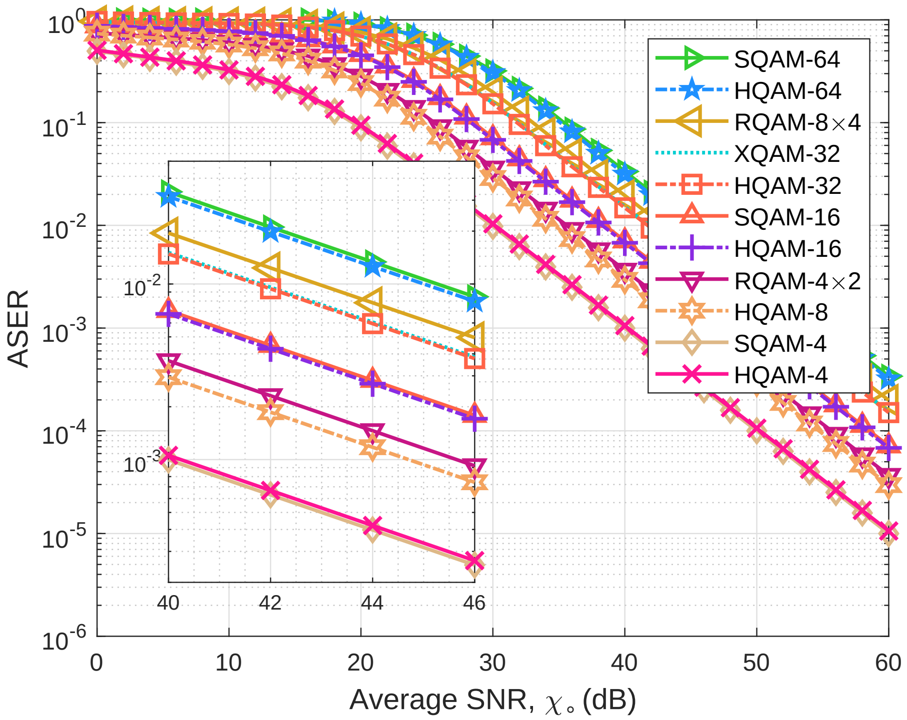

(d) $(4, 8, 16, 32, 64)$-points constellations and $\rho = 0.1$.

Figure 5.5: ASER versus $\chi_\circ$ for various QAM modulation schemes (contd.).

in HQAM-4 than SQAM-4.

5.7 Summary

The performance of a novel dual-hop RF/NLOS UVC DF cooperative communication system is investigated in terms of outage probability and ASER. Imperfect CSI at considered at the Rx and its impact on the system performance is evaluated. It is demonstrated that the system performance significantly degrades as the imperfection in the channel estimate increases. Further, it is shown that the RF link is more prone to CEE than the UV link, specifically for high SNR scenarios, hence there is a need for better estimators in RF link. Furthermore, it is shown that the system performs best for elevation angle of less than 70° in NLOS link. We considered RQAM, SQAM, XQAM, and HQAM schemes for ASER analysis and showed that for all constellation sizes, SQAM performs better than RQAM. Furthermore, it is demonstrated that HQAM is an optimal scheme for constellation size greater than 4. For instance, it is shown that for a constellation size of 64, HQAM provides a significant SNR gain of 0.26 dB (approx.) over SQAM-64 to achieve the ASER of 10^{-4} for perfect CSI case.

Chapter 6

Conclusions and Future Works

6.1 Conclusions

In this thesis, the problem of high-path loss, turbulence induced fading, and low data rate of UVC system is addressed through the use of spatial diversity, cooperative relaying, and higher-order modulation schemes, respectively. Table 6.1 shows the summary of different system models considered in the thesis.

Table 6.1: Summary of the system models studied.

Chapter	**System Model**	**Fading Model**	**Channel Imperfections**	**Performance Metrics**
Chapter 2	Receiver Diversity with Correlated Branches	Lognormal Distribution	Not considered	Outage Probability ASER Ergodic Capacity
Chapter 3	Multiple parallel relays	Lognormal Distribution	Not considered	Outage Probability Diversity order ASER
Chapter 4	Best relay selection	Lognormal Distribution	Considered	Outage Probability Diversity order ASER
Chapter 5	Hybrid RF/NLOS-UVC	Rayleigh Distribution for RF link, Lognormal Distribution for UV link	Considered	Outage Probability Diversity order ASER

The performance analysis of the proposed systems is carried out using the performance metrics like outage probability, ASER, diversity order, and ergodic capacity. In the analysis, the practical constraint of imperfect CSI at Rx is considered, and its impact on the system performance is evaluated.

Initially, the performance of the SIMO NLOS UVC system under weak turbulence conditions is investigated by considering channel correlation. For higher order modulation schemes, the ASER performance of the system is analyzed. It is observed that SQAM outperforms RQAM across all constellation sizes and channel correlations. Further, it is shown that HQAM outperforms SQAM and XQAM for constellation sizes greater than 4. It is observed that performance degrades as channel correlation increases due to the loss of diversity. Furthermore, it is demonstrated that for high channel correlation, increasing the number of branches beyond a certain value has a negligible effect on the system's performance. The ergodic capacity of the system is calculated, and it is demonstrated that when the refractive index structure coefficient is small, channel correlation has a marginal effect on the ergodic capacity.

Next, a cooperative multi-relay communication system is proposed. The system's performance is evaluated using both variable-gain and fixed-gain AF relaying. It is demonstrated that the use of parallel relays in conjunction with SC leads in a considerable performance gain over the no-relay case. Additionally, it is proved that the system's performance improves with an increase in the number of relays, decreased elevation angles, and increased FOV. It is concluded that fixed-gain relaying always outperforms variable-gain AF relaying due to its high amplification. Further, the diversity analysis is performed and it is shown that the system's diversity order improves with the addition of more relays. Furthermore, it has been found that HQAM provides significant performance advantages for UVC long-distance cooperative communication when compared to RQAM and XQAM schemes.

Further, a DF based cooperative relay NLOS UVC system employing best relay selection, and SC at the receiver is examined. The realistic case of imperfect CSI is considered and the system's performance is analyzed in terms of outage probability, diversity order, and ASER. It is noticed that while the number of relays is fixed, the system's diversity order improves with decreasing elevation angles at relay nodes. It is shown that lowering the relay's elevation angle and increasing the Rx FOV considerably enhances the system's performance. It is observed that the impact of imperfect CSI grows more severe as the intensity of the turbulence increases, requiring a greater SNR to reach the desired system's performance goals. Additionally, it is proved that HQAM outperforms RQAM, SQAM, and XQAM schemes irrespective of the number of relays, and CEE.

Finally, a hybrid RF/NLOS UVC system is proposed, in which the RF link is modelled using Rayleigh distribution and the UVC link is modelled using LN distribution. The system's performance is examined in depth for higher-order modulation schemes considering imperfect CSI at the receiver. Additionally, the effect of elevation angles on overall e2e system performance is analyzed, and it is demonstrated that maintaining an elevation angle of less than 70° leads in improved performance. Further, it is established that the RF link is more susceptible to CEE and a more advanced channel estimate technique is required for the RF link. Furthermore, it is shown that for the considered RF/NLOS UVC system, HQAM outperforms all other modulation schemes for constellation size greater than four.

As a concluding remark, this dissertation addresses the primary challenges associated with NLOS UVC technology by employing diversity techniques, cooperative relaying, and hybrid arrangements, thereby making it a more viable candidate for adoption in future generation wireless communication networks such as 6G. Throughout the dissertation, it has been demonstrated that futuristic higher-order modulation schemes, such as XQAM and HQAM, can play a significant role in supporting high-data applications, regardless of the underlying system model. In addition, the significance of system configuration parameters such as elevation angle and FOV is illustrated, and it is proved that judicious selection of these parameters can result in a significant performance gains. It is deduced that regardless of the system model considered, a lower elevation angle and a larger FOV always lead to enhanced performance. Further, the detrimental effects of channel estimation errors on system performance are demonstrated, thereby highlighting the need for sophisticated and robust channel estimation techniques at the receiver.

It is also worth mentioning the limitations of the work carried out in the dissertation. First and foremost, the research outcomes are only applicable when the geometry of the transmitter and receiver are coplanar. Another limitation is that the maximum distance for UV link is considered to be less than one kilometre, for which the turbulence is considered to be weak to moderate. The results obtained are inapplicable for UV link distances exceeding 1 kilometre. For such distances, turbulence is intense, and a different fading model (such as Gamma-Gamma) is more suitable. The current approach assumes a single scattering path from source to destination, which is the third limitation. The results of this study do not hold true for multiple scattering, which involves many scattering events before a UV photon reaches the receiver. The search for analytical path-loss expressions and turbulence modelling for the multiple-scattering UVC is still underway. The research work carried out in this dissertation can be expanded in the future to address these limitations in order to gain greater technical depth and understanding of the NLOS UVC system.

6.2 Future Works

- The work covered in this thesis considers the single scattering model of UVC, in which the photons undergo scattering at most once. The similar study can be conducted for multiple scattering models in which photons undergo scattering more than once. Such a study is more crucial for long-distance outdoor UV communication since multiple UV photon scattering is more likely in such a scenario, making it more intriguing to examine the effects of multiple scattering on the UVC system's performance.

- The work of this thesis can also be extended for strong turbulence scenarios, in which the irradiance fluctuations due to turbulence is modelled by a Gamma-Gamma distribution. Strong turbulence is predicted to cause UVC to perform worse than in the weak turbulence situation, necessitating the use of more sophisticated system models and approaches in NLOS UVC to improve performance. In the presence of strong turbulence, UVC is expected to underperform the weak turbulence case thereby motivating the need to consider more advanced system models and techniques in NLOS UVC to boost it's performance.

- In the current study SC is employed as the diversity combining approach at the Rx to reduce receiver complexity. Due to the low power budget of UVC, it is worthwhile to investigate other combining techniques, such as EGC and MRC, in order to determine the power gain over SC.

- Impact of co-channel interference along with outdated channels estimation can be focused for the considered system models.
- The effect of non-linearity in the UV LEDs can be incorporated in the considered cooperative relayed NLOS UVC systems. The effective receiver equalization techniques can be studied to mitigate the distortion due to LED non-linearity.
- The hybrid combination of NLOS UVC with other OWC technologies such as FSO and VLC can also be explored.

Appendix A

Proofs for Chapter 3

A.1 Proof of Lemma 3.1

$$\mathbb{E}[g(\chi_{e2e}^{ub})] = \int_0^{\infty} g(\chi) f_{\chi_{e2e}^{ub}}(\chi) d\chi. \tag{A.1}$$

On substituting $f_{\chi_{e2e}^{ub}}(\chi)$ from (3.22) into (A.1), and after mathematical simplifications, we get

$$\mathbb{E}[g(\chi_{e2e}^{ub})] = \Xi_2 + \Xi_2, \tag{A.2}$$

where

$$\Xi_1 = M \int_{-\infty}^{\infty} g(\exp\Big(\sqrt{2}\sigma_{sr}x + \mu_{sr}\Big) Q\left(\frac{\sqrt{2}\sigma_{sr}x + \mu_{sr} - \mu_{rd}}{\sigma_{rd}}\right)$$
$$\left[1 - Q\Big(\sqrt{2}\sigma_{sr}x\Big) Q\left(\frac{\sqrt{2}\sigma_{sr}x + \mu_{sr} - \mu_{rd}}{\sigma_{rd}}\right)\right]^{M-1} e^{-x^2} dx, \tag{A.3}$$

and

$$\Xi_2 = M \int_{-\infty}^{\infty} g(\exp\Big(\sqrt{2}\sigma_{rd}y + \mu_{rd}\Big) Q\left(\frac{\sqrt{2}\sigma_{rd}y + \mu_{rd} - \mu_{sr}}{\sigma_{sr}}\right)$$
$$\left[1 - Q\Big(\sqrt{2}\sigma_{rd}y\Big) Q\left(\frac{\sqrt{2}\sigma_{rd}y + \mu_{rd} - \mu_{sr}}{\sigma_{sr}}\right)\right]^{M-1} e^{-y^2} dy, \tag{A.4}$$

The expressions in (A.3) and (A.4) matches Gauss-Hermite quadrature integral form

$\int_{-\infty}^{\infty} f(\xi)e^{-\xi^2}d\xi$ which can be evaluated using the numerical integration technique [63, Table 25.10] resulting in (3.24) and (3.25).

Appendix B

Proofs for Chapter 4

B.1 Proof of Theorem 4.1

$$\mathbb{E}[g(\chi_{e2e})] = \int_0^\infty g(\chi) f_{\chi_{e2e}}(\chi) d\chi. \tag{B.1}$$

On substituting $f_{\chi_{e2e}}(\chi)$ from (4.11) into (B.1) we get

$$\mathbb{E}[g(\chi_{e2e})] = \mathcal{X}_1 + \mathcal{X}_2, \tag{B.2}$$

where

$$\begin{aligned}
\mathcal{X}_1 = &\frac{N_r}{\sqrt{2\pi}\, 2\sigma_{h_{SR}}\chi} \int_0^\infty g(\chi) Q\Big(\frac{\ln(\chi) - 2\mu_{h_{RD}} + \ln\big(4\epsilon_{RD} + 4\sigma^2_{e,RD}\big)}{2\sigma_{h_{RD}}}\Big) \\
&\times \left[1 - Q\Big(\frac{\ln(\chi) - 2\mu_{h_{RD}} + \ln\big(4\epsilon_{RD} + 4\sigma^2_{e,RD}\big)}{2\sigma_{h_{RD}}}\Big) Q\Big(\frac{\ln(\chi) - 2\mu_{h_{SR}} + \ln\big(4\epsilon_{SR} + 4\sigma^2_{e,SR}\big)}{2\sigma_{h_{SR}}}\Big)\right]^{N_r-1} \\
&\times \exp\left(\frac{-\big(\ln(\chi) - 2\mu_{h_{SR}} + \ln\big(4\epsilon_{SR} + 4\sigma^2_{e,SR}\big)\big)^2}{8\sigma^2_{h_{SR}}}\right) d\chi,
\end{aligned} \tag{B.3}$$

and

$$\begin{aligned}
\mathcal{X}_2 = &\frac{N_r}{\sqrt{2\pi}\, 2\sigma_{h_{RD}}\chi} \int_0^\infty g(\chi) Q\Big(\frac{\ln(\chi) - 2\mu_{h_{SR}} + \ln\big(4\epsilon_{SR} + 4\sigma^2_{e,SR}\big)}{2\sigma_{h_{SR}}}\Big) \\
&\times \left[1 - Q\Big(\frac{\ln(\chi) - 2\mu_{h_{SR}} + \ln\big(4\epsilon_{SR} + 4\sigma^2_{e,SR}\big)}{2\sigma_{h_{SR}}}\Big) Q\Big(\frac{\ln(\chi) - 2\mu_{h_{RD}} + \ln\big(4\epsilon_{RD} + 4\sigma^2_{e,RD}\big)}{2\sigma_{h_{RD}}}\Big)\right]^{N_r-1} \\
&\times \exp\left(\frac{-\big(\ln(\chi) - 2\mu_{h_{RD}} + \ln\big(4\epsilon_{RD} + 4\sigma^2_{e,RD}\big)\big)^2}{8\sigma^2_{h_{RD}}}\right) d\chi.
\end{aligned} \tag{B.4}$$

On performing change of variable $\xi = \big[\ln(\chi) - 2\mu_{h_{SR}} + \ln\Big(4\epsilon_{SR} + 4\sigma^2_{e,SR}\Big)\big]/2\sqrt{2}\,\sigma_{h_{SR}}$ and $\xi = \big[\ln(\chi) - 2\mu_{h_{RD}} + \ln\Big(4\epsilon_{RD} + 4\sigma^2_{e,RD}\Big)\big]/2\sqrt{2}\,\sigma_{h_{RD}}$ in (B.3) and (B.4), respectively, and after simplification, we get (B.5) and (B.6) given as

$$\begin{aligned}
\mathcal{X}_1 = \frac{N_r}{\sqrt{\pi}} \int_0^\infty & g\Bigg(\exp\left(2\sqrt{2}\sigma_{h_{SR}}\xi + 2\mu_{h_{SR}} - \ln\left(4\epsilon_{SR} + 4\sigma^2_{e,SR}\right)\right)\Bigg) \\
& \times Q\Bigg(\frac{2\sqrt{2}\sigma_{h_{SR}}\xi + 2\mu_{h_{SR}} - \ln\Big(4\epsilon_{SR} + 4\sigma^2_{e,SR}\Big) - 2\mu_{h_{RD}} + \ln\Big(4\epsilon_{RD} + 4\sigma^2_{e,RD}\Big)}{2\sigma_{h_{RD}}}\Bigg)\Bigg[1 - Q\big(\sqrt{2}\xi\big) \\
& \times Q\Bigg(\frac{2\sqrt{2}\sigma_{h_{SR}}\xi + 2\mu_{h_{SR}} - \ln\Big(4\epsilon_{SR} + 4\sigma^2_{e,SR}\Big) - 2\mu_{h_{RD}} + \ln\Big(4\epsilon_{RD} + 4\sigma^2_{e,RD}\Big)}{2\sigma_{h_{RD}}}\Bigg)\Bigg]^{N_r-1} \\
& \times \exp\big(-\xi^2\big)d\xi.
\end{aligned} \tag{B.5}$$

$$\begin{aligned}
\mathcal{X}_2 = \frac{N_r}{\sqrt{\pi}} \int_0^\infty & g\Bigg(\exp\left(2\sqrt{2}\sigma_{h_{RD}}\xi + 2\mu_{h_{RD}} - \ln\left(4\epsilon_{RD} + 4\sigma^2_{e,RD}\right)\right)\Bigg) \\
& \times Q\Bigg(\frac{2\sqrt{2}\sigma_{h_{RD}}\xi + 2\mu_{h_{RD}} - \ln\Big(4\epsilon_{RD} + 4\sigma^2_{e,RD}\Big) - 2\mu_{h_{SR}} + \ln\Big(4\epsilon_{SR} + 4\sigma^2_{e,SR}\Big)}{2\sigma_{h_{SR}}}\Bigg)\Bigg[1 - Q\big(\sqrt{2}\xi\big) \\
& \times Q\Bigg(\frac{2\sqrt{2}\sigma_{h_{RD}}\xi + 2\mu_{h_{RD}} - \ln\Big(4\epsilon_{RD} + 4\sigma^2_{e,RD}\Big) - 2\mu_{h_{SR}} + \ln\Big(4\epsilon_{SR} + 4\sigma^2_{e,SR}\Big)}{2\sigma_{h_{SR}}}\Bigg)\Bigg]^{N_r-1} \\
& \times \exp\big(-\xi^2\big)d\xi.
\end{aligned} \tag{B.6}$$

Solving (B.5) and (B.6) using Gauss-Hermite quadrature integration technique [63, Table 25.10], and substituting the resulting expressions into (B.2) produces (4.12).

B.2 Proof of Theorem 4.2

In high SNR regime, on substituting the value of $\epsilon_p,\ p \in \{SD, SR, RD\}$ into (4.10) and (4.14), and rearranging the terms, we get

$$\begin{aligned}
P^{e2e}_{out} \approx \Bigg[& Q\Bigg(\frac{-\ln(\chi) + 2\mu_{h_{SR}} - \ln\big(4\ell^{-2}_{SR}\big) + \ln(\chi_\circ)}{2\sigma_{h_{SR}}}\Bigg) + Q\Bigg(\frac{-\ln(\chi) + 2\mu_{h_{RD}} - \ln\big(4\ell^{-2}_{RD}\big) + \ln(\chi_\circ)}{2\sigma_{h_{RD}}}\Bigg) \\
& - Q\Bigg(\frac{-\ln(\chi) + 2\mu_{h_{SR}} - \ln\big(4\ell^{-2}_{SR}\big) + \ln(\chi_\circ)}{2\sigma_{h_{SR}}}\Bigg) Q\Bigg(\frac{-\ln(\chi) + 2\mu_{h_{RD}} - \ln\big(4\ell^{-2}_{RD}\big) + \ln(\chi_\circ)}{2\sigma_{h_{RD}}}\Bigg)\Bigg]^{N_r},
\end{aligned} \tag{B.7}$$

and

$$P_{out}^{SD} \approx Q\Big(\frac{-\ln(\chi) + 2\mu_{h_{SD}} - \ln\big(4\ell_{SD}^{-2}\big) + \ln(\chi_\circ)}{2\sigma_{h_{SD}}}\Big). \tag{B.8}$$

In (B.7), the term involving product of two $Q(\cdot)$ functions is negligibly small as compared to other terms, and can safely be ignored for analytical tractability, resulting in

$$P_{out}^{e2e} \approx \left[Q\Big(\frac{-\ln(\chi) + 2\mu_{h_{SR}} - \ln\big(4\ell_{SR}^{-2}\big) + \ln(\chi_\circ)}{2\sigma_{h_{SR}}}\Big) + Q\Big(\frac{-\ln(\chi) + 2\mu_{h_{RD}} - \ln\big(4\ell_{RD}^{-2}\big) + \ln(\chi_\circ)}{2\sigma_{h_{RD}}}\Big)\right]^{N_r}. \tag{B.9}$$

On rearranging the terms in (B.8) and (B.9), and differentiating $\ln\big(P_{out}^{e2e}\big)$ and $\ln\big(P_{out}^{SD}\big)$ with respect to $\ln(\chi_\circ)$, we get

$$\frac{\partial \ln P_{out}^{e2e}}{\partial \ln \chi_\circ} \approx \frac{N_r\left[\frac{1}{2\sigma_{h_{SR}}}\exp\left(\frac{-(\ln(\chi_\circ)-\ln\left(4\ell_{SR}^{-2}\chi\right)+2\mu_{h_{SR}})^2}{8\sigma_{h_{SD}}^2}\right) + \frac{1}{2\sigma_{h_{RD}}}\exp\left(\frac{-(\ln(\chi_\circ)-\ln\left(4\ell_{RD}^{-2}\chi\right)+2\mu_{h_{RD}})^2}{8\sigma_{h_{RD}}^2}\right)\right]}{\sqrt{2\pi}\left[Q\left(\frac{\ln(\chi_\circ)-\ln\left(4\ell_{SR}^{-2}\chi\right)+2\mu_{h_{SR}}}{2\sigma_{h_{SR}}}\right) + Q\left(\frac{\ln(\chi_\circ)-\ln\left(4\ell_{RD}^{-2}\chi\right)+2\mu_{h_{RD}}}{2\sigma_{h_{RD}}}\right)\right]}, \tag{B.10}$$

and

$$\frac{\partial \ln P_{out}^{SD}}{\partial \ln \chi_\circ} = \frac{\exp\left(\frac{-(\ln(\chi_\circ)-\ln\left(4\ell_{SD}^{-2}\chi\right)+2\mu_{h_{SD}})^2}{8\sigma_{h_{SD}}^2}\right)}{2\sqrt{2\pi}\sigma_{h_{SD}}Q\left(\frac{\ln(\chi_\circ)-\ln\left(4\ell_{SD}^{-2}\chi\right)+2\mu_{h_{SD}}}{2\sigma_{h_{SD}}}\right)}, \tag{B.11}$$

respectively. On substituting (B.10) and (B.11) into (4.13) and simplifying, we get the RDO expression given in (4.15).

B.3 Proof of Theorem 4.3

The well known upper and lower bounds of Q function are given by [75]

$$\frac{z}{(1+z^2)\sqrt{2\pi}}\exp\big(-z^2/2\big) < Q(z) < \frac{1}{z\sqrt{2\pi}}\exp\big(-z^2/2\big). \tag{B.12}$$

Using these bounds into (4.15), and applying squeezing theorem [95] at high SNR, results in

$$\text{ARDO} \approx \lim_{\chi_\circ \to \infty} \frac{\frac{\sigma^2_{h_{SD}} N_r}{\sigma_{h_{SR}}} \exp\left(\frac{-(\ln \chi_\circ)^2}{8\sigma^2_{h_{SR}}}\right)}{\sigma_{h_{SR}} \exp\left(\frac{-(\ln \chi_\circ)^2}{8\sigma^2_{h_{SR}}}\right) + \sigma_{h_{RD}} \exp\left(\frac{-(\ln \chi_\circ)^2}{8\sigma^2_{h_{RD}}}\right)} + \frac{\frac{\sigma^2_{h_{SD}} N_r}{\sigma_{h_{RD}}} \exp\left(\frac{-(\ln \chi_\circ)^2}{8\sigma^2_{h_{RD}}}\right)}{\sigma_{h_{SR}} \exp\left(\frac{-(\ln \chi_\circ)^2}{8\sigma^2_{h_{SR}}}\right) + \sigma_{h_{RD}} \exp\left(\frac{-(\ln \chi_\circ)^2}{8\sigma^2_{h_{RD}}}\right)}. \tag{B.13}$$

Using $e^{-x} = \sum_{i=0}^{\infty} \frac{(-x)^i}{i!}$ in (B.13) and neglecting higher-order terms. After simplification, we obtain the ARDO expression as given in (4.17).

Appendix C

Proofs for Chapter 5

C.1 Proof of Theorem 5.1

$$\mathbb{E}[\Psi(\chi_{e2e})] = \int_0^\infty \Psi(\chi) f_{\chi_{e2e}}(\chi) d\chi. \tag{C.1}$$

On substituting (5.12) in (C.1) we get

$$\begin{aligned}\mathbb{E}[\Psi(\chi_{e2e})] = \int_0^\infty \Psi(\chi) \Bigg[& \left(\frac{1+\overline{\chi}_{sr}\Omega_{e_{sr}}}{\overline{\chi}_{sr}}\right) \exp\left(\frac{-(1+\overline{\chi}_{sr}\Omega_{e_{sr}})\chi}{\overline{\chi}_{sr}}\right) \\ & \times Q\left(\frac{\ln((1+\overline{\chi}_{rd}\Omega_{e_{rd}})\chi/\overline{\chi}_{rd}) - 2\mu_{h_{rd}}}{2\sigma_{h_{rd}}}\right) + \frac{\exp\left(\frac{-\left[\ln\left((1+\overline{\chi}_{rd}\Omega_{e_{rd}})\chi/\overline{\chi}_{rd}\right)-2\mu_{h_{rd}}\right]^2}{8\sigma_{h_{rd}}^2}\right)}{2\sqrt{2\pi}\,\sigma_{h_{rd}}\chi} \\ & \times \exp\left(\frac{-(1+\overline{\chi}_{sr}\Omega_{e_{sr}})\chi}{\overline{\chi}_{sr}}\right)\Bigg] d\chi. \end{aligned} \tag{C.2}$$

For mathematical tractability of (C.2), we use an approximation of $Q(\cdot)$ function developed by Borjesson and Sundberg and is given in [96, Eq. (16)]. On applying Borjesson approximation in (C.2) and simplifying, results in

$$\mathbb{E}[\Psi(\chi_{e2e})] = \mathcal{I}_1 - \mathcal{I}_2, \tag{C.3}$$

where

$$\mathcal{I}_1 = \left(\frac{1+\overline{\chi}_{sr}\Omega_{e_{sr}}}{\overline{\chi}_{sr}}\right) \int_0^\infty \Psi(\chi) \exp\left(\frac{-(1+\overline{\chi}_{sr}\Omega_{e_{sr}})\chi}{\overline{\chi}_{sr}}\right) d\chi, \tag{C.4}$$

and

$$\mathcal{I}_2 = \int_0^\infty \Psi(\chi)\frac{1}{2\sqrt{2\pi}\ \sigma_{h_{rd}}\chi} \exp\Big(\frac{-(1+\overline{\chi}_{sr}\Omega_{e_{sr}})\chi}{\overline{\chi}_{sr}}\Big)\left\{\frac{2\ \sigma_{h_{rd}}\chi\big(1+\overline{\chi}_{sr}\Omega_{e_{sr}}\big)}{\overline{\chi}_{sr}\sqrt{\left(\frac{\ln\left((1+\overline{\chi}_{rd}\Omega_{e_{rd}})\chi/\overline{\chi}_{rd}\right)-2\mu_{h_{rd}}}{2\sigma_{h_{rd}}}\right)^2+1}}-1\right\}$$
$$\times \exp\left(\frac{-\big[\ln((1+\overline{\chi}_{rd}\Omega_{e_{rd}})\chi/\overline{\chi}_{rd})-2\mu_{h_{rd}}\big]^2}{8\sigma^2_{h_{rd}}}\right)d\chi. \tag{C.5}$$

On performing change of variable $y = \frac{\ln\left((1+\overline{\chi}_{rd}\Omega_{e_{rd}})\chi/\overline{\chi}_{rd}\right)-2\mu_{h_{rd}}}{2\sqrt{2}\ \sigma_{h_{rd}}}$ in (C.5), and after rearranging the terms we get

$$\begin{aligned}\mathcal{I}_2 = \frac{1}{\sqrt{\pi}}\int_{-\infty}^{\infty}&\Psi\Big(\frac{\overline{\chi}_{rd}}{1+\overline{\chi}_{rd}\Omega_{e_{rd}}}\exp\big(2\sqrt{2}\ \sigma_{h_{rd}}y+2\mu_{h_{rd}}\big)\Big)\\ &\times\exp\Big(\frac{-\overline{\chi}_{rd}(1+\overline{\chi}_{sr}\Omega_{e_{sr}})\exp\big(2\sqrt{2}\ \sigma_{h_{rd}}y+2\mu_{h_{rd}}\big)}{\overline{\chi}_{sr}(1+\overline{\chi}_{rd}\Omega_{e_{rd}})}\Big)\\ &\times\left\{\frac{2\ \sigma_{h_{rd}}\overline{\chi}_{rd}(1+\overline{\chi}_{sr}\Omega_{e_{sr}})\exp\big(2\sqrt{2}\ \sigma_{h_{rd}}y+2\mu_{h_{rd}}\big)}{\overline{\chi}_{sr}(1+\overline{\chi}_{rd}\Omega_{e_{rd}})\sqrt{2y^2+1}}-1\right\}\exp\big(-y^2\big)dy.\end{aligned} \tag{C.6}$$

The integral expression of (C.6) matches the Gauss-Hermite quadrature integral form, which on utilizing the numerical integral technique stated in [63, Eq. (25.4.46)] yields (5.15).

C.2 Solution of EQ. (5.17)

Equation (5.17) can be written as

$$\mathcal{I}_1 = 2p_0\mathbb{G}_1(a_0)+2q_0\mathbb{G}_1(b_0)-4p_0q_0\mathbb{G}_2(a_0,b_0), \tag{C.7}$$

where

$$\mathbb{G}_1(\nu) = \Big(\frac{1+\overline{\chi}_{sr}\Omega_{e_{sr}}}{\overline{\chi}_{sr}}\Big)\int_0^\infty Q(\nu\sqrt{\chi})\exp\left(\frac{-(1+\overline{\chi}_{sr}\Omega_{e_{sr}})\chi}{\overline{\chi}_{sr}}\right)d\chi, \tag{C.8}$$

$$\mathbb{G}_2(\nu,\varrho) = \Big(\frac{1+\overline{\chi}_{sr}\Omega_{e_{sr}}}{\overline{\chi}_{sr}}\Big)\int_0^\infty Q(\nu\sqrt{\chi})Q(\varrho\sqrt{\chi})\exp\left(\frac{-(1+\overline{\chi}_{sr}\Omega_{e_{sr}})\chi}{\overline{\chi}_{sr}}\right)d\chi. \tag{C.9}$$

Performing change of variable $\chi = y^2$ in (C.8) and (C.9), and utilizing [97, eq. (7) and eq. (5)], we obtain

$$\mathbb{G}_1(\nu) = \frac{1}{2} - \frac{1}{2}\sqrt{\frac{\overline{\chi}_{sr}\nu^2}{(2(1+\overline{\chi}_{sr}\Omega_{e_{sr}}) + \overline{\chi}_{sr}\nu^2)}}, \tag{C.10}$$

$$\begin{aligned}\mathbb{G}_2(\nu, \varrho) = &\frac{1}{4} - \frac{1}{2\pi}\sqrt{\frac{\overline{\chi}_{sr}\nu^2}{(2(1+\overline{\chi}_{sr}\Omega_{e_{sr}}) + \overline{\chi}_{sr}\nu^2)}}\tan^{-1}\left(\frac{\nu}{\varrho}\sqrt{\frac{(2(1+\overline{\chi}_{sr}\Omega_{e_{sr}}) + \overline{\chi}_{sr}\nu^2)}{\overline{\chi}_{sr}\nu^2}}\right) - \\ &- \frac{1}{2\pi}\sqrt{\frac{\overline{\chi}_{sr}\varrho^2}{(2(1+\overline{\chi}_{sr}\Omega_{e_{sr}}) + \overline{\chi}_{sr}\varrho^2)}}\tan^{-1}\left(\frac{\varrho}{\nu}\sqrt{\frac{(2(1+\overline{\chi}_{sr}\Omega_{e_{sr}}) + \overline{\chi}_{sr}\varrho^2)}{\overline{\chi}_{sr}\varrho^2}}\right).\end{aligned} \tag{C.11}$$

Finally, on substituting (C.10), and (C.11) into (C.7), the solution of $\mathcal{I}_1$ is obtained as

$$\begin{aligned}\mathcal{I}_1 = &\, p_0 + q_0 - p_0 q_0 - p_0\sqrt{\frac{\overline{\chi}_{sr}a_0^2}{(2(1+\overline{\chi}_{sr}\Omega_{e_{sr}}) + \overline{\chi}_{sr}a_0^2)}} - q_0\sqrt{\frac{\overline{\chi}_{sr}b_0^2}{(2(1+\overline{\chi}_{sr}\Omega_{e_{sr}}) + \overline{\chi}_{sr}b_0^2)}} \\ &+ \frac{2p_0q_0}{\pi}\sqrt{\frac{\overline{\chi}_{sr}a_0^2}{(2(1+\overline{\chi}_{sr}\Omega_{e_{sr}}) + \overline{\chi}_{sr}a_0^2)}}\tan^{-1}\left(\frac{a_0}{b_0}\sqrt{\frac{(2(1+\overline{\chi}_{sr}\Omega_{e_{sr}}) + \overline{\chi}_{sr}a_0^2)}{\overline{\chi}_{sr}a_0^2}}\right) \\ &+ \frac{2p_0q_0}{\pi}\sqrt{\frac{\overline{\chi}_{sr}b_0^2}{(2(1+\overline{\chi}_{sr}\Omega_{e_{sr}}) + \overline{\chi}_{sr}b_0^2)}}\tan^{-1}\left(\frac{b_0}{a_0}\sqrt{\frac{(2(1+\overline{\chi}_{sr}\Omega_{e_{sr}}) + \overline{\chi}_{sr}b_0^2)}{\overline{\chi}_{sr}b_0^2}}\right).\end{aligned} \tag{C.12}$$

C.3 Solution of EQ. (5.19)

Equation (5.19) can be written as

$$\mathcal{I}_1 = \frac{13}{4}\mathbb{G}_1(\sqrt{2A}) + \frac{1}{8}\mathbb{G}_1(2\sqrt{A}) - \frac{23}{8}\mathbb{G}_2(\sqrt{2A}, \sqrt{2A}), \tag{C.13}$$

where $\mathbb{G}_1(\cdot)$, and $\mathbb{G}_2(\cdot,\cdot)$ are defined in (C.8) and (C.9), respectively. Using (C.10) and (C.11) in (C.13) results in the solution of $\mathcal{I}_1$ as

$$\begin{aligned}\mathcal{I}_1 = &\frac{47}{32} - \frac{13}{8}\sqrt{\frac{2A\overline{\chi}_{sr}}{(2(1+\overline{\chi}_{sr}\Omega_{e_{sr}}) + 2A\overline{\chi}_{sr})}} - \frac{1}{16}\sqrt{\frac{4A\overline{\chi}_{sr}}{(2(1+\overline{\chi}_{sr}\Omega_{e_{sr}}) + 4A\overline{\chi}_{sr})}} \\ &+ \frac{23}{8\pi}\sqrt{\frac{\overline{\chi}_{sr}A}{((1+\overline{\chi}_{sr}\Omega_{e_{sr}}) + \overline{\chi}_{sr}A)}}\tan^{-1}\left(\sqrt{\frac{((1+\overline{\chi}_{sr}\Omega_{e_{sr}}) + \overline{\chi}_{sr}A)}{\overline{\chi}_{sr}A}}\right).\end{aligned} \tag{C.14}$$

C.4 Solution of EQ. (5.21)

Equation (5.21) can be written as

$$\mathcal{I}_1 = D_C \mathbb{G}_1(\sqrt{q_1}) + \frac{2}{3} D_C \mathbb{G}_2(\sqrt{2q_1/3}, \sqrt{2q_1/3}) - 2D_C \mathbb{G}_2(\sqrt{q_1}, \sqrt{q_1/3}), \tag{C.15}$$

where $\mathbb{G}_1(\cdot)$, and $\mathbb{G}_2(\cdot,\cdot)$ are defined in (C.8) and (C.9), respectively. Using (C.10) and (C.11) in (C.15) results in the solution of $\mathcal{I}_1$ as

$$\begin{aligned}
\mathcal{I}_1 = {} & \frac{D_C}{2} + \frac{1}{6} - \frac{D_C}{2} - \frac{D_C}{2}\sqrt{\frac{\overline{\chi}_{sr} q_1}{(2(1+\overline{\chi}_{sr}\Omega_{e_{sr}}) + \overline{\chi}_{sr} q_1}} - \frac{2}{3\pi}\sqrt{\frac{\overline{\chi}_{sr} q_1}{(3(1+\overline{\chi}_{sr}\Omega_{e_{sr}}) + \overline{\chi}_{sr} q_1)}} \\
& \times \tan^{-1}\left(\sqrt{\frac{(3(1+\overline{\chi}_{sr}\Omega_{e_{sr}}) + \overline{\chi}_{sr} q_1)}{\overline{\chi}_{sr} q_1}}\right) + \frac{D_C}{\pi}\sqrt{\frac{\overline{\chi}_{sr} q_1}{(2(1+\overline{\chi}_{sr}\Omega_{e_{sr}}) + \overline{\chi}_{sr} q_1)}} \\
& \times \tan^{-1}\left(\sqrt{\frac{\sqrt{3}(2(1+\overline{\chi}_{sr}\Omega_{e_{sr}}) + \overline{\chi}_{sr} q_1)}{\overline{\chi}_{sr} q_1}}\right) + \frac{D_C}{\pi}\sqrt{\frac{\overline{\chi}_{sr} q_1}{(6(1+\overline{\chi}_{sr}\Omega_{e_{sr}}) + \overline{\chi}_{sr} q_1)}} \\
& \times \tan^{-1}\left(\sqrt{\frac{(6(1+\overline{\chi}_{sr}\Omega_{e_{sr}}) + \overline{\chi}_{sr} q_1)}{\sqrt{3}\overline{\chi}_{sr} q_1}}\right).
\end{aligned} \tag{C.16}$$

References

[1] M. Z. Chowdhury, M. T. Hossan, A. Islam, and Y. M. Jang, "A comparative survey of optical wireless technologies: Architectures and applications," *IEEE Access*, vol. 6, pp. 9819–9840, Mar. 2018.

[2] A. Al-Kinani, C.-X. Wang, L. Zhou, and W. Zhang, "Optical wireless communication channel measurements and models," *IEEE Commun. Surv. Tuts.*, vol. 20, no. 3, pp. 1939–1962, 3rd Quart. 2018.

[3] A. Vavoulas, H. G. Sandalidis, N. D. Chatzidiamantis, Z. Xu, and G. K. Karagiannidis, "A survey on ultraviolet C-Band (UV-C) communications," *IEEE Commun. Surv. Tuts.*, vol. 21, no. 3, pp. 2111–2133, 3rd Quart. 2019.

[4] Z. Xu and B. M. Sadler, "Ultraviolet communications: potential and state-of-the-art," *IEEE Commun. Mag.*, vol. 46, no. 5, pp. 67–73, May 2008.

[5] D. M. Reilly and C. Warde, "Temporal characteristics of single-scatter radiation," *J. Opt. Soc. Am.*, vol. 69, no. 3, pp. 464–470, Mar. 1979.

[6] M. R. Luettgen, J. H. Shapiro, and D. M. Reilly, "Non-line-of-sight single-scatter propagation model," *J. Opt. Soc. Am.*, vol. 8, no. 12, pp. 1964–1972, Dec. 1991.

[7] I. C. on Non-Ionizing Radiation Protection (ICNIRP), "Guidelines on limits of exposure to ultraviolet radiation of wavelengths between 180 nm and 400 nm (incoherent optical radiation)," *Health Phys.*, vol. 87, no. 2, pp. 171–186, Aug. 2004.

[8] X. Sun, Z. Zhang, A. Chaaban, T. K. Ng, C. Shen, R. Chen, J. Yan, H. Sun, X. Li, J. Wang, J. Li, M.-S. Alouini, and B. S. Ooi, "71-Mbit/s ultraviolet-B LED commu-

nication link based on 8-QAM-OFDM modulation," *Opt. Exp.*, vol. 25, no. 19, pp. 23 267–23 274, Sep. 2017.

[9] Z. Yong, W. Jian, X. Houfei, and L. Jintong, "Non-line-of-sight ultraviolet communication performance in atmospheric turbulence," *China Commun.*, vol. 10, no. 11, pp. 52–57, Nov. 2013.

[10] Z. Xu, H. Ding, B. M. Sadler, and G. Chen, "Analytical performance study of solar blind non-line-of-sight ultraviolet short-range communication links," *Opt. Lett.*, vol. 33, no. 16, pp. 1860–1862, Aug. 2008.

[11] H. Ding, G. Chen, A. K. Majumdar, B. M. Sadler, and Z. Xu, "Turbulence modeling for non-line-of-sight ultraviolet scattering channels," *Proc. SPIE*, vol. 8038, 80380J, May 2011.

[12] M. H. Ardakani, A. R. Heidarpour, and M. Uysal, "Performance analysis of relay-assisted NLOS ultraviolet communications over turbulence channels," *IEEE/OSA J. Opt. Commun. Netw.*, vol. 9, no. 1, pp. 109–118, Jan. 2017.

[13] S. Arnon, J. Barry, G. Karagiannidis, R. Schober, and M. Uysal, *Advanced Optical Wireless Communication Systems.* Cambridge Univ. Press, 2012.

[14] A. Goldsmith, *Wireless Communications*, 1st ed. Cambridge University Press, 2005.

[15] S. C. Schwartz and Y. S. Yeh, "On the distribution function and moments of power sums with log-normal components," *The Bell System Technol. J.*, vol. 61, no. 7, pp. 1441–1462, Sept. 1982.

[16] L. Fenton, "The sum of log-normal probability distributions in scatter transmission systems," *IRE Trans. Commun. Syst.*, vol. 8, no. 1, pp. 57–67, Mar. 1960.

[17] A. Safak, "Statistical analysis of the power sum of multiple correlated log-normal components," *IEEE Trans. Veh. Technol.*, vol. 42, no. 1, pp. 58–61, Feb. 1993.

[18] N. C. Beaulieu, A. A. Abu-Dayya, and P. J. McLane, "Estimating the distribution of a sum of independent lognormal random variables," *IEEE Trans. Commun.*, vol. 43, no. 12, p. 2869, Dec. 1995.

[19] N. B. Mehta, J. Wu, A. F. Molisch, and J. Zhang, "Approximating a sum of random variables with a lognormal," *IEEE Trans. Wireless Commun.*, vol. 6, no. 7, Jul. 2007.

[20] Y.-W. P. Hong, W.-J. Huang, and C.-C. J. Kuo, *Cooperative communications and networking: technologies and system design*, 1st ed.

[21] I. . W. Group *et al.*, "IEEE standard for local and metropolitan area networks, part 16: Air interface for broadband wireless access systems, amendment 1: Multi-hop relay specification," *IEEE Standard 802.16 j-2009*, 2009.

[22] J. N. Laneman, D. N. Tse, and G. W. Wornell, "Cooperative diversity in wireless networks: Efficient protocols and outage behavior," *IEEE Trans. Inf. Theory*, vol. 50, no. 12, pp. 3062–3080, Dec. 2004.

[23] X. He, E. Xie, M. S. Islim, A. Purwita, J. J. McKendry, E. Gu, H. Haas, and M. D. Dawson, "Deep UV micro-LED arrays for optical communications," in *Int. Conf. UV LED Technol. Appl. (ICULTA-2018)*, Apr. 2018.

[24] P. K. Singya, N. Kumar, V. Bhatia, and M.-S. Alouini, "On performance of hexagonal, cross, and rectangular QAM for multi-relay systems," *IEEE Access*, vol. 7, pp. 60 602–60 616, May 2019.

[25] S. Arya and Y. H. Chung, "Non-line-of-sight ultraviolet communication with receiver diversity in atmospheric turbulence," *IEEE Photon. Technol. Lett.*, vol. 30, no. 10, pp. 895–898, May 2018.

[26] B. Zhang, C. Gong, Q. Gao, and Z. Xu, "Two-way relay protocol for optical wireless scattering communication," *IEEE Commun. Lett.*, vol. 21, no. 4, pp. 913–916, Apr. 2017.

[27] C. Gong, K. Wang, Z. Xu, and X. Wang, "On full-duplex relaying for optical wireless scattering communication with on-off keying modulation," *IEEE Trans. Wireless Commun.*, vol. 17, no. 4, pp. 2525–2538, Apr. 2018.

[28] P. Song, X. Ke, F. Song, and T. Zhao, "Multi-user interference in a non-line-of-sight ultraviolet communication network," *IET Commun.*, vol. 10, no. 13, pp. 1640–1645, Sep. 2016.

[29] D. Han, Y. Liu, K. Zhang, P. Luo, and M. Zhang, "Theoretical and experimental research on diversity reception technology in NLOS UV communication system," *Opt. Exp.*, vol. 20, no. 14, pp. 15 833–15 842, Jul. 2012.

[30] G. Wang, K. Wang, C. Gong, D. Zou, Z. Jiang, and Z. Xu, "A 1Mbps real-time NLOS UV scattering communication system with receiver diversity over 1km," *IEEE Photon. J.*, vol. 10, no. 2, pp. 1–13, Apr. 2018.

[31] N. Kumar and V. Bhatia, "Exact ASER analysis of rectangular QAM in two-way relaying networks over Nakagami-m fading channels," *IEEE Wireless Commun. Lett.*, vol. 5, no. 5, pp. 548–551, Oct. 2016.

[32] D. Dixit and P. Sahu, "Performance analysis of rectangular QAM with SC receiver over Nakagami-m fading channels," *IEEE Commun. Lett.*, vol. 18, no. 7, pp. 1262–1265, Jul. 2014.

[33] N. Kumar, P. K. Singya, and V. Bhatia, "ASER analysis of hexagonal and rectangular QAM schemes in multiple-relay networks," *IEEE Trans. Veh. Technol.*, vol. 67, no. 2, pp. 1815–1819, Feb. 2018.

[34] P. K. Singya, N. Kumar, and V. Bhatia, "Impact of imperfect CSI on ASER of hexagonal and rectangular QAM for AF relaying network," *IEEE Commun. Lett.*, vol. 22, no. 2, Feb. 2018.

[35] P. Shaik, P. K. Singya, and V. Bhatia, "On impact of imperfect CSI over hexagonal QAM for TAS/MRC-MIMO cooperative relay network," *IEEE Commun. Lett.*, vol. 23, no. 10, pp. 1721–1724, Oct. 2019.

[36] X.-C. Zhang, H. Yu, and G. Wei, "Exact symbol error probability of Cross-QAM in AWGN and fading channels," *EURASIP J. Wireless Commun. Netw.*, vol. 2010, no. 1, pp. 1–9, Nov. 2010.

[37] L. Rugini, "Symbol error probability of hexagonal QAM," *IEEE Commun. Lett.*, vol. 20, no. 8, pp. 1523–1526, Aug. 2016.

[38] W. Huang, J. Takayanagi, T. Sakanaka, and M. Nakagawa, “Atmospheric optical communication system using subcarrier PSK modulation,” in *Proceedings of IEEE Int. Conf. Commun. (ICC)*, vol. 3, May 1993, pp. 1597–1601 vol.3.

[39] M. Z. Hassan, M. J. Hossain, J. Cheng, and V. C. Leung, “Subcarrier intensity modulated optical wireless communications: a survey from communication theory perspective,” *ZTE Commun.*, vol. 14, no. 2, pp. 2–12, Apr. 2016.

[40] P. K. Singya, N. Kumar, V. Bhatia, and M.-S. Alouini, “On the performance analysis of higher order QAM schemes over mixed RF/FSO systems,” *IEEE Trans. Veh. Technol.*, vol. 69, no. 7, pp. 7366–7378, Jul. 2020.

[41] M. Niu, J. Cheng, and J. F. Holzman, “Error rate performance comparison of coherent and subcarrier intensity modulated optical wireless communications,” *IEEE/OSA J. Opt. Commun. Netw.*, vol. 5, no. 6, pp. 554–564, Jun. 2013.

[42] M. Z. Hassan, X. Song, and J. Cheng, “Subcarrier intensity modulated wireless optical communications with rectangular QAM,” *IEEE/OSA J. Opt. Commun. Netw.*, vol. 4, no. 6, pp. 522–532, Jun. 2012.

[43] W. O. Popoola and Z. Ghassemlooy, “BPSK subcarrier intensity modulated free-space optical communications in atmospheric turbulence,” *J. Lightw. Technol.*, vol. 27, no. 8, pp. 967–973, Apr. 2009.

[44] A. Mishra and R. K. Giri, “Performance analysis of different modulation techniques in sim based fso using different receivers over turbulent channel,” in *2018 Int. Conf. Commun., Computing and Internet of Things (IC3IoT)*. IEEE, Feb. 2018, pp. 459–464.

[45] Z. Ghassemlooy, W. Popoola, and S. Rajbhandari, *Optical wireless communications: system and channel modelling with MATLAB*. CRC press, 2013.

[46] S. Arya and Y. H. Chung, “Amplify-and-forward multihop non-line-of-sight ultraviolet communication in the gamma-gamma fading channel,” *IEEE/OSA J. Opt. Commun. Netw.*, vol. 11, no. 8, pp. 422–436, Aug. 2019.

[47] M. Safari and M. Uysal, "Cooperative diversity over log-normal fading channels: performance analysis and optimization," *IEEE Trans Wireless Commun.*, vol. 7, no. 5, pp. 1963–1972, May 2008.

[48] G. Pan, E. Ekici, and Q. Feng, "Performance analysis of multi-branch multi-hop wireless relay systems over log-normal channels," *IEEE Trans. Wireless Commun.*, vol. 13, no. 1, pp. 223–233, Jan. 2014.

[49] M. Elamassie, M. Al-Nahhal, R. C. Kizilirmak, and M. Uysal, "Transmit laser selection for underwater visible light communication systems," in *2019 IEEE 30th Annu. Int. Symp. on Personal, Indoor Mobile Radio Commun. (PIMRC)*, Nov. 2019, pp. 1–6.

[50] A. J. Paulraj and T. Kailath, "Increasing capacity in wireless broadcast systems using distributed transmission/directional reception (DTDR)," Sep. 1994, US Patent 5,345,599.

[51] L. Zheng and D. N. C. Tse, "Diversity and multiplexing: A fundamental tradeoff in multiple-antenna channels," *IEEE Trans. Inf. Theory*, vol. 49, no. 5, pp. 1073–1096, May 2003.

[52] A. J. Paulraj, D. A. Gore, R. U. Nabar, and H. Bolcskei, "An overview of MIMO communications-a key to gigabit wireless," *Proc. IEEE*, vol. 92, no. 2, pp. 198–218, 2004.

[53] A. Nosratinia, T. E. Hunter, and A. Hedayat, "Cooperative communication in wireless networks," *IEEE Commun. Mag.*, vol. 42, no. 10, pp. 74–80, Oct. 2004.

[54] M. A. Amirabadi and V. T. Vakili, "Performance comparison of two novel relay-assisted hybrid FSO/RF communication systems," *IET Commun.*, vol. 13, no. 11, pp. 1551–1556, Jul. 2019.

[55] J. Al-Khori, G. Nauryzbayev, M. M. Abdallah, and M. Hamdi, "Secrecy performance of decode-and-forward based hybrid RF/VLC relaying systems," *IEEE Access*, vol. 7, pp. 10 844–10 856, Jan. 2019.

[56] H. Lei, H. Luo, K. Park, I. S. Ansari, W. Lei, G. Pan, and M.-S. Alouini, "On secure mixed RF-FSO systems with TAS and imperfect CSI," *IEEE Trans. Commun.*, vol. 68, no. 7, pp. 4461–4475, 2020.

[57] E. Zedini, H. Soury, and M.-S. Alouini, "On the performance analysis of dual-hop mixed FSO/RF systems," *IEEE Trans. Wireless Commun.*, vol. 15, no. 5, pp. 3679–3689, May 2016.

[58] X. Song, F. Yang, and J. Cheng, "Subcarrier intensity modulated optical wireless communications in atmospheric turbulence with pointing errors," *IEEE/OSA J. Opt. Commun. Netw.*, vol. 5, no. 4, pp. 349–358, Apr. 2013.

[59] S. Han, S. Ahn, E. Oh, and D. Hong, "Effect of Channel-Estimation Error on BER Performance in Cooperative Transmission," *IEEE Trans. Veh. Technol.*, vol. 58, no. 4, pp. 2083–2088, May 2009.

[60] H. Yu, G. Wei, F. Ji, and X. Zhang, "On the error probability of cross-QAM with MRC reception over generalized η-μ fading channels," *IEEE Trans. Veh. Technol.*, vol. 60, no. 6, pp. 2631–2643, Jul. 2011.

[61] G. Chen, Z. Xu, H. Ding, and B. M. Sadler, "Path loss modeling and performance trade-off study for short-range non-line-of-sight ultraviolet communications," *Opt. Exp.*, vol. 17, no. 5, pp. 3929–3940, Mar. 2009.

[62] S. S. Gupta, "Probability integrals of multivariate normal and multivariate t," *Annals of Mathematical Statistics*, vol. 34, pp. 792–828, 1963.

[63] M. Abramowitz and I. A. Stegun, *Handbook of Mathematical Functions (National Bureau of Standards, Washington, DC, 1972)*, 10th ed. Dover Publ., Jun. 1972.

[64] K. K. Garg, P. K. Singya, and V. Bhatia, "Performance analysis of AF relayed NLOS UV communication over turbulent channel," in *IEEE Int. Conf. Adv. Net. Telecommun. Sys. (ANTS)*, Dec. 2018, pp. 1–5.

[65] M. H. Ardakani, A. R. Heidarpour, and M. Uysal, "Non-line-of-sight ultraviolet communications over atmospheric turbulence channels," in *4th Int. Workshop Opt. Wireless Commun. (IWOW)*, Sep. 2015, pp. 55–59.

[66] A. Refaai, M. Abaza, M. S. El-Mahallawy, and M. H. Aly, "Performance analysis of multiple NLOS UV communication cooperative relays over turbulent channels," *Opt. Exp.*, vol. 26, no. 16, pp. 19 972–19 985, Aug. 2018.

[67] M. H. Ardakani and M. Uysal, "Relay-assisted OFDM for ultraviolet communications: Performance analysis and optimization," *IEEE Trans. Wireless Commun.*, vol. 16, no. 1, pp. 607–618, Jan. 2017.

[68] K. K. Garg, P. K. Singya, and V. Bhatia, "ASER analysis of general order rectangular QAM for dual-hop NLOS UV communication system," in *2019 National Conf. Commun. (NCC)*, Feb. 2019, pp. 1–6.

[69] M. A. Amirabadi and V. T. Vakili, "Performance evaluation of a novel relay-assisted hybrid FSO/RF communication system with receive diversity," *IET Optoelec.*, vol. 13, no. 5, pp. 203–214, Oct. 2019.

[70] ——, "Performance of a relay-assisted hybrid FSO/RF communication system," *Physical Commun.*, vol. 35, 100729, pp. 1–9, Aug. 2019.

[71] ——, "On the performance of a multi-user multi-hop hybrid FSO/RF communication system," *Opt. Commun.*, vol. 444, pp. 172–183, Aug. 2019.

[72] Q. Yang, J. Shi, M. Xiao, and H. Chen, "A decentralized slot synchronization algorithm for tdma-based ad hoc networks," in *Int. Conf. Wireless Commun. Netw. Mob. Comp.*, Sep. 2007, pp. 1717–1721.

[73] K. K. Garg, P. K. Singya, and V. Bhatia, "Performance analysis of NLOS ultraviolet communications with correlated branches over turbulent channels," *IEEE/OSA J. Opt. Commun. Netw.*, vol. 11, no. 11, pp. 525–535, Nov. 2019.

[74] P. Shaik, K. K. Garg, and V. Bhatia, "On impact of imperfect channel state information on dual-hop nonline-of-sight ultraviolet communication over turbulent channel," *Opt. Eng.*, vol. 59, no. 1, pp. 1 – 14, Jan. 2020.

[75] J. G. Proakis and M. Salehi, *Digital Communications*, 5th ed. McGraw-Hill, 2008.

[76] K. K. Garg, P. Shaik, and V. Bhatia, "Performance analysis of cooperative relaying technique for non-line-of-sight UV communication system in the presence of turbulence," *Opt. Eng.*, vol. 59, no. 5, pp. 1 – 16, Apr. 2020.

[77] M. Seyfi, S. Muhaidat, and J. Liang, "Amplify-and-forward selection cooperation over Rayleigh fading channels with imperfect CSI," *IEEE Trans. Wireless Commun.*, vol. 11, no. 1, pp. 199–209, Jan. 2012.

[78] V. Bhatia, B. Mulgrew, and D. D. Falconer, "Non-parametric maximum-likelihood channel estimator and detector for OFDM in presence of interference," *IET Commun.*, vol. 1, no. 4, pp. 647–654, Aug. 2007.

[79] K. K. Garg and V. Bhatia, "Performance analysis of cooperative nlos uvc system with receiver diversity," in *2020 National Conf. Commun. (NCC)*, Feb. 2020, pp. 1–6.

[80] J. Hu and N. C. Beaulieu, "Performance analysis of decode-and-forward relaying with selection combining," *IEEE Commun. Lett.*, vol. 11, no. 6, pp. 489–491, Jun. 2007.

[81] L. C. Andrews, R. L. Phillips, and C. Y. Hopen, *Laser beam scintillation with applications.* SPIE press, 2001, vol. 99.

[82] S. Anees and M. R. Bhatnagar, "Performance of an amplify-and-forward dual-hop asymmetric RF-FSO communication system," *J. Opt. Commun. Netw.*, vol. 7, no. 2, pp. 124–135, Feb. 2015.

[83] S. Anees and M. R. Bhatnagar, "Performance evaluation of decode-and-forward dual-hop asymmetric radio frequency-free space optical communication system," *IET Optoelec.*, vol. 9, no. 5, pp. 232–240, Oct. 2015.

[84] Y. F. Al-Eryani, A. M. Salhab, S. A. Zummo, and M.-S. Alouini, "Two-way multiuser mixed RF/FSO relaying: Performance analysis and power allocation," *J. Opt. Commun. Netw.*, vol. 10, no. 4, pp. 396–408, Apr. 2018.

[85] G. Pan, H. Lei, Y. Deng, L. Fan, J. Yang, Y. Chen, and Z. Ding, "On secrecy performance of MISO SWIPT systems with TAS and imperfect CSI," *IEEE Trans. Commun.*, vol. 64, no. 9, pp. 3831–3843, May 2016.

[86] J. Zhang, X. Pan, G. Pan, and Y. Xie, "Secrecy analysis for multi-relaying RF-FSO systems with a multi-aperture destination," *IEEE Photon. J.*, vol. 12, no. 2, pp. 1–11, Apr. 2020.

[87] A. Upadhya, V. K. Dwivedi, and G. K. Karagiannidis, "On the effect of interference and misalignment error in mixed RF/FSO systems over generalized fading channels," *IEEE Trans. Commun.*, vol. 68, no. 6, pp. 3681–3695, Jun. 2020.

[88] S. H. Islam, A. S. M. Badrudduza, S. M. Riazul Islam, F. I. Shahid, I. S. Ansari, M. K. Kundu, S. K. Ghosh, M. B. Hossain, A. S. M. S. Hosen, and G. H. Cho, "On secrecy performance of mixed generalized gamma and RF-FSO variable gain relaying channel," *IEEE Access*, vol. 8, pp. 104 127–104 138, May 2020.

[89] C. Gong and Z. Xu, "Channel estimation and signal detection for optical wireless scattering communication with inter-symbol interference," *IEEE Trans. Wireless Commun.*, vol. 14, no. 10, pp. 5326–5337, Oct. 2015.

[90] S. M. Kay, *Fundamentals of Statistical Signal Processing: Estimation Theory*, 1st ed. NJ, Englewood Cliffs: Prentice-Hall, Inc., 1993.

[91] L. L. Scharf, *Statistical Signal Processing: Detection, Estimation, and Time Series Analysis*, 1st ed. Addison-Wesley, 1991.

[92] F. Fang, H. Zhang, J. Cheng, S. Roy, and V. C. M. Leung, "Joint user scheduling and power allocation optimization for energy-efficient NOMA systems with imperfect CSI," *IEEE J. Sel. Areas Commun.*, vol. 35, no. 12, pp. 2874–2885, Nov. 2017.

[93] L. Wang, Y. Cai, and W. Yang, "On the finite-SNR DMT of two-way af relaying with imperfect CSI," *IEEE Wireless Commun. Lett.*, vol. 1, no. 3, pp. 161–164, Jun. 2012.

[94] V. Bhatia and B. Mulgrew, "Non-parametric likelihood based channel estimator for Gaussian mixture noise," *Signal Process.*, vol. 87, no. 11, pp. 2569–2586, Nov. 2007.

[95] F. Caliò and A. Lazzari, *Elements of Mathematics with Numerical Applications*, 2nd ed. Società Editrice Esculapio, 2017.

[96] V. N. Q. Bao, L. P. Tuyen, and H. H. Tue, "A survey on approximations of one-dimensional Gaussian Q-function," *REV J. Electron. Commun.*, vol. 5, no. 1-2, pp. 1–14, Jan.–Jun. 2015.

[97] N. C. Beaulieu, "A useful integral for wireless communication theory and its application to rectangular signaling constellation error rates," *IEEE Trans. Commun.*, vol. 54, no. 5, pp. 802–805, May 2006.

List of publications

Journal Papers:

1. **K. K. Garg**, P. Shaik, V. Bhatia, and O. Krejcar, "On the performance of a relay assisted hybrid RF-NLOS UVC system with imperfect channel estimation," *IEEE/OSA J. Opt. Commun. Netw.*, vol. 14, no. 4, pp. 177-189, Apr. 2022.

2. **K. K. Garg**, P. Shaik, P. K. Singya, and V. Bhatia, "Performance of multiple relay DF NLOS UVC system with CSI imperfections," *IEEE Open J. Commun. Soc.*, vol. 2, pp. 602-616, Mar. 2021.

3. V. Bhatia, S. Jain, **K. K. Garg**, and R. Mitra, "Performance analysis of RKHS based detectors for nonlinear NLOS ultraviolet communications," *IEEE Trans. Veh. Technol.*, vol. 70, no. 4, pp. 3625-3639, Apr. 2021.

4. **K. K. Garg**, P. Shaik, and V. Bhatia, "Performance analysis of cooperative relaying technique for non-line-of-sight UV communication system in the presence of turbulence," *Opt. Eng.*, vol. 59, no. 5, pp. 1-16, Apr. 2020.

5. P. Shaik, **K. K. Garg**, and V. Bhatia, "On impact of imperfect channel state information on dual-hop nonline-of-sight ultraviolet communication over turbulent channel," *Opt. Eng.*, vol. 59, no. 1, pp. 1-14, Jan. 2020.

6. **K. K. Garg**, P. K. Singya, and V. Bhatia, "Performance analysis of NLOS ultraviolet communications with correlated branches over turbulent channels," *IEEE/OSA J. Opt. Commun. Netw.*, vol. 11, no. 11, pp. 525-535, Nov. 2019.

Conference Papers:

1. P. Shaik, P. K. Singya, **K. K. Garg**, and V. Bhatia, "Outage probability analysis of SWIPT device-to-device MIMO relay systems with outdated CSI," in *IEEE Wireless Commun. Netw. Conf. (WCNC)*, Mar. 2021, pp. 1-6.

2. P. Shaik, P. K. Singya, N. Kumar, **K. K. Garg**, and V. Bhatia, "On impact of imperfect CSI over SWIPT device-to-device (D2D) MIMO relay systems," in *Int. Conf. on Sig. Process. Commun. (SPCOM)*, Jul. 2020, pp. 1-5.

3. **K. K. Garg** and V. Bhatia, "Performance analysis of cooperative NLOS UVC system with receiver diversity," in *National Conf. Commun. (NCC)*, Feb. 2020, pp. 1-6.

4. **K. K. Garg**, P. K. Singya, and V. Bhatia, "ASER analysis of general order rectangular QAM for dual-hop NLOS UV communication system," in *National Conf. Commun. (NCC)*, Feb. 2019, pp. 1-6.

5. **K. K. Garg**, P. K. Singya, and V. Bhatia, "Performance analysis of AF relayed NLOS UV communication over turbulent channel," in *IEEE Int. Conf. Adv. Netw. Telecommun. Sys. (ANTS)*, Dec. 2018, pp. 1-5.